DEVELOPMENT OF NEW ARRAY SIGNAL PROCESSING TECHNIQUES USING SWARM INTELLIGENCE

A THESIS

SUBMITTED TO THE DEPARTMENT OF ELECTRICAL AND ELECTRONICS ENGINEERING

AND THE INSTITUTE OF ENGINEERING AND SCIENCES

OF BILKENT UNIVERSITY

IN PARTIAL FULFILLMENT OF THE REQUIREMENTS

FOR THE DEGREE OF

DOCTOR OF PHILOSOPHY

By

Mehmet Burak Güldoğan

May 2010

I certify that I have read this thesis and that in my opinion it is fully adequate, in scope and in quality, as a thesis for the degree of Doctor of Philosophy.

Prof. Dr. Orhan Arıkan(Supervisor)

I certify that I have read this thesis and that in my opinion it is fully adequate, in scope and in quality, as a thesis for the degree of Doctor of Philosophy.

Assist. Prof. Dr. Sinan Gezici

I certify that I have read this thesis and that in my opinion it is fully adequate, in scope and in quality, as a thesis for the degree of Doctor of Philosophy.

Prof. Dr. Mustafa Ç. Pınar

I certify that I have read this thesis and that in my opinion it is fully adequate, in scope and in quality, as a thesis for the degree of Doctor of Philosophy.

Assoc. Prof. Dr. Ezhan Karaşan

I certify that I have read this thesis and that in my opinion it is fully adequate, in scope and in quality, as a thesis for the degree of Doctor of Philosophy.

Assist. Prof. Dr. Ali Cafer Gürbüz

Approved for the Institute of Engineering and Sciences:

Prof. Dr. Mehmet Baray
Director of Institute of Engineering and Sciences

ABSTRACT

DEVELOPMENT OF NEW ARRAY SIGNAL PROCESSING TECHNIQUES USING SWARM INTELLIGENCE

Mehmet Burak Güldoğan
Ph.D. in Electrical and Electronics Engineering
Supervisor: Prof. Dr. Orhan Arıkan
May 2010

In this thesis, novel array signal processing techniques are proposed for identification of multipath communication channels based on cross ambiguity function (CAF) calculation, swarm intelligence and compressed sensing (CS) theory. First technique detects the presence of multipath components by integrating CAFs of each antenna output in the array and iteratively estimates direction-of-arrivals (DOAs), time delays and Doppler shifts of a known waveform. Second technique called particle swarm optimization-cross ambiguity function (PSO-CAF) makes use of the CAF calculation to transform the received antenna array outputs to delay-Doppler domain for efficient exploitation of the delay-Doppler diversity of the multipath components. Clusters of multipath components are identified by using a simple amplitude thresholding in the delay-Doppler domain. PSO is used to estimate parameters of the multipath components in each cluster. Third proposed technique combines CS theory, swarm intelligence and CAF computation. Performance of standard CS formulations based on discretization of the multipath channel parameter space degrade significantly when the actual channel parameters deviate from the assumed discrete set of values. To alleviate this “off-grid”problem, a novel technique by making use of the PSO, that can also be used in applications other than the multipath channel identification is proposed. Performances of the proposed techniques are verified both on sythetic and real data.

Keywords: Parameter estimation, cross ambiguity function (CAF), particle swarm optimization (PSO), compressed sensing (CS), sparse approximation

ÖZET

SÜRÜ ZEKASI KULLANILARAK YENİ DİZİLİM SİNYAL İŞLEME TEKNİKLERİNİN GELİŞTİRİLMESİ

Mehmet Burak Güldoğan
Elektrik ve Elektronik Mühendisliği Doktora
Tez Yöneticisi: Prof. Dr. Orhan Arıkan
Mayıs 2010

Bu tezde, çokyollu haberleşme kanallarını modellemek için çapraz belirsizlik işlevi (CAF), sürü zekası ve sıkıştırılmış algılama (CS) teorisi tabanlı yeni dizi sinyal işleme teknikleri önerilmektedir. Birinci teknik, dizideki herbir antenin çıktısında hesaplanan CAF' lerin entegrasyonunu kullanarak hem çokyollu kanal birleşenlerinin varlığını tespit etmektedir hem de bilinen bir sinyale ait ekoların geliş yönlerini (DOAs), zaman gecikmelerini ve Doppler kaymalarını kestirebilmektedir. Parçacık sürü optimizasyonu - çapraz belirsizlik işlevi (PSO-CAF) adıyla önerilen ikinci teknik, çokyollu birleşenlerin gecikme-Doppler çeşitliliklerini verimli bir şekilde ortaya çıkarmak için CAF hesaplamasını kullanarak anten dizi çıktısını gecikme-Doppler düzlemine taşır. Gecikme-Doppler düzlemi üzerinde yer alan çokyollu birleşen kümeleri, basit bir genlik eşiklemesi ile tespit edilir. Herbir küme içerisindeki çokyollu birleşen parametrelerini kestirmek için PSO kullanılmıştır. Üçüncü önerilen teknik sıkıştırılmş algılama (CS) teorisini, sürü zekasını ve CAF hesaplamasını birleştirerek çokyollu kanal modellemesi yapmaktadır. Çokyollu kanal parametre uzayının ayrık örneklenmesine dayalı çalışan standart CS formülizasyonları, gerçek kanal parametrelerinin kabul edilmiş ayrık küme değerlerinden saptığı durumlarda performansları ciddi

bir şekilde düşmektedir. "Kötü ızgara" olarak da adlandırılabilinecek ve çokyollu kanal modellemesi dışında birçok başka uygulamada da karşılaşılaşılan bu problemi çözmek için yeni bir teknik sunulmaktadır. Önerilen tekniklerin başarımları sentetik ve gerçek sinyaller üzerinde doğrulanmıştır.

Anahtar Kelimeler: Parametre kestirimi, çapraz belirsizlik işlevi (CAF), parçacık sürü optimizasyonu (PSO), sıkıştırılmış algılama (CS), seyrek yaklaşma

ACKNOWLEDGMENTS

I am heartily thankful to my supervisor, Prof. Orhan Arıkan, whose encouragement, guidance and support from the initial to the final level enabled me to finish my graduate work. He is not only the best advisor that I have seen but also a role model as a researcher and a teacher to me. His intuition to see and solve a problem was amazing to me and it was a big pleasure to be advised by him.

I would also like to thank the other four members of my dissertation committee Dr. Sinan Gezici, Dr. Mustafa Pınar, Dr. Ezhan Karaşan and Dr. Ali Cafer Gürbüz for their careful reading of the dissertation draft and numerous helpful suggestions.

I would in particular like to thank Dr. Sinan Gezici for the endless hours of technical and non-technical discussions.

I would also like to thank all my current and former colleagues in the Department of Electrical and Electronics Engineering at Bilkent University for their rather enviable companionship. I would in particular like to express my gratitude to Uğur Töreyin, Celal Alp Tunç, Yaşar Kemal Alp, Hamza Soğancı, Ahmet Güngör, Mert Pilancı, Aykut Yıldız, İbrahim Onaran, Osman Gürlevik and Mete Kart.

Finally, I would like to express my gratitude to my parents and my sister for always believing in me and encouraging me to achieve my goals. My deepest gratitude goes to my wife, Seher, for her support and love which have been invaluable in helping me focus on my academic pursuits. My son Fikret Yusuf was born during my research work toward this dissertation and made my study and life at Bilkent University filled with joy.

Contents

List of Figures

List of Tables

Dedicated to memory of my father,
Dr. Fikret Güldoğan.

Chapter 1

INTRODUCTION

1.1 Objective and Contributions of this Work

Modern wireless communication systems are designed to operate in multipath environments where the transmitted information arrives at the receiver after reflecting off various obstacles that are present in the environment of the communication. A superposition of multiple delayed, attenuated, frequency-phase shifted copies of the original signal arrive at the receiver. This superposition of multiple copies of the emitted signal are called the multipath signal components. Although, at first, the presence of multipath arrivals seems to degrade the quality of the communication, a carefuly designed communication system can take advantage of the diversity provided by the multipath environment. Diversity in the multipath channels is a result of variation between the direction-of-arrivals (DOA), delays and Doppler shifts of the individual channel components. To take full advantage of this diversity, multipath communication channels should be accurately modeled. For this purpose, communication systems utilize antenna arrays and sophisticated signal processing techniques to produce estimates for multipath channel parameters.

Most of the time, since channel state information (CSI) is not available to systems, communication channel should be periodically estimated at the receiver to take advantage of the diversity provided by multipath propagation. There are a multitude of array signal processing techniques proposed for reliable and accurate estimation for these channel parameters. Multipath channel parameter estimation techniques can be grouped into three categories as [4]: spectral-based estimation, parametric subspace-based estimation and deterministic parametric estimation. Conventional beamformer, Capon's beamformer [5] and MUSIC [6] can be stated within the first category. In contrast to beamforming techniques, the multiple signal classification (MUSIC) algorithm provides statistically consistent estimates and became a highly popular algorithm [7], [8]. The signal subspace fitting (SSF) [9], weighted subspace fitting (WSF) [10], estimation of signal parameter estimation via rotational invariance techniques (ESPRIT) [11] and unitary ESPRIT [12] are computationally efficient techniques and belong to the second category. In the last category, maximum likelihood (ML) techniques should be stated [4], [13].

The ML criterion based channel identification is a commonly used framework due to its superior asymptotic performance. Having determined a parametric signal model, ML estimates are obtained by a search conducted in the parameter space to maximize the likelihood function. The major drawback of the ML technique is its high computational complexity associated with the direct maximization of multimodal and nonlinear likelihood function over a very large dimensional parameter space. Alternative maximization methods are proposed to obtain the ML estimates more efficiently. One of the most popular one to facilitate simple implementation of likelihood function is the expectation maximization (EM) algorithm formulated by Dempster *et al.* [14]. Simpler maximization steps in lower dimensional parameter spaces are used instead of the original likelihood function. Various different forms of the EM algorithm have been developed to further improve the performance. The most popular one is the space alternating generalized EM (SAGE) algorithm, which was developed by Fessler and Hero [15]. In SAGE, parameters are updated sequentially in contrast with the EM where all the parameters are updated simultaneously. Main advantage of the SAGE algorithm over the EM algorithm is its faster convergence resulting in an increased efficiency. Applications of SAGE algorithm are extensively reported in the literature [16], [17], [18], [19], [20], [21], [22].

In general, coded waveforms with the time-bandwidth products significantly larger than one are employed in wideband communication channels. In these systems, to have optimal extraction of the transmitted information, pulse compression of the receiver output is necessary and important. Pulse compression can be achieved by a simple matched filter that implements correlation of the incoming signal with the transmitted waveform in delay only channels. Nevertheless, in the presence of Doppler shifts a single matched filter cannot provide the optimal performance. Instead, a bank of matched filters each matched to a specific Doppler shift should be employed [23], providing individual Doppler slices of the CAF between the transmitted and received signals. As a result, integration of CAF calculation into the processing chain has both theoretical and practical advantageous. In the first part, a novel technique called cross-ambiguity function direction finding (CAF-DF), which reliably estimates the DOAs, time delays, and Doppler shifts of a known waveform impinging onto an array of antennas from several distinct paths [24], [25], [26], [27], [28], [29]. Unlike the other alternatives, the proposed CAF-DF technique provides joint delay and Doppler shift estimates on the cross ambiguity function surface. The CAF-DF technique can resolve highly correlated signals with closely spaced signal parameters even in poor SNR conditions.

Computational swarm intelligence based optimization techniques such as genetic algorithm (GA) [30], ant colony optimization [31], differential evolution

[32], honey bee colony [33], bacteria foraging [34] and particle swarm optimization (PSO) [35] can be used to optimize the ML based formulation. GA is one of the most popular and powerful search technique in the class of evolutionary algorithms used in many engineering problems [36], [37]. It borrows some key concepts from evolutionary biology such as crossover, mutation, inheritance and natural selection. Although, GA has a legitimate fame, it has some disadvantages: 1) burdensome implementation, 2) slow convergence, 3) tendency to converge towards local optima if the fitness function is not defined properly.

Particle swarm optimization (PSO) is another evolutionary computation algorithm which has been shown to be very effective in optimizing difficult multidimensional, nonlinear and multimodal problems in a variety of fields [38], [39], [40], [41], [42], [43], [44], [45], [46], [47]. PSO is first introduced by Eberhart and Kennedy in 1995 [35]. It was inspired by the social behavior of animals, specifically the ability of groups of animals to work collectively in finding the desirable positions in a given area. PSO utilizes a swarm of particles that fly through the problem search space. Each particle in the swarm represents a candidate solution. A few crucial points about PSO can be itemized to clarify the advantages of it over classical Newton-type techniques: 1) less sensitive to initialization, 2) better chance to find global optimum and 3) provides more accurate estimates.

In the second part of this thesis, a new transform domain array signal processing technique is proposed for identification of multipath communication channels [48], [49], [50]. The received array element outputs are transformed to delay-Doppler domain by using CAF computation for efficient exploitation of the delay-Doppler diversity of the multipath signals. In the transform domain, a simple amplitude threshold determined by the noise standard deviation helps to identify the clusters of multipath components. This way, the original channel identification problem is reduced to channel identification problems over the identified path clusters in the delay-Doppler domain. Since, each cluster has fewer multipath components, there is a significant advantage of conducting the required optimization for identification of channel parameters over the identified clusters. Here, because of its robust performance, we choose to use the particle swarm optimization (PSO) to obtain globally optimal values of the channel parameters in each cluster. Since the optimization problem is formulated in the CAF domain of the transmitted signal and the received array outputs, the developed technique is named as the PSO-CAF.

There have been many research efforts in developing training based methods for channel modeling [51], [52]. These efforts basically concentrate on two phases, namely sensing and reconstruction. In sensing phase, training signals are designed to probe the communication channel and in reconstruction phase, receiver output is processed to obtain channel state information. Designing proper training signals and developing efficient reconstruction techniques are highly critical in order to accurately model the channel. The general assumption in most of the important works in wireless communications is that there exists a rich multipath environment and linear reconstruction techniques are known to be optimal in these channels. However, recent research show that wireless channels have a sparse structure in time, frequency and space [53]. Moreover, it is presented in [53], [54], that training based methods using linear reconstruction techniques cannot fully exploit the sparse structure of the channel causing over utilization of the resources. Recently, by embedding the key concepts from compressed sensing, new training based techniques have been proposed for sparse channels that have better performance than usual least-squared based approaches to model the sparse wireless channel [53]. In [54], [55] authors use a virtual representation of physical multipath channels to model the time frequency response of sparse multipath channel. In [56], [57], matrix identification problem, where the matrix has a sparse representation in some basis, is discussed. Herman and Strohmer introduced the concept of compressed sensing radar, which provides better time frequency resolution over classical radar by exploiting the sparse structure [57].

Lastly, some other CS based techniques which found to be effective are presented in the following references [58], [59], [60], [61].

General assumption used in all of these approaches is that the all multipath components fall on the grid points, which is practically impossible as the multipath parameters are unknown. Hence the true grid, which is possibly irregular, cannot be known beforehand. This so called off-grid problem, results in a mismatch of the dictionary and severely degrades the performance of techniques that exploit sparsity. Furthermore, such methods exhibit an unstable behavior as previously shown in theoretical studies on dictionary errors. In several papers, the problem is pointed out and very simple grid refinement approaches are stated [62], [63].

In the third part of the thesis, a new algorithm is developed based on the compressed sensing (CS) theory to accurately estimate the multipaths [64], [65]. Similar to the first technique, the receiver output is transformed to delay-Doppler domain by using the CAF for efficient exploitation of the delay-Doppler diversity of the multipath signals. In the transform domain, clusters of multipath components are identified. Then, we make use of the PSO to perturb the location of each grid point that reside in each cluster separately and conduct an orthogonal matching pursuit (OMP) [66] to reconstruct sparse multipath sources.

1.2 Organization of the Thesis

The organization of the thesis is as follows. In Chapter 2, wireless communication environment and its key components are given. Then physical and sparse channel models are presented. Lastly, two channel estimation techniques are introduced.

In Chapter 3, a new array signal processing technique is presented to estimate the DOAs, time delays and Doppler shifts of a known waveform impinging onto an array of antennas from several distinct paths. Performance of the proposed technique is compared with other techniques in the literature. Moreover, the performance of the CAF-DF technique is tested on recorded real ionospheric data.

A novel transform domain array signal processing technique based on PSO and CAF computation is presented in Chapter 4 for identification of multipath communication channels. Detailed analysis and simulation results are provided.

In Chapter 5, CS and sparse approximation theory is reviewed. Then, off-grid problem in sparse signal recovery is introduced. To alleviate this problem, a new algorithm is developed based on the CS theory, PSO and CAF. The performance of the developed technique is tested and analyzed based on extensive simulations.

Remarks and conclusions are provided in Chapter 6.

In the Appendix, important points and derivations of PSO, CAF and CRLB are provided.

Chapter 2

Wireless Communications

Wireless communications is one of the most important technology of our time that has a profound impact on our society. Today, wireless technology support not only voice telephony but also supports other services such as the transmission of images, text, data and video. The demand for new wireless capacity is increasingly growing. There still exist technical problems that should be solved in wireline communications. However, with the addition of new optical-fiber, switch and router systems, the demand for extra wireline capacity can be fulfilled. On the other side, there exist only two resources; transmitter power and radio bandwidth that can be used to increase the wireless capacity. Both of these resources are limited, unfortunately. Moreover, radio bandwidth is not growing and transmitter power is not improving at rates close to additional demand to wireless capacity.

Fortunately, microprocessor power is growing rapidly. According to Moore's law, microprocessor capability doubles every eight months. Over the past twenty years, accuracy of the law is confirmed and it seems to continue for years. Considering these circumstances, there has been an enormous effort in the last few decades to increase the wireless communication capacity by adding more technology and intelligence to the wireless signal processing algorithms [67]. Efforts in this area can be grouped in two parts; developing new signal transmission techniques and advanced receiver signal processing approaches in order to increase capacity without demanding more power or bandwidth [67].

With a 1.5-trillion dollars market share, the telecommunications industry is one of the largest industries. Mobile (cellular) telephony constitutes the largest section of the telecommunications industry. However, there exists many other wireless technologies that are being deployed worldwide. Some of the most popular examples include Bluetooth, personal area networks (e.g. IEEE 802.15), wireless local area networks (e.g. IEEE 802.11), wireless metropolitan area networks (e.g. IEEE 802.16) and wireless local area networks. These technologies are the key enablers of many different wireless applications, which are extensively used in daily life [68], [69], [70]. To improve the performance of these technologies, there is a strong support for the research and development efforts in signal processing for wireless communications.

Wide spread deployment of many important wireless systems have become possible by the development of a number of transmission, channel assignment and spatial techniques; time division multiple access (TDMA), code division multiple access (CDMA), orthogonal frequency division multiplexing (OFDM), other multi-carrier systems, beamforming and space time coding. Wireless radio channels create severe challenges such as path loss, shadowing, multipath fading, dispersion and interference as a medium for reliable high speed communication. Stated techniques can be chosen to address these kind of physical properties of wireless channels. As a result, advanced receiver signal processing techniques for channel modeling are required in order to take advantage of these transmission techniques, to reduce the deteriorations of the wireless channel by exploiting the diversities of the wireless channel.

In the following sections, we will briefly review the main characteristics of mobile radio propagation and multipath wireless channels.

2.1 Mobile Wireless Propagation

Since most of the wireless systems operate in urban areas, typically there is no direct line of sight (LOS) between the transmitter and the receiver. Transmitted radio signals propagating through the channel arrives at the receiver along a number of different paths. This phenomenon is called as multipath propagation. As illustrated in Fig. 2.1, multipaths arise from reflection, scattering, refraction and diffraction of radiated wave off the objects in the environment [1], [71]. The received signal is much weaker than the transmitted one due to channel losses. Propagation models can be considered in two categories: large-scale (or path loss) propagation models and small-scale (or fading) propagation models. Models that predict the mean signal strength between a transmitter-receiver separation are called the large-scale. These kind of models characterize signal strength over large transmitter-receiver separations. Differently, models that characterize the rapid fluctuations of the received signal strength over short travel distances such as a few wavelengths are called small-scale fading. To illustrate the effect of large scale and small scale fading on the received power, a measurement obtained in an indoor radio channel communication system is shown in Fig. 2.2. When the mobile receiver moves, signal fluctuates rapidly (small-scale fading). However, average signal changes gradually (large-scale fading) with distance. In this thesis, we will focus on the issues related with the small-scale fading.

Small-scale fading is created by constructive and destructive interference of the multiple signal paths between the transmitter and receiver. Signals arriving from different multipaths are combined at the receiver. It has been observed that the combined signals fluctuate in amplitude and phase. This phenomenon can

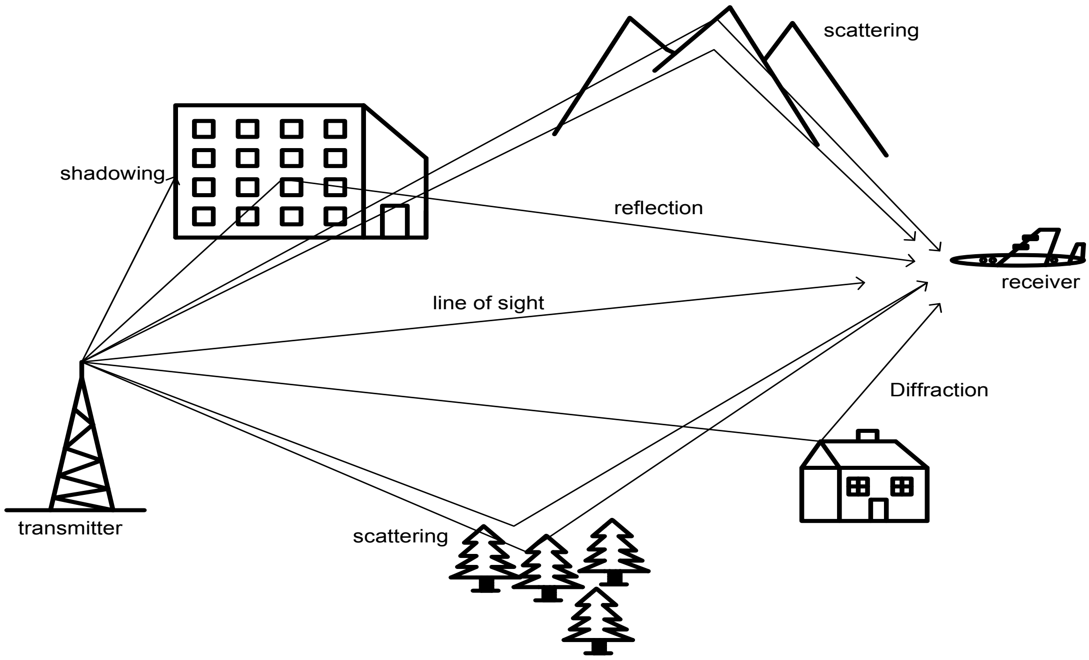

Figure 2.1: Multipath environment. Reflected, scattered, diffracted and line of sight multipath components.

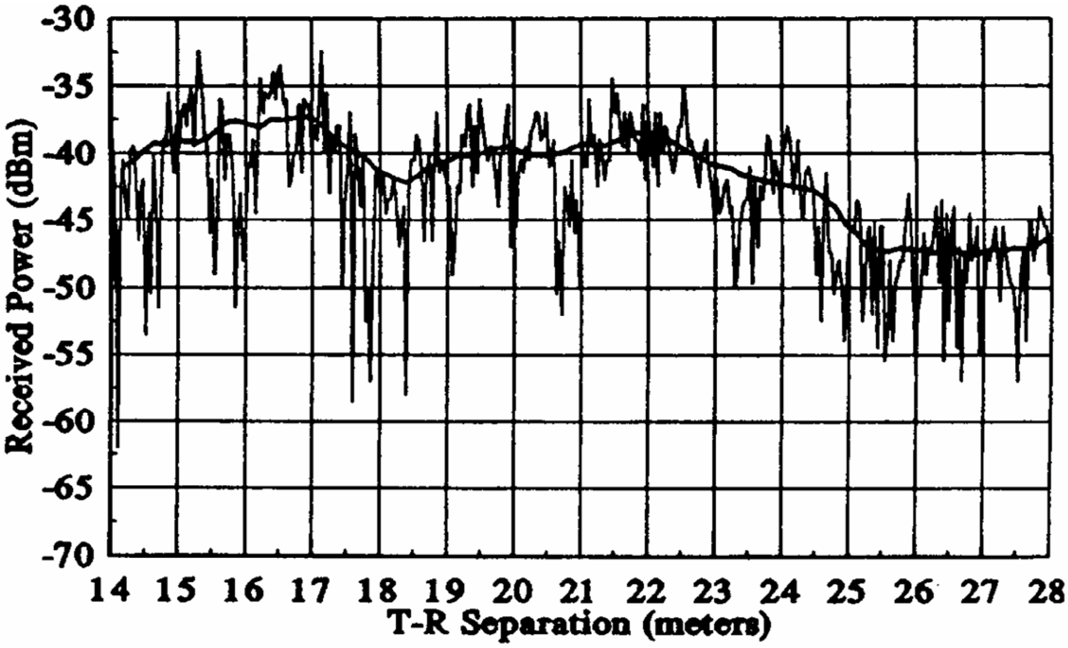

Figure 2.2: Large-scale and small-scale fading for an indoor communication system. Rapid signal fades are small-scale fading. Local average signal changes are large-scale fading [1].

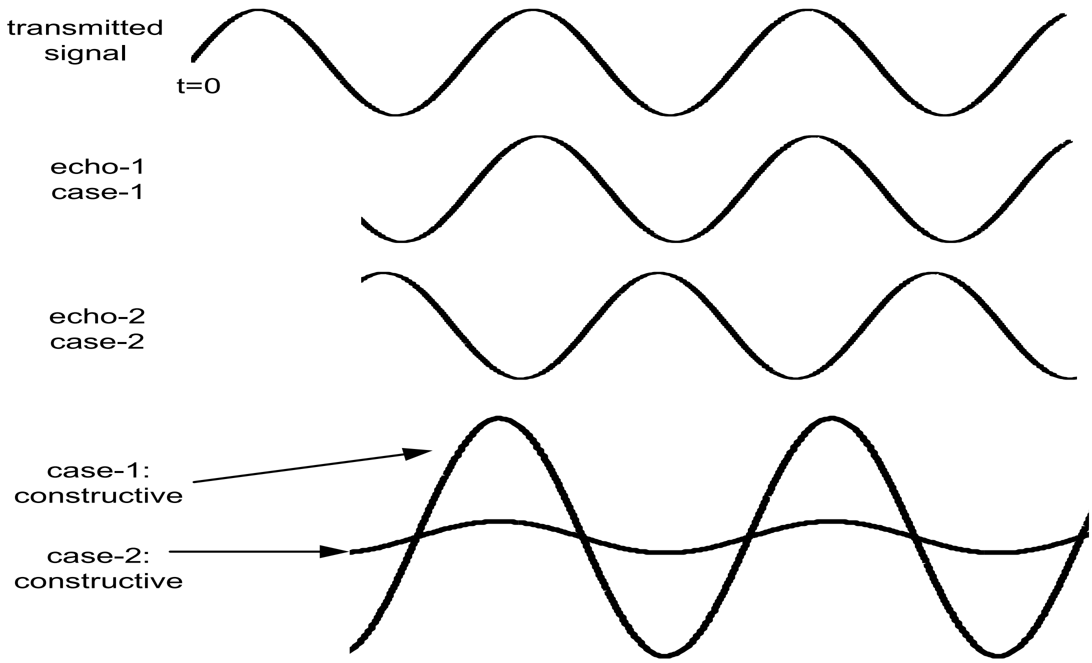

Figure 2.3: Two echoes of a transmitted signal are constructively and destructively added.

be illustrated with two different scenarios. Consider a static multipath situation where a narrowband signal is transmitted and several echoes impinge on the receiver from two different paths as in Fig. 2.3. Superposition of the components can either be constructive (case-1) or destructive (case-2) depending on the relative phases between the signals arriving from different multipaths. Secondly, in a dynamic multipath situation where relative motion between mobile and base station results in random frequency modulation, spatial location of paths continuously change and therefore relative phase shifts change. As shown in Fig. 2.4, the received signal amplitude changes in the case of two paths whose phases change with the position of the receiver.

Related with relative motion between the base station and mobile, the rate of change of phase is apparent as Doppler shift. This very important physical phenomenon can be summarized as follows. With a constant velocity v, a mobile is moving along a path and receiving signal from the base station as illustrated in Fig. 2.5. The phase change in the received signal due to the path length

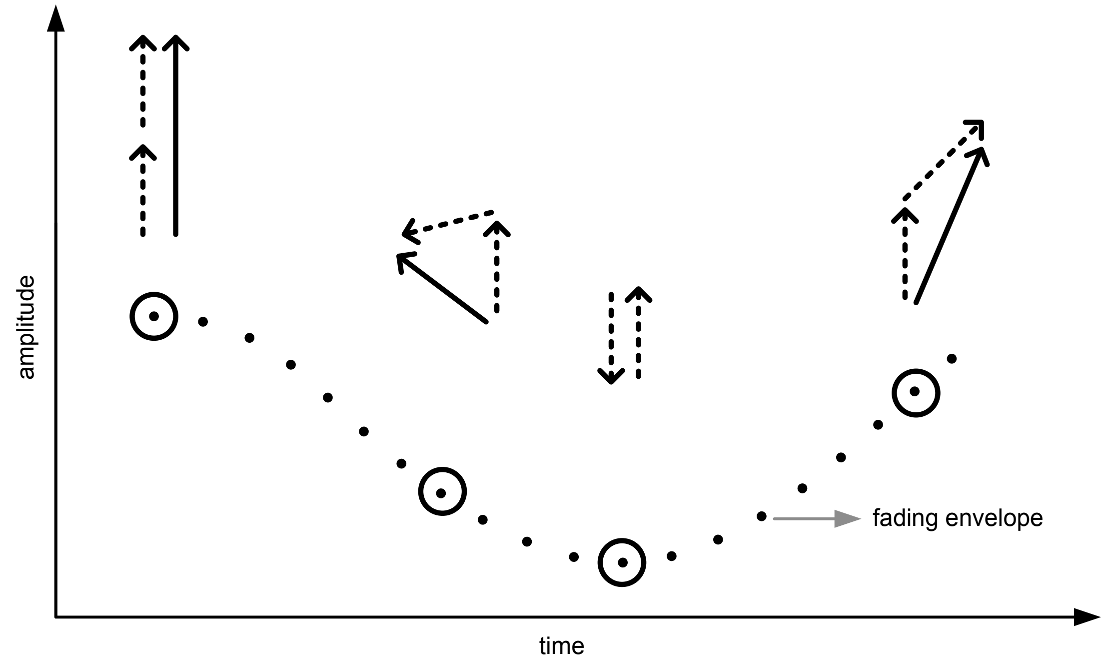

Figure 2.4: Envelope fading when two multipath components added with different phases.

difference can be written as

$$\Delta\psi = \frac{2\pi v \Delta t \, \cos\theta}{\lambda} \quad , \tag{2.1}$$

and the corresponding Doppler shift in the frequency is

$$\nu = \frac{\Delta\psi}{2\pi\Delta t} = \frac{v \, \cos\theta}{\lambda} \quad . \tag{2.2}$$

With this equation, we have related Doppler shift with the mobile velocity and the angle between mobile direction and the arriving signal direction.

2.2 Characteristics of Mobile Multipath Communication Channel parameters

Power delay profiles plays a crucial role in modeling mobile multipath channel. These profiles are obtained to find the average small-scale power delay profile in a local area by averaging instantaneous power delay profile measurements. In 450

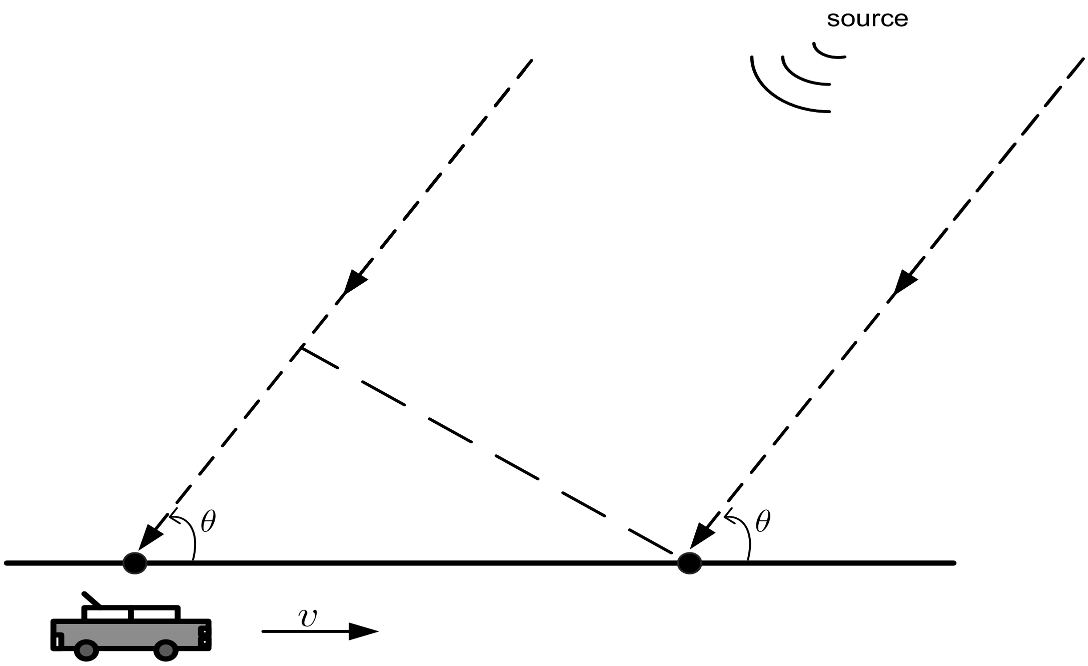

Figure 2.5: Doppler effect illustration. Far-field signal impinges on the antenna of a moving car and reflects off.

MHz - 6 GHz range channel measurements, based on time resolution and type of the channel, it is generally assumed that sampling at spatial separations of $\lambda/4$ and over mobile receiver movements smaller than 6 m for outdoor channels and smaller than 2 m for indoor channels. Using such a dense sampling compensates the bias, which is due to large-scale averaging, in the resulting statistics of small-scale. Typical power delay profiles obtained from indoor and outdoor channels are seen in Fig. 2.6, 2.7.

2.2.1 The Delay Spread

In a multipath channel, multiple delayed and scaled echoes of the transmitted signal arrive at the receiver. Typically, a double negative exponential model, where the delay separation between multipaths increases exponentially with path delay and the multipath amplitudes decrease exponentially with delay, shows a reasonable agreement with the observed data [72], [73], [74]. The delay spread is

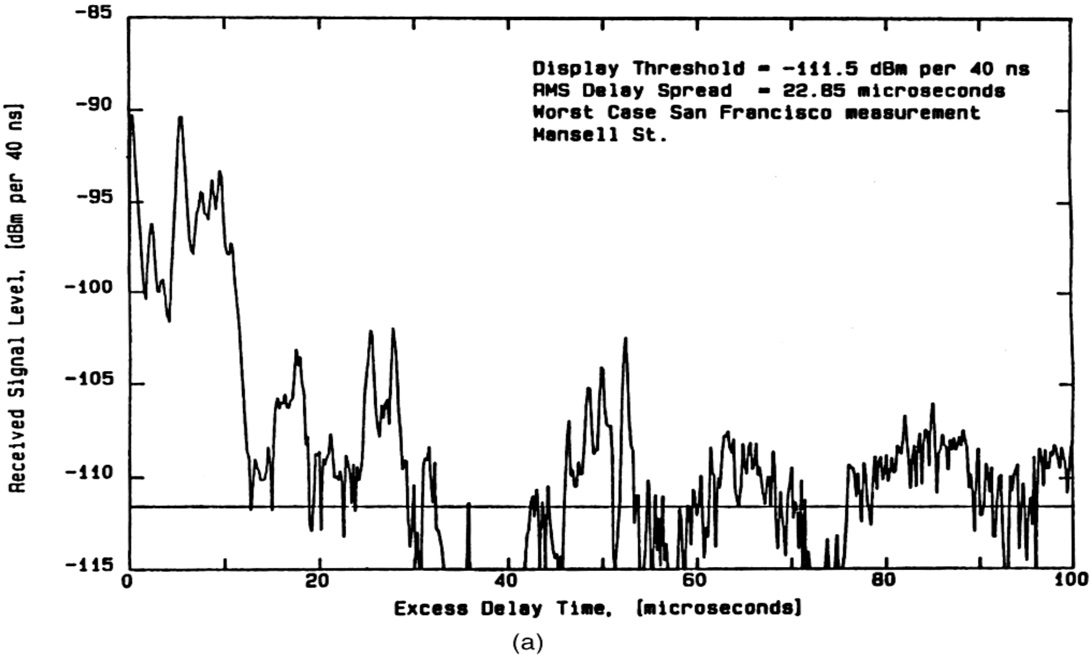

Figure 2.6: Multipath power delay profile recorded from a 900 MHz cellular system. [2].

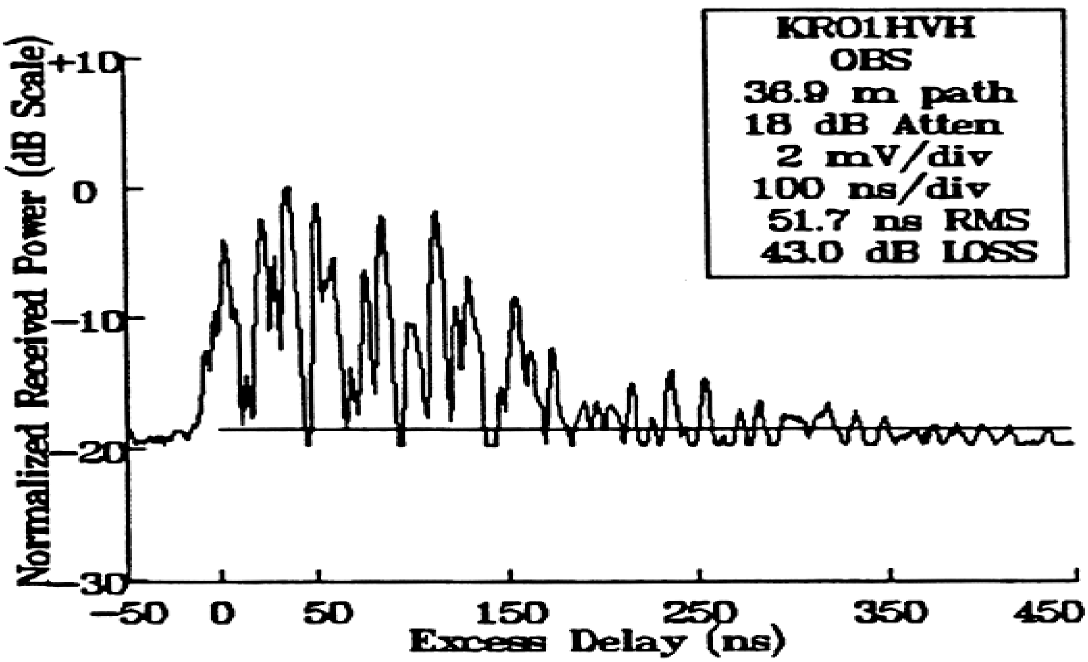

Figure 2.7: Multipath power delay profile recorded from a 4 GHz indoor environment [3].

defined as the range of delays of discernible multipath components. Power delay profiles provide us information about time dispersive structure of the multipath channels. The mean excess delay ($\bar{\tau}$) and rms delay spreads (σ_τ) are two important multipath channel parameters that quantify the time dispersive properties of wideband channels. The mean excess delay is defined as:

$$\bar{\tau} = \frac{\sum_i P(\tau_i)\tau_i}{\sum_i P(\tau_i)} \quad , \tag{2.3}$$

and the rms delay spread is defined as

$$\begin{aligned} \sigma_\tau &= \sqrt{\frac{\sum_i P(\tau_i)\tau_i^2}{\sum_i P(\tau_i)} - (\bar{\tau})^2} \\ &= \sqrt{\bar{\tau^2} - (\bar{\tau})^2} \quad , \end{aligned} \tag{2.4}$$

where P is the relative power level and τ_i is the measured relative delay with respect to initial time τ_0 [1]. In outdoor multipath communication channels, typical rms delay spread values are on the order of microseconds and in indoor channels it is on the order of nanoseconds. Another multipath channel parameter is the maximum excess delay (Q dB), which is the time delay during maximum multipath energy falls Q dB. For example, in Fig. 2.8, after 84 ns, which is here maximum excess delay (10 dB), maximum power level at 0 dB is decreased to -10 dB. The maximum excess delay is sometimes called as the excess delay spread of a power delay profile and defines the time duration of the multipath which is above a specific threshold. In Fig. 2.8, determination of reviewed multipath channel parameters are presented for an indoor power delay profile.

2.2.2 The Coherence Bandwidth

Similar to the delay spread parameters, that are used to characterize the multipath channel in time, coherence bandwidth (BW_{coh}) is used to characterize the multipath channel in the frequency domain. Coherence bandwidth can be defined as the range of frequencies in which channel is flat. For example, assume

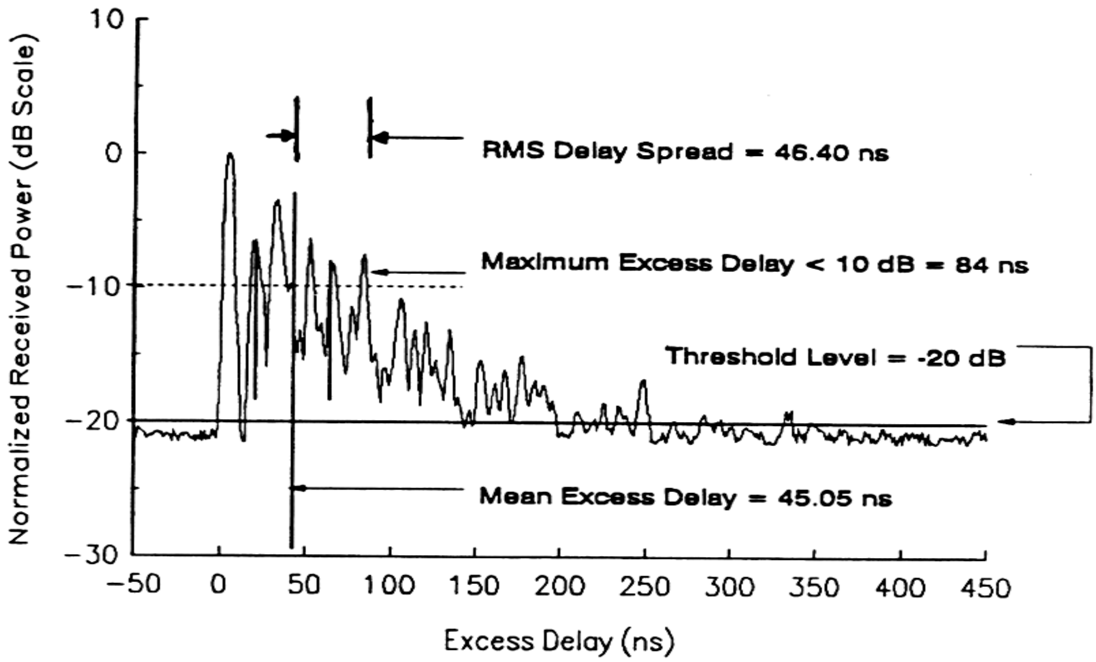

Figure 2.8: Indoor power delay profile: rms delay spread, mean excess delay, maximum excess delay (10dB) and threshold level is seen. [1].

that there exist two multipath components having frequency separation which is greater than BW_{coh}. Then, these two components is expected to be affected very differently by the channel. The coherence bandwidth and the rms delay spread are inversely proportional to each other.

$$BW_{coh} \approx \frac{1}{\sigma_\tau} \quad . \tag{2.5}$$

This is a very rough approximation and exact relation between these two parameters is a function of the multipath channel structure and the transmitted signals. Detailed analysis and extensive simulations are needed to understand the effect of the time varying multipath channel on application specific transmitted signal. Therefore, in order to have high data rate wireless communications with specific modems, very accurate multipath channel models are required [75], [76].

2.2.3 Doppler Spread

Time dispersive structure of the multipath channel is expressed with the previously described parameters delay spread and coherence bandwidth. In this section we will describe Doppler spread (B_d) and coherence time (T_{coh}) that are used to express the time varying, which is caused by movement of scatters, reflectors and relative motion between the base station and mobile, structure of the multipath channels. Doppler spread is defined as the spectral broadening caused by the Doppler shift. Coherence time, which is inversely proportional to maximum Doppler shift, is used to describe the time varying structure of the frequency dispersion in the multipath channel. Relation between these two parameters is:

$$T_{coh} \approx \frac{1}{\nu_{max}} \quad . \tag{2.6}$$

In other words, the coherence time is the time duration over which the impulse response of the channel is approximately the same. Therefore, it can be said that two multipath components are affected differently by the channel if time difference of arrivals are larger than T_{coh}.

2.3 The Small Scale Fading Categories

In this section, we will summarize the types of small scale fading due to multipath delay spread and Doppler spread. Time dispersion causes flat or frequency selective fading. Frequency dispersion causes fast or slow fading.

2.3.1 Flat Fading

If the channel has a constant gain over a bandwidth (BW_{ch}) that is larger than the trasmitted signal bandwidth (BW_s), then the received signal encounter approximately the same amount of fading over the transmission bandwidth. This type of fading is called as flat fading. Flat fading channels are also known as the narrowband channels. In these channels, reciprocal of the transmitted signal bandwidth is much larger than the rms delay spread,

$$\frac{1}{BW_s} \gg \sigma_\tau \quad . \tag{2.7}$$

This means that, all the multipath echoes fall into a single delay bin. These channels may result in deep fades.

2.3.2 Frequency Selective Fading

If the channel has a constant gain over a bandwidth (BW_{ch}) that is smaller than the transmitted signal bandwidth (BW_s), then the received signal encounter fading that varies across frequency, called as frequency selective fading. Frequency selective fading channels are also known as the wideband channels. In these channels, reciprocal of the transmitted signal bandwidth is smaller than the rms delay spread:

$$\frac{1}{BW_s} < \sigma_\tau \quad . \tag{2.8}$$

In frequency selective fading channels, channel can be considered as a linear filter and each multipath component should be modeled. Therefore, modeling of these channels are more challenging than the flat fading channels.

2.3.3 The Fast Fading

If the channel impulse response is rapidly changing within a symbol duration T_s (i.e. reciprocal of the BW_s), then the received signal undergoes what is called as the fast fading. With increasing Doppler spread relative to the transmitted signal bandwidth, the distortion on the received signal increases. The fast fading conditions are

$$BW_s < BW_\nu \tag{2.9}$$

$$T_s > T_{coh} \quad . \tag{2.10}$$

Fast fading is directly related with the rate of change of the multipath channel due to relative motion.

2.3.4 The Slow Fading

When the channel response changes much slower than the baseband transmitted signal, then this channel can be called as the slow fading channel. At that time, the channel can be assumed as almost static over the duration of several symbol durations. Doppler spread is much smaller than the transmitted signal bandwidth. Slow fading conditions are

$$BW_s \gg BW_\nu \tag{2.11}$$

$$T_s \ll T_{coh} \quad . \tag{2.12}$$

To summarize, both the fast and the slow fading are only related with the relationship between the time rate of change in the multipath channel and the transmitted signal. These two terms do not depend on the various losses in the channel.

2.4 Physical Multipath Channel Model

Multipath channels can be modeled as a time varying linear filter. Relative motion of the transmitter and the receiver is the major reason for the time variation. However, even if the transmitter and receiver are stationary, there is a slow variation in the communication channel due to propagation environment. The received signal in the absence of noise can be modeled as:

$$\begin{aligned} x(t) &= \int_0^{\tau_{max}} h(t,\tau)s(t-\tau)d\tau && (2.13)\\ &= \int H(t,f)S(f)e^{j2\pi ft}df && (2.14)\\ &= \int_0^{\tau_{max}} \int_{-\nu_{max}}^{\nu_{max}} C(\tau,\nu)s(t-\tau)e^{j2\pi\nu t}d\nu d\tau \quad , && (2.15) \end{aligned}$$

where $x(t)$ and $s(t)$ represent the received and transmitted signals respectively, and $S(f)$ is the Fourier transform of $s(t)$. The multipath channel is characterized by the time-varying impulse response, $h(t,\tau)$, or the time-varying frequency response, $H(t,f)$:

$$\begin{aligned} H(t,f) &= \int h(t,\tau)e^{-j2\pi f\tau}d\tau && (2.16)\\ &= \sum_{i=1}^{d} \zeta_i e^{-j2\pi f\tau_i} e^{j2\pi\nu_i t} \quad , && (2.17) \end{aligned}$$

or the delay-Doppler spreading function, $C(\tau,\nu)$ [77]. Delay-Doppler spreading function can be written as

$$C(\tau,\nu) = \sum_{i=1}^{d} \zeta_i \delta(\tau-\tau_i)\delta(\nu-\nu_i). \qquad (2.18)$$

where d is the number of multipath components, $\zeta_i \in \mathbb{C}$, $\nu_i \in [-\nu_{max}, \nu_{max}]$, and $\tau_i \in [0, \tau_{max}]$ are the complex path gain, the delay and the Doppler shift associated with the i^{th} multipath component, respectively. Therefore, in a discrete physical multipath channel model, the received signal is modeled as:

$$x(t) = \sum_{i=1}^{d} \zeta_i s(t-\tau_i)e^{j2\pi\nu_i t} \quad . \qquad (2.19)$$

At this point, it is very informative to focus on the discretization of the multipath channel in delay. Discrete delay intervals are called the excess delay bins and can be denoted as $\Delta\tau$. For instance, the first multipath component has a delay of $\tau_1 = \Delta\tau$ and the i^{th} multipath component has a delay of $\tau_i = i\Delta\tau$, for $i = 0, ..., N-1$, where N is the total number of possible excess delay bins. All the multipath components that are received within the i^{th} bin are considered to have a single resolvable multipath component having delay τ_i.

There may be several multipath components arriving within an excess delay bin and combining to yield the instantaneous amplitude and phase of a single modeled multipath signal, depending on the channel delay properties and $\Delta\tau$ choice. This situation results in fading of the multipath amplitude within an excess delay bin. On the other hand, if there is only one multipath component arriving within an excess delay bin, then the amplitude for that particular time delay will not fade significantly [1]. A receiver with bandwidth BW_{rx} cannot distinguish between echoes arriving in τ_i and $\tau_i + \Delta\tau$, if $\Delta\tau \ll 1/BW_{rx}$. It is sufficient to consider this condition with $\Delta\tau = BW_{rx}$, which corresponds to time-delay resolution, for many qualitative considerations [71]. Here, maximum excess delay of the multipath channel is taken as $N\Delta\tau$, which is larger than the expected delay spread of the channel. In the following, we will further generalize the presented channel model to include the effects of DOA of each multipath component using multiple antennas at the receiver.

Antenna arrays consists of a set of antennas that are spatially distributed at known positions with reference to a common reference point [78]. The propagating signals are simultaneously sampled and collected by the receiver at each antenna. The transmitted waveforms undergo some modifications, depending on the path of propagation and the antenna characteristics.

Usually, the direction and the speed of the propagation are defined by a vector $\boldsymbol{\alpha}$ in (2.20) which is called the slowness vector. Using the reference coordinate

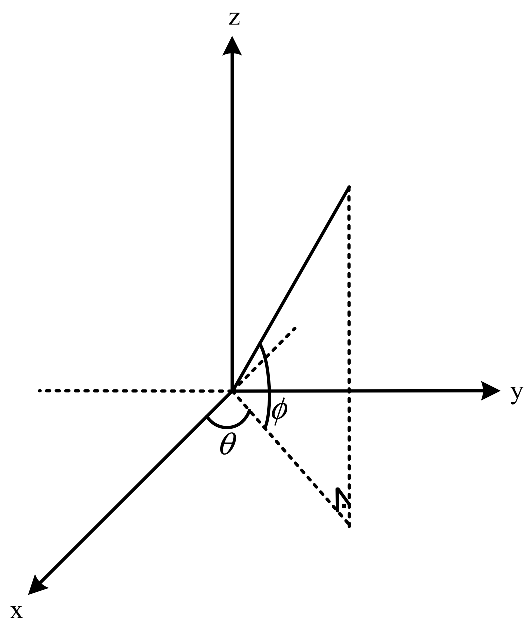

Figure 2.9: Direction of the signal and reference coordinate system.

system in Fig. 2.9, the slowness vector is

$$\boldsymbol{\alpha} = \frac{1}{c}[\cos\phi\cos\theta \; ; \; \cos\phi\sin\theta \; ; \; \sin\phi] \quad , \tag{2.20}$$

where θ is the azimuth angle, ϕ is the elevation angle and c is the speed of light. In Fig. 2.10, a circular array geometry is shown. Position of each antenna can be represented by a vector as:

$$\boldsymbol{r_m} = [x_m \; ; \; y_m \; ; \; z_m] \tag{2.21}$$

$$= [r_m \sin(\theta_m) \; ; \; r_m \cos(\theta_m) \; ; \; 0] \quad , \tag{2.22}$$

and the propagation direction of each impinging signal is represented by unit vector

$$\boldsymbol{\alpha}_i = \frac{1}{c}[x_i \; ; \; y_i \; ; \; z_i] \quad i = 1, ..., d \quad . \tag{2.23}$$

By using the antenna coordinate system and the propagation directions of each multipath component, the relative phase of the m^{th} sensor due to i^{th} impinging signal with respect to the origin of the sensor array can be written in cartesian

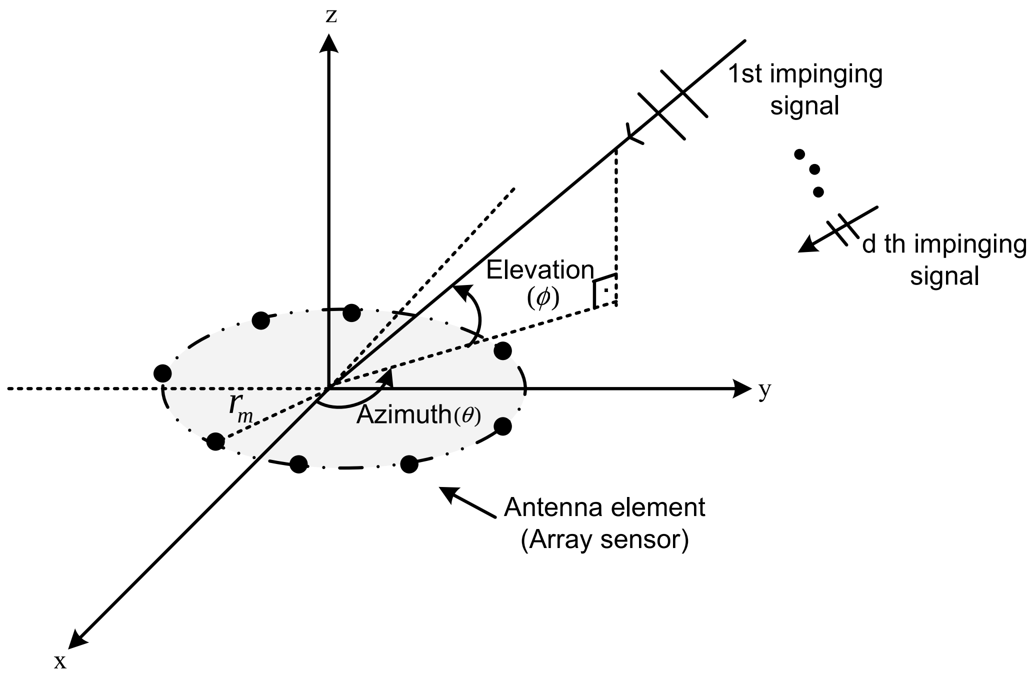

Figure 2.10: d multipath components impinge onto an uniformly spaced circular antenna array and multipath enviroment.

coordinates as:

$$\begin{aligned}
\xi_{m,i}(\theta,\phi) &= \boldsymbol{\alpha}_i \cdot \boldsymbol{r_m} \\
&= \frac{1}{c}\begin{bmatrix}\cos(\theta_i)\cos(\phi_i) \\ \sin(\theta_i)\cos(\phi_i) \\ \sin(\phi_i)\end{bmatrix} \cdot \begin{bmatrix} r_m\cos(\theta_m) \\ r_m\sin(\theta_m) \\ 0\end{bmatrix} \\
&= \frac{1}{c}\left[r_m\cos(\theta_i)\cos(\phi_i)\cos(\theta_m) + r_m\sin(\theta_i)\cos(\phi_i)\sin(\theta_m)\right] \quad . \qquad (2.24)
\end{aligned}$$

Without the carrier term $\exp(jw_ct)$, where $w_c = 2\pi f_c$, the output is modeled as:

$$x_m(t) = s(t)e^{-j\xi_{m,i}(\theta,\phi)} \qquad (2.25)$$

$$= s(t)a_m(\theta_i,\phi_i) \quad . \qquad (2.26)$$

By using this formulation, the time-varying frequency response given in (2.16) can be expressed as:

$$\mathbf{H}(t,f) = \sum_{i=1}^{d} \zeta_i \mathbf{a}(\theta_i,\phi_i)e^{-j2\pi f\tau_i}e^{j2\pi\nu_i t} \quad . \qquad (2.27)$$

By further combining the pure multipath model given in (2.19) and the spatial aspects of the antenna array, we get the following antenna array output signal:

$$\mathbf{x}(t) = \sum_{i=1}^{d} \zeta_i \mathbf{a}(\theta_i, \phi_i) s(t - \tau_i) e^{j2\pi\nu_i t} \quad , \tag{2.28}$$

where:

- $\mathbf{x}(t) = [x_1(t), ..., x_M(t)]^T$ is the array output and $[.]^T$ is the transpose operator,
- d: number of multipaths,
- $\mathbf{a}(\theta, \phi) = [a_1(\theta, \phi), ..., a_M(\theta, \phi)]^T$ is the $M \times 1$ steering vector of the array along the direction of (θ, ϕ),
- θ_i: azimuth angle of the i^{th} path,
- ϕ_i: elevation angle of the i^{th} path,
- ζ_i: complex scalar, containing the attenuation and phase terms of the i^{th} path,
- τ_i: time delay of the i^{th} path,
- ν_i: Doppler shift of the i^{th} path.

Eq. (2.28) can be written in a more compact form by defining a matrix and a vector of signal waveforms as:

$$\mathbf{x}(t) = \mathbf{D}(t, \boldsymbol{\varphi})\boldsymbol{\zeta} \quad , \tag{2.29}$$

where

$$\mathbf{D}(t, \boldsymbol{\varphi}) = [\mathbf{a}(\theta_i, \phi_i)s(t - \tau_i)e^{j2\pi\nu_i t}, ..., \mathbf{a}(\theta_d, \phi_d)s(t - \tau_d)e^{j2\pi\nu_d t}] \tag{2.30}$$

is an $M \times d$ matrix,

$$\boldsymbol{\zeta} = [\zeta_i, ..., \zeta_d]^T \tag{2.31}$$

is a $d \times 1$ vector containing the attenuation and phase terms of individual paths and channel parameters are collected in the vector $\boldsymbol{\varphi} = [\boldsymbol{\varphi}_1, ..., \boldsymbol{\varphi}_d]$, and $\boldsymbol{\varphi}_i = [\tau_i, \nu_i, \theta_i, \phi_i]$.

Moreover in the presence of noise we reach the well-known representation for the array input-output relation as:

$$\mathbf{x}(t) = \mathbf{D}(t, \boldsymbol{\varphi})\boldsymbol{\zeta} + \mathbf{n}(t) \quad , \tag{2.32}$$

where $\mathbf{n}(t) = [n_1(t), ..., n_M(t)]^T$ is spatially and temporally white circularly symmetric Gaussian noise with variance σ^2.

Lastly, in the end of this section we provide a performance criteria to be evaluated by the parameter estimation techniques used and proposed throughout the thesis. An important performance criterion in multipath channel parameter estimation is the effect of the estimated channel parameters to the performance of the communication receiver system where the estimated channel parameters can be used to form the following decision signal [26]:

$$\hat{\rho} = \int_0^T s^*(t) \left(\sum_{m=1}^{M} \sum_{i=1}^{d} \hat{\zeta}_i^* x_m(t + \hat{\tau}_i) e^{-j2\pi\hat{\nu}_i t} e^{j2\pi\nu_c \xi_{m,i}(\hat{\theta}_i, \hat{\phi}_i)} \right) dt \quad . \tag{2.33}$$

This decision signal is very similar to the decision signal generated by a rake receiver [79]. Here we employed a raking strategy in both delay and Doppler as well as between various DOAs of the multipath components. The estimated SNR of the decision signal given below serves as a performance criterion between alternative techniques:

$$\widehat{\mathrm{SNR}} = \frac{|\hat{\rho}|^2}{\mathrm{E_s M}\sigma^2 \sum_{\mathrm{i=1}}^{\mathrm{d}} |\hat{\zeta}_{\mathrm{i}}|^2} \tag{2.34}$$

where E_s is the transmitted signal energy.

2.5 Sparse Multipath Channel Model

In this section, we will present a virtual channel model for doubly selective channels ($BW\ \tau_{max} \geq 1$, $T\ \nu_{max} \geq 1$) that exploits the relation between the multipath components and the signal space. Canonical model, or also known as virtual channel model, formulize a lower dimensional approximation of the physical multipath channel by uniformly sampling of the delay-Doppler-spatial domain [54], [80]. This alternative modeling exploits the relation between the clustering of multipath components within delay-Doppler-spatial domain and sparsity of degrees of freedom in the multipath channel and prepares the underlying structure to be able to make use of the benefits of the CS theory.

Recent multipath channel measurement results show that multipath components are distributed in as clusters within a defined channel spread and impinge onto a receiver in clusters [17],[81]. In a scattering environment, clusters of multipath components occur due to the large scale scatters such as buildings and hills. Multipath components within a cluster occur due to small scale scatters of the large scale scatters such as windows of buildings. Moreover, most of the practical multipath channels such as ultra-wideband channels [82], high definition digital television channels [83], [84] underwater acoustic channels [85], [86] and broadband wireless communication channels [87] exhibit a clustered sparse structure. There exist various efforts in the literature to clarify the underlying theory of clustered sparsity. Therefore, sparse nature of the multipath channels should be exploited in order to accurately estimate the channel parameters [53].

First of all, for the sake of simplicity and to be able to introduce the main idea clearly, we will provide formulation of the virtual channel model in delay-Doppler domain. Extension to spatial domain is straightforward and can be found in the references [88], [55]. However, we will shortly mention the spatial domain in virtual channel model by the end of this section. Doubly selective multipath

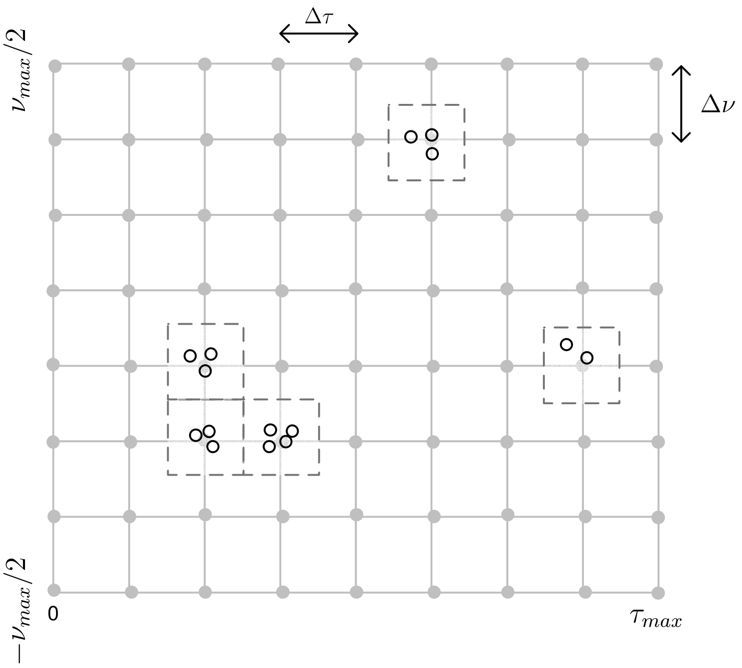

Figure 2.11: An illusration of clustering and virtual channel representation on delay Doppler domain. There exists three clusters of multipath components. Delay resolution is $\Delta\tau$. Doppler resolution is $\Delta\nu$

channels can be classified as either rich or sparse, depending on the separation between different multipath component clusters. The separations are smaller than $\Delta\tau = 1/BW$ and $\Delta\nu = 1/T$ in delay Doppler domain for rich multipath component channels. However in sparse multipath component channels, The separations are larger than $\Delta\tau = 1/BW$ and $\Delta\nu = 1/T$. A virtual multipath channel representation is presented in Fig. 2.11, [89]. In this figure, each small circle corresponds to a multipath component. As can be seen, each delay Doppler bin is of size $\Delta\tau \times \Delta\nu$ and very few of them has a multipath component and, hence, multipath components are sparse in delay-Doppler domain.

Although, physical discrete channel model given in (2.19) is a realistic model, analysis and estimation steps are difficult, due to the presence of large number of parameters, ζ_i, τ_i, ν_i. In situations where we have finite signaling duration and channel bandwidth, discrete multipath model can be approximated by a linear one known as virtual channel model [54]. By uniformly sampling the physical multipath environment in both delay with $\Delta\tau = 1/BW$ and in Doppler with

$\Delta\nu = 1/T$, a lower dimensional approximation of the discrete multipath model can be obtained. The corresponding discrete model is:

$$H(t,f) = \sum_{k=0}^{K-1} \sum_{p=-P}^{P} \mathcal{H}(k,p) e^{j2\pi \frac{p}{T} t} e^{-j2\pi \frac{k}{BW} f} \quad . \tag{2.35}$$

The virtual channel coefficients can be related to the continuous channel model as:

$$\mathcal{H}(k,p) = \frac{1}{T\ BW} \int_0^T \int_{-BW/2}^{BW/2} H(t,f) e^{j2\pi \frac{p}{T} t} e^{-j2\pi \frac{k}{BW} f} dt\ df \quad . \tag{2.36}$$

Number of resolvable delay and Doppler cells in each dimension are:

$$K = \left\lceil \frac{\tau_{max}}{\Delta\tau} \right\rceil + 1 = \lceil BW \tau_{max} \rceil + 1 \tag{2.37}$$

$$P = \left\lceil \frac{\nu_{max}}{2\Delta\nu} \right\rceil + 1 = \lceil T\nu_{max}/2 \rceil + 1 \quad . \tag{2.38}$$

Hence, in the simplified model, the channel is characterized with the virtual channel coefficients $\mathcal{H}(k,p)$, K and P only. Physical and virtual channel models can be related with each other by substituting (2.16) into (2.36) as [90]:

$$\mathcal{H}(k,p) = \sum_{i=1}^{d} \zeta_i e^{-j\pi(p-\nu_i T)} \mathrm{sinc}(p - \nu_i T) \mathrm{sinc}(k - \tau_i BW) \tag{2.39}$$

$$\approx \sum_{i \in S_{\tau,k} \bigcap S_{\nu,p}} \zeta_i \quad , \tag{2.40}$$

where $S_{\tau,k} \bigcap S_{\nu,p}$ is the set of all multipath components whose delays and Doppler's are inside of a delay-Doppler resolution cell of size $\Delta\tau \times \Delta\nu$ and centered on the k^{th} virtual delay ($\frac{k}{BW}$) and p^{th} virtual Doppler shift ($\frac{p}{T}$). Set $S_{\tau,k} \bigcap S_{\nu,p}$ is defined as:

$$S_{\tau,k} = \left\{ i \ : \ \left| \tau_i - \frac{k}{BW} \right| < \frac{1}{2BW} \right\} \tag{2.41}$$

$$S_{\nu,p} = \left\{ i \ : \ \left| \nu_i - \frac{p}{T} \right| < \frac{1}{2T} \right\} \quad . \tag{2.42}$$

By using the given sampled virtual channel representation, approximation of (2.19) can be written as:

$$
\begin{aligned}
x(t) &= \sum_{i=1}^{d} \zeta_i s(t-\tau_i) e^{j2\pi\nu_i t} && (2.43)\\
&\approx \sum_{k=0}^{K-1} \sum_{p=-P}^{P} \mathcal{H}(k,p) s\left(t - \frac{k}{BW}\right) e^{j2\pi \frac{p}{T} t}. && (2.44)
\end{aligned}
$$

Therefore, we can say that the virtual model given above approximately represents the physical discrete doubly selective multipath channel in terms of an N_h dimensional parameter vector containing the virtual channel coefficients $\mathcal{H}(k,p)$. N_h is defined as:

$$
\begin{aligned}
N_h &= K\ (2P+1) && (2.45)\\
&= (2\lceil T\nu_{max}/2\rceil + 1)(\lceil BW\tau_{max}\rceil + 1) && (2.46)\\
&\approx \tau_{max}\nu_{max}TBW && (2.47)\\
&\approx \tau_{max}\nu_{max}N_b\ \ . && (2.48)
\end{aligned}
$$

Finally, if we introduce the spatial dimension to the model, the virtual multipath channel model approximation of (2.27) can be extended as:

$$
\begin{aligned}
\mathbf{H}(t,f) &\approx \sum_{m_e=1}^{M_e} \sum_{m_a=1}^{M_a} \sum_{k=0}^{K-1} \sum_{p=-P}^{P} \mathcal{H}(m_a,m_e,k,p)\mathbf{a}\left(\frac{m_e}{M_e}, \frac{m_a}{M_a}\right)\\
&\cdot\ e^{j2\pi\frac{p}{T}t} e^{-j2\pi\frac{k}{BW}f} && (2.49)\\
\mathcal{H}(m_a,m_e,k,p) &= \frac{1}{M_e M_a TBW} \int_0^T \int_{-BW/2}^{BW/2} \mathbf{a}\left(\frac{m_e}{M_e}, \frac{m_a}{M_a}\right)^H\\
&\cdot\ \mathbf{H}(t,f) e^{j2\pi\frac{p}{T}t} e^{-j2\pi\frac{k}{BW}f} dt\ df\ \ . && (2.50)
\end{aligned}
$$

Virtual path partitioning is presented in Fig. 2.12. For the sake of clarity, we will focus on only virtual model in delay-Doppler domain in Section 5.

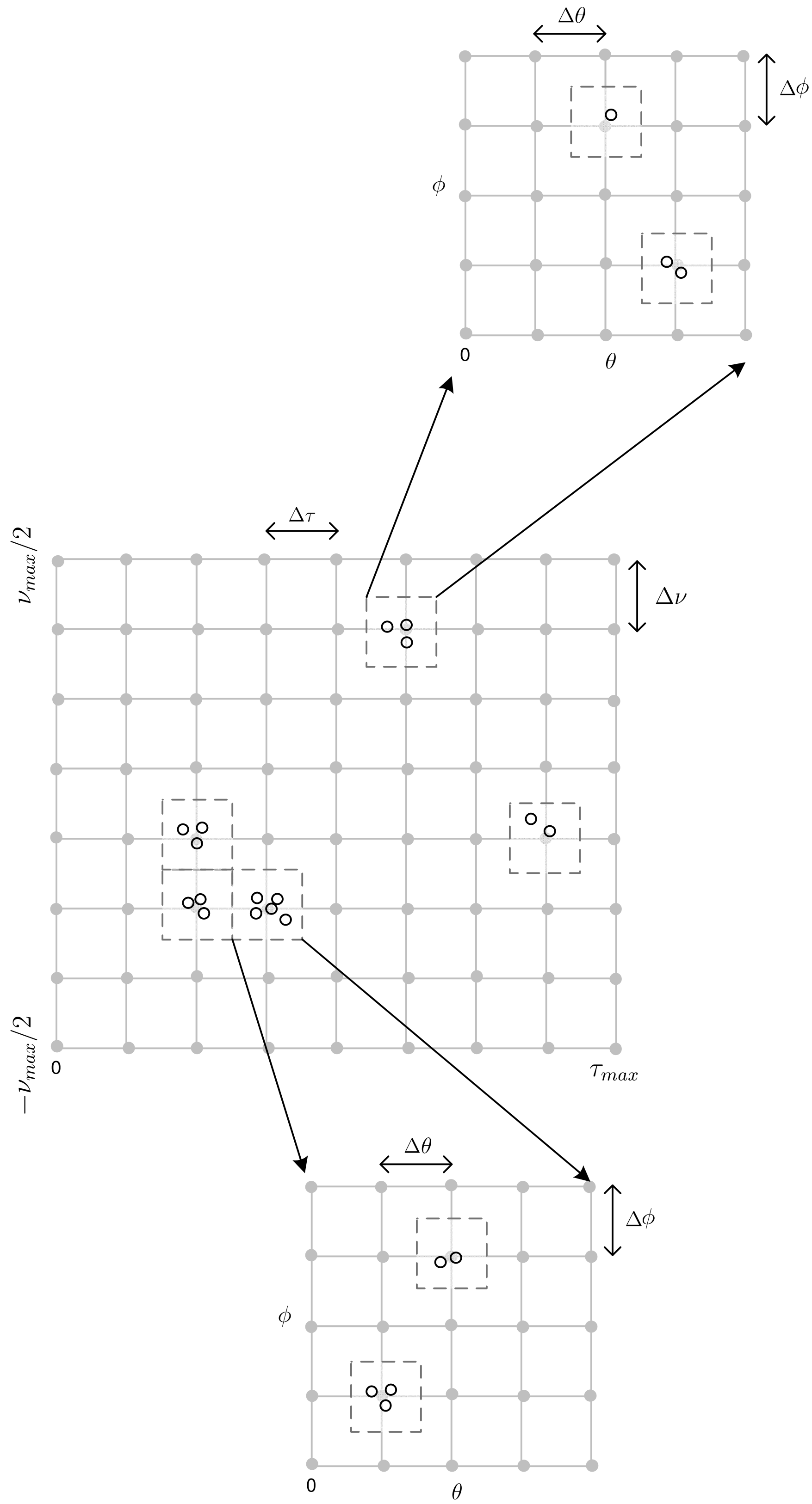

Figure 2.12: An illusration of clustering and virtual channel representation on delay-Doppler and spatial domain. Delay resolution is $\Delta\tau$. Doppler resolution is $\Delta\nu$. Elevation and azimuth resolution are $\Delta\phi$ and $\Delta\theta$, respectively.

2.6 Maximum-Likelihood (ML) Based Multipath Channel Estimation

Maximum likelihood (ML) estimation is a commonly used approach to channel parameter estimation. Assuming that the noise on each pulse transmission are independent, the probability density function of the observations can be obtained as:

$$P[\mathbf{x}(t_1) \quad ... \quad \mathbf{x}(t_N)] = \prod_{k=1}^{N} \frac{1}{\mid \pi\sigma^2 \mathbf{I} \mid} e^{-[\|\mathbf{e}(t_k)\|^2/\sigma^2]} \quad , \tag{2.51}$$

where $|\cdot|$ represents the determinant, $\|\cdot\|$ represents the norm, and

$$\begin{aligned} \mathbf{e}(t_k) &= \mathbf{x}(t_k) - \sum_{i=1}^{d} \mathbf{a}(\theta_i, \phi_i)\zeta_i s(t_k - \tau_i) e^{j2\pi\nu_i t_k} \\ &= \mathbf{x}(t_k) - \mathbf{D}(t_k, \boldsymbol{\varphi})\boldsymbol{\zeta} \quad . \end{aligned} \tag{2.52}$$

The ML estimates that maximize the likelihood function can be written as the maximum of the log-likelihood function:

$$\left[\hat{\boldsymbol{\varphi}}, \hat{\boldsymbol{\zeta}}\right] = \arg \max_{\boldsymbol{\varphi},\boldsymbol{\zeta}} \left\{ -\mathrm{NMlog}\pi\sigma^2 - \frac{1}{\sigma^2} \sum_{\mathrm{k}=1}^{\mathrm{N}} \|\mathbf{e}(\mathrm{t_k})\|^2 \right\}, \tag{2.53}$$

or equivalently

$$\left[\hat{\boldsymbol{\varphi}}, \hat{\boldsymbol{\zeta}}\right] = \arg \min_{\boldsymbol{\varphi},\boldsymbol{\zeta}} \left\{ \sum_{\mathrm{k}=1}^{\mathrm{N}} \|\mathbf{e}(\mathrm{t_k})\|^2 \right\}. \tag{2.54}$$

Given the path parameters $\boldsymbol{\varphi}$, path scaling parameters $\boldsymbol{\zeta}$ can be obtained in closed form as:

$$\hat{\boldsymbol{\zeta}} = \left(\mathbf{D}(t_k, \boldsymbol{\varphi})^H \mathbf{D}(t_k, \boldsymbol{\varphi})\right)^{-1} \mathbf{D}(t_k, \boldsymbol{\varphi})^H \mathbf{x}(t_k) \quad , \tag{2.55}$$

where $(\cdot)^H$ denotes conjugate transpose. Therefore, by substituting (2.55) into (2.52), the ML optimization can be reduced to the following optimization problem over the path parameters, $\boldsymbol{\varphi}$, only:

$$[\hat{\boldsymbol{\varphi}}] = \arg \min_{\boldsymbol{\varphi}} \left\{ \sum_{\mathrm{k}=1}^{\mathrm{N}} \|\mathbf{x}(\mathrm{t_k}) - \mathbf{P}_{\mathbf{D}(\mathrm{t_k},\boldsymbol{\varphi})}\mathbf{x}(\mathrm{t_k})\|^2 \right\}, \tag{2.56}$$

where $\mathbf{P}_{\mathbf{D}(t_k,\boldsymbol{\varphi})}$ is the projection operator onto the space spanned by the columns of $\mathbf{D}(t_k, \boldsymbol{\varphi})$:

$$\mathbf{P}_{\mathbf{D}(t_k,\boldsymbol{\varphi})} = \mathbf{D}(t_k, \boldsymbol{\varphi}) \left(\mathbf{D}(t_k, \boldsymbol{\varphi})^H \mathbf{D}(t_k, \boldsymbol{\varphi})\right)^{-1} \mathbf{D}(t_k, \boldsymbol{\varphi})^H \ . \tag{2.57}$$

A more compact form of (2.56) can be given as:

$$[\hat{\boldsymbol{\varphi}}] = \arg \max_{\boldsymbol{\varphi}} \left\{ \sum_{\mathrm{k}=1}^{\mathrm{N}} \|\mathbf{P}_{\mathbf{D}(\mathrm{t_k},\boldsymbol{\varphi})} \mathbf{x}(\mathrm{t_k})\|^2 \right\} . \tag{2.58}$$

Therefore, one needs to find the global maximum of this $4 \times d$ dimensional optimization problem to identify all 4 parameters for each path. For large number of multipaths that are common to urban and indoor communication, computational complexity of direct maximization becomes prohibitively high.

One of the most popular approach to obtain more efficient ML estimates is the EM algorithm [14]. EM is an iterative method for solving the ML estimation problem in situations where a part of the observations are missing. In estimation of superimposed signals in white Gaussian noise, EM algorithm has been used [91]. To further improve the speed of convergence of the EM approach, SAGE algorithm has been proposed [15]. Each iteration of the algorithm contain EM iteration phase where some of the parameters are fixed at the previous iteration values, while other parameters are re-estimated. Instead of simultaneous parameter estimation, parameters are estimated sequentially. In order to reduce the complexity of the algorithm, suboptimal but faster one dimensional optimization procedures along each parameter are used. In Table 2.1, the basic form of the SAGE algorithm is presented [19].

Formulization of the SAGE algorithm relies on two crucial points of unobservable (complete) and observable (incomplete) data. In Fig. 2.13, relation between observable and unobservable data is seen. Considering the model given in (2.32), complete data can be defined as follows:

$$\begin{aligned} \mathbf{z}_i(t) &= \zeta_i \mathbf{a}(\theta_i, \phi_i) s(t - \tau_i) e^{j2\pi\nu_i t} + \mathbf{n}_i(t) \\ &= \mathbf{u}_i(t) + \mathbf{n}_i(t) \qquad i = 1, .., i, ..., d \ . \end{aligned} \tag{2.59}$$

Table 2.1: Basic SAGE algorithm

Initialize the algorithm.
for $j = 1$; $j \leq$ max. # iterations ; $j = j + 1$
for $i = 1$; $i \leq d$; $i + +$
- Expectation step: estimate the complete (unobservable) data of i^{th} signal path.
- Maximization step: estimate each parameter of i^{th} signal path sequentially by maximizing a properly chosen cost function.
- Create a copy of the i^{th} signal path with estimated parameters.
- Subtract the copy signal from each antenna output.
end
end

The received signal called as incomplete data and it is related to complete data by

$$\mathbf{x}(t) = \sum_{i=1}^{d} \mathbf{z}_i(t) \quad . \tag{2.60}$$

The SAGE algorithm can be divided into two parts namely; expectation and maximization phases. In the expectation phase, complete data can be formed as:

$$\hat{\mathbf{z}}_i(t;\eta) = \mathbf{x}(t) - \sum_{\gamma=1,\gamma\neq i}^{d} \hat{\mathbf{u}}(t;\varphi_i(\eta)) \tag{2.61}$$

where η is the algorithm iteration index. In the first iteration, $\eta = 1$, $\hat{\mathbf{z}}_i(t;\eta)$ is initialized as $\hat{\mathbf{z}}_i(t;\eta) = \mathbf{x}(t)$. Once the complete information is formed, the maximization phase takes place to yield a new set of parameter estimates for each multipath component by using the following equations:

$$\hat{\tau}_i(\eta) = \arg \max_{\tau} \left\{ \left| \mathbf{g}_i(\tau, \hat{\theta}(\eta-1), \hat{\phi}(\eta-1), \hat{\nu}(\eta-1); \hat{\mathbf{z}}_i(t;\eta-1)) \right| \right\} \tag{2.62}$$

$$\hat{\theta}_i(\eta), \hat{\phi}_i(\eta) = \arg \max_{\theta,\phi} \{ |\mathbf{g}_i(\hat{\tau}(\eta), \theta, \phi, \hat{\nu}(\eta-1); \hat{\mathbf{z}}_i(t;\eta-1))| \} \tag{2.63}$$

$$\hat{\nu}_i(\eta) = \arg \max_{\nu} \left\{ \left| \mathbf{g}_i(\hat{\tau}(\eta), \hat{\theta}(\eta), \hat{\phi}(\eta), \nu; \hat{\mathbf{z}}_i(t;\eta-1)) \right| \right\} \tag{2.64}$$

$$\hat{\zeta}_i(\eta) = \frac{\mathbf{g}_i(\hat{\tau}(\eta), \hat{\theta}(\eta), \hat{\phi}(\eta), \hat{\nu}(\eta); \hat{\mathbf{z}}_i(t;\eta-1))}{s(t)s(t)^H \|\mathbf{a}(\hat{\theta}(\eta), \hat{\phi}(\eta))\|^2} \quad . \tag{2.65}$$

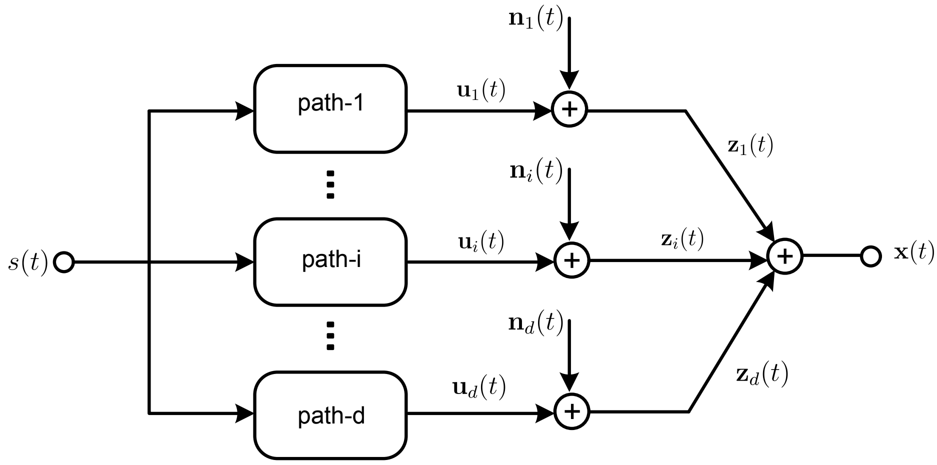

Figure 2.13: Relation between observable and unobservable data.

In these equations, $\mathbf{g}_i(\tau, \theta, \phi, \nu; \mathbf{z}_i(t))$ is defined as:

$$\mathbf{g}_i(\tau, \theta, \phi, \nu; \mathbf{z}_i(t)) \triangleq \sum_{m=1}^{M} \int_{-\infty}^{\infty} s^H(t-\tau) z_{m,i}(t) e^{-j2\pi\nu t} e^{\xi_m(\theta,\phi)} dt \quad . \tag{2.66}$$

There are various methods to initialize the algorithm. One can use MUSIC algorithm to provide initial time-delay values and then for the remaining signal parameters initialization iterations of the SAGE can be used. In this paper, a different initialization procedure is preferred [19]. Since, initially, phase of the complex amplitudes ζ_{m_i} are not known, time-delays and DOAs are estimated incoherently. For this purpose, in the initialization part, maximization procedures used for time-delay and DOA estimations given in (2.62) and (2.63) are changed with the equations below.

$$\hat{\tau}_i(\eta) = \arg \max_{\tau} \left\{ \sum_{m=1}^{M} \left| \int_{-\infty}^{\infty} s^H(t-\tau) \hat{z}_{m,i}(t,0) dt \right|^2 \right\} \tag{2.67}$$

$$\hat{\theta}_i(\eta), \hat{\phi}_i(\eta) = \arg \max_{\theta,\phi} \left\{ \sum_{m=1}^{M} \left| \int_{-\infty}^{\infty} s^H(t-\tau) \hat{z}_{m,i}(t,0) e^{j\xi_{m,i}(\theta,\phi)} dt \right|^2 \right\} \tag{2.68}$$

As seen from the equations above, signal estimates for the multipaths with initialized parameters are subtracted from the observed data $\mathbf{x}(t)$. Parameter update procedure is continued until there is no considerable improvement in the sense of rMSE between consecutive iterations.

2.7 Multipath High Frequency (HF) Channel Modeling Using Swarm Intelligence

In this section, a blind source estimation technique called multipath separation-direction of arrival (MS-DOA) is combined with genetic algorithm to estimate DOAs for signals incoming from various ionospheric multipaths [36]. The signals at the output of the reference antenna can also be identified with high accuracy. In MS-DOA, both the array output vector and incoming signal vector are expanded in terms of a basis vector set. A linear equation is formed using the coefficients of the basis vector for the array output vector and the incoming signal vector and the array manifold. The DOAs in elevation and azimuth which maximize the sum of the magnitude squares of the projection of the signal coefficients on the range space of the array manifold are the required separation angles. Once the array manifold is estimated then the incoming signals can also be determined using the basis vectors and signal coefficients. When there are more than one mode impinging on the array or when the region of interest is not restricted, the search for the maximizer of the projections with brute force requires a time interval that inhibits the use of MS-DOA for online signal and angle estimation. Therefore, in this study, we utilize GA as an alternative search routine that can operate online for multiple direction of arrival estimation. In the following, we will briefly present MS-DOA technique with GA and provide some simulation results.

By omitting the delay and Doppler parameters, the model given in (2.28) can also be written as:

$$\mathbf{X} = \mathbf{B}\mathbf{A}^T \quad , \tag{2.69}$$

where

$$\boldsymbol{X} = [\mathbf{x}_1 \ldots \boldsymbol{x}_m \ldots \boldsymbol{x}_M] \quad , \tag{2.70}$$

$$\boldsymbol{B} = [\boldsymbol{b}_1 \ldots \boldsymbol{b}_i \ldots \boldsymbol{b}_d] \quad , \tag{2.71}$$

and $\boldsymbol{A}$ is the array manifold:

$$\boldsymbol{A} = [\boldsymbol{a}(\theta_1, \phi_1) \ldots \boldsymbol{a}(\theta_d, \phi_d)] \quad . \tag{2.72}$$

Since $\boldsymbol{x}_m$'s are linear combinations of $\boldsymbol{b}_i$'s, the rank of $\boldsymbol{X}$ can be at most d. This implies that d basis vectors are necessary and sufficient to represent the measurement vector. In determining the basis that spans the column space, singular value decomposition (SVD) can be used. The number of impinging waves on the receiving array can be estimated as the number of significant singular values in Σ of the following decomposition:

$$\boldsymbol{X} = \boldsymbol{U\Sigma V}^H \quad , \tag{2.73}$$

where the superscript H denotes the Hermitian operator throughout the text and

$$\mathbf{U} = [\mathbf{u}_1 \ldots \mathbf{u}_m \ldots \mathbf{u}_M] \quad , \tag{2.74}$$

and

$$\mathbf{V} = [\mathbf{v}_1 \ldots \mathbf{v}_m \ldots \mathbf{v}_M] \quad , \tag{2.75}$$

and $\mathbf{\Sigma}$ is the diagonal matrix containing singular values. An effective set of basis vectors can be chosen corresponding to the significant singular values as

$$\mathbf{U}_{\mathbf{eff}} = [\mathbf{u}_1 \ldots \mathbf{u}_i \ldots \mathbf{u}_d] \quad , \tag{2.76}$$

and

$$\mathbf{V}_{\mathbf{eff}} = [\mathbf{v}_1 \ldots \mathbf{v}_i \ldots \mathbf{v}_d] \quad . \tag{2.77}$$

Then $\mathbf{X}$ can be written as

$$\mathbf{X} = [\mathbf{u}_1 \ldots \mathbf{u}_i \ldots \mathbf{u}_d][\mathbf{X}_1 \ldots \mathbf{X}_i \ldots \mathbf{X}_d]^T \quad , \tag{2.78}$$

where

$$[\mathbf{X}_1 \ \ldots \ \mathbf{X}_i \ \ldots \ \mathbf{X}_d]^T = \underbrace{\begin{bmatrix} \sigma_1 & 0 & \cdots & 0 \\ 0 & \sigma_2 & \cdots & 0 \\ \vdots & \vdots & \ddots & \vdots \\ 0 & 0 & \cdots & \sigma_d \end{bmatrix}}_{\boldsymbol{\Sigma_{eff}}} \mathbf{V_{eff}}^H \ , \tag{2.79}$$

and Σ_{eff} denotes the singular value matrix which holds the d most significant singular values. By using above derivations the linear system of equations can be rewritten as:

$$\underbrace{\begin{bmatrix} \mathbf{A} & \mathbf{0} & \cdots & \mathbf{0} \\ \mathbf{0} & \mathbf{A} & \cdots & \mathbf{0} \\ \vdots & \vdots & \vdots & \vdots \\ \mathbf{0} & \mathbf{0} & \cdots & \mathbf{A} \end{bmatrix}}_{\mathbf{A_g}} \underbrace{\begin{bmatrix} \mathbf{B}_1 \\ \mathbf{B}_2 \\ \vdots \\ \mathbf{B}_d \end{bmatrix}}_{\mathbf{b_g}} = \underbrace{\begin{bmatrix} \mathbf{X}_1 \\ \mathbf{X}_2 \\ \vdots \\ \mathbf{X}_d \end{bmatrix}}_{\mathbf{x_g}} \tag{2.80}$$

For the optimum solution of the above set of equations, the following least squares cost function is defined as

$$J(\mathbf{a}_1; \ldots \mathbf{a}_d; \mathbf{b}_g) = ||\mathbf{A}_g \mathbf{b}_g - \mathbf{x}_g||^2 \tag{2.81}$$

where $||.||$ denotes the l_2 norm [92]. By using (2.80), this cost function can be rewritten as

$$J(\mathbf{a}_1; \ldots \mathbf{a}_d; \mathbf{b}_g) = \sum_{i=1}^{d} \ ||\mathbf{A}\mathbf{B}_i - \mathbf{X}_i||^2 \tag{2.82}$$

We investigate the values $\boldsymbol{a}_i$ and $\boldsymbol{b}_g$ which will minimize J. Because of the orthogonality property of the least squares cost function, the individual J_i's are minimized when the projection of $\mathbf{X}_i$'s onto the range space of $\mathbf{A}$ are maximized. The projections are defined as

$$\mathbf{P}_i(\mathbf{a}_i) = \mathbf{A}(\mathbf{A}^H\mathbf{A})^{-1}\mathbf{A}^H\mathbf{X}_i \tag{2.83}$$

where $1 \leq i \leq d$. Therefore, the optimal solution can be obtained as the maximizer of the following function $\mathcal{M}$:

$$\mathcal{M}(\mathbf{a}_1; \ldots; \mathbf{a}_d) = \sum_{i=1}^{d} ||\mathbf{P}_i||^2. \tag{2.84}$$

Once the DOAs are estimated as the maximizer of $\mathcal{M}$, then $\mathbf{B}_i$'s can be obtained as

$$\mathbf{B}_i = (\mathbf{A}^H(\tilde{\mathbf{a}}_1;\ldots;\tilde{\mathbf{a}}_d)\mathbf{A}(\tilde{\mathbf{a}}_1;\ldots;\tilde{\mathbf{a}}_d))^{-1}\mathbf{A}^H(\tilde{\mathbf{a}}_1;\ldots;\tilde{\mathbf{a}}_d)\mathbf{X}_i \quad . \tag{2.85}$$

By using $\mathbf{B}_i$'s, $\mathbf{B}$ can easily be obtained. Thus, with the MS-DOA algorithm, not only the DOAs of the incoming signals are estimated but also the incoming signals themselves at the output of the reference antennas are estimated. The search for the maximizers can be performed either by brute force (optimum solution but has higher computational time) or by a sub-optimum but fast nonlinear search algorithm such as genetic search as discussed in the next section.

2.7.1 Simulation Results on Real Ionospheric Data

In this section, we will provide the performances of plain MUSIC and MS-DOA with GA on real ionospheric data obtained from a high latitude path. The data set is provided by Dr. E.M. Warrington from University of Leicester, UK. The HF transmitter is located at Uppsala, Sweden and the receiver array is at Kiruna, Sweden. The receiver array is formed of 6 antennas, distributed inhomogeneously in a circular array. Out of this set of 6 antennas, only 5 antennas are calibrated and used in the DF problem. The transmitted signals are Barker-13 coded BPSK pulses modulated at 1667 baud with a repetition rate of 55 coded pulses per second. Signal duration is 2 s. The carrier frequency is changed every 30 s. The frequencies are repeated every 3 minutes. The details of the transmitted signal are provided in [93] and the receiver array is given [94]. Due to the structure of the HF link, only the signals at 4.63 MHz and 6.95 MHz proved to be useful in the analysis. The antenna output signals are normalized with respect to their $l2$ norm before they are introduced to the DF algorithms. The estimates of arrival angles for the test cases for 4.636001 MHz between 23:03:19 and 23:24:19 are provided in Table 2.2 on May 2, 2003. Here, the numbers denote the hour, the minute and the seconds, respectively. On May 2, 2003, at 2300 UT, sunspot number was

Table 2.2: The estimation of arrival angles for elevation and azimuth in degrees for 4.636001 MHz on May 02, 2003 between 23:03:19 to 23:24:19.

	MUSIC		MS-DOA with GA			
	Path1		Path1		Path2	
time	elevation	azimuth	elevation	azimuth	elevation	azimuth
23:03:19	25.7	194.8	29.5	196.5	35.9	195.7
23:06:19	20	117	28.9	194	34.7	193.6
23:09:19	25.1	195.6	27.9	196	33	194.7
23:12:19	32.9	196.3	26.3	196	32.4	195.6
23:15:19	42.9	197.4	26.5	196.8	34.8	195.2
23:18:19	27.5	195.3	27.5	196.1	33.6	195
23:21:19	30.2	194.8	28.7	195	34.7	194.8
23:24:19	29.3	195.7	28.8	194.8	33.5	194.7
mean	29.2	185.9	28	195.7	34.1	194.9
median	28.4	195.5	28.3	196	34.2	194.9

86, Kp index was 2+, Ap index was 9 and Dst index was -17. The approximate distance between the Uppsala and Kiruna is 886 km and Uppsala is 193^0 from the local north of Kiruna in the azimuth. The elevation of multipath components for both frequencies are expected to be between 20^0 and 40^0 according to the results in [93].

The estimates of arrival angles for the test cases for 6.953 MHz between 23:00:49 and 23:24:49 are provided in Table 2.3. Here, the numbers denote the hour, the minute and the seconds, respectively.

As it might be readily observed from Table 2.2 and Table 2.3, for both frequencies, Plain MUSIC is able to detect only one path, yet for MS-DOA with GA, two paths are estimated. The estimate of the MUSIC in one path corresponds to the first path estimated with MS-DOA. The mean and median of the angles during the estimation interval are also provided in the tables. With MS-DOA estimates, both the mean and the median are close to each other for all paths indicating a consistency and robustness in the estimates. When the two paths estimates are compared, it is also observed that the two paths are very close to each other in azimuth and they are separated with couple of degrees in elevation. The mean estimates for the arrival angles are in very well accordance with the

Table 2.3: The estimation of arrival angles for elevation and azimuth in degrees for 6.953 MHz on May 02, 2003 between 23:00:49 to 23:24:49.

	MUSIC		MS-DOA with GA			
	Path1		Path1		Path2	
time	elevation	azimuth	elevation	azimuth	elevation	azimuth
23:00:49	30.8	196	33.4	193.1	36.5	194.8
23:03:49	31.7	196.5	33	193.2	37.1	194.3
23:06:49	31.9	195.7	33.4	194	37.2	195.6
23:09:49	32.6	195.3	33.7	194.2	37.8	195.7
23:12:49	33	195.2	33.3	193.5	37.4	195.3
23:15:49	33.3	197.4	32.6	194.6	36.5	196
23:18:49	32.4	196.1	33.4	194.3	37.9	196.2
23:21:49	32.3	196.3	32.9	194.4	36.7	196.1
23:24:49	32.8	195.8	32.3	194.2	36.3	195.6
mean	32.3	196	33.1	193.9	37	195.5
median	32.4	196	33.3	194.2	37.1	195.6

expected azimuth and elevation angles. The angle spread is larger in MUSIC than MS-DOA with GA for both frequencies. The estimates are also provided in Fig. 2.14 for easier viewing. In Figure (2.14a) and (2.14b), the estimates for the arrival angle in elevation and azimuth, respectively, are provided for the first path and for the two frequencies. The first path is estimated by both MUSIC and MS-DOA with GA. In Figure (2.14c) and (2.14d), the elevation and azimuth estimates for the two frequencies are given for path 2. The second path is only estimated by MS-DOA with GA. From the analysis of both simulated and experimental data, it can be observed that MS-DOA with GA provides a powerful alternative in direction of arrival and multipath separation problems in HF links.

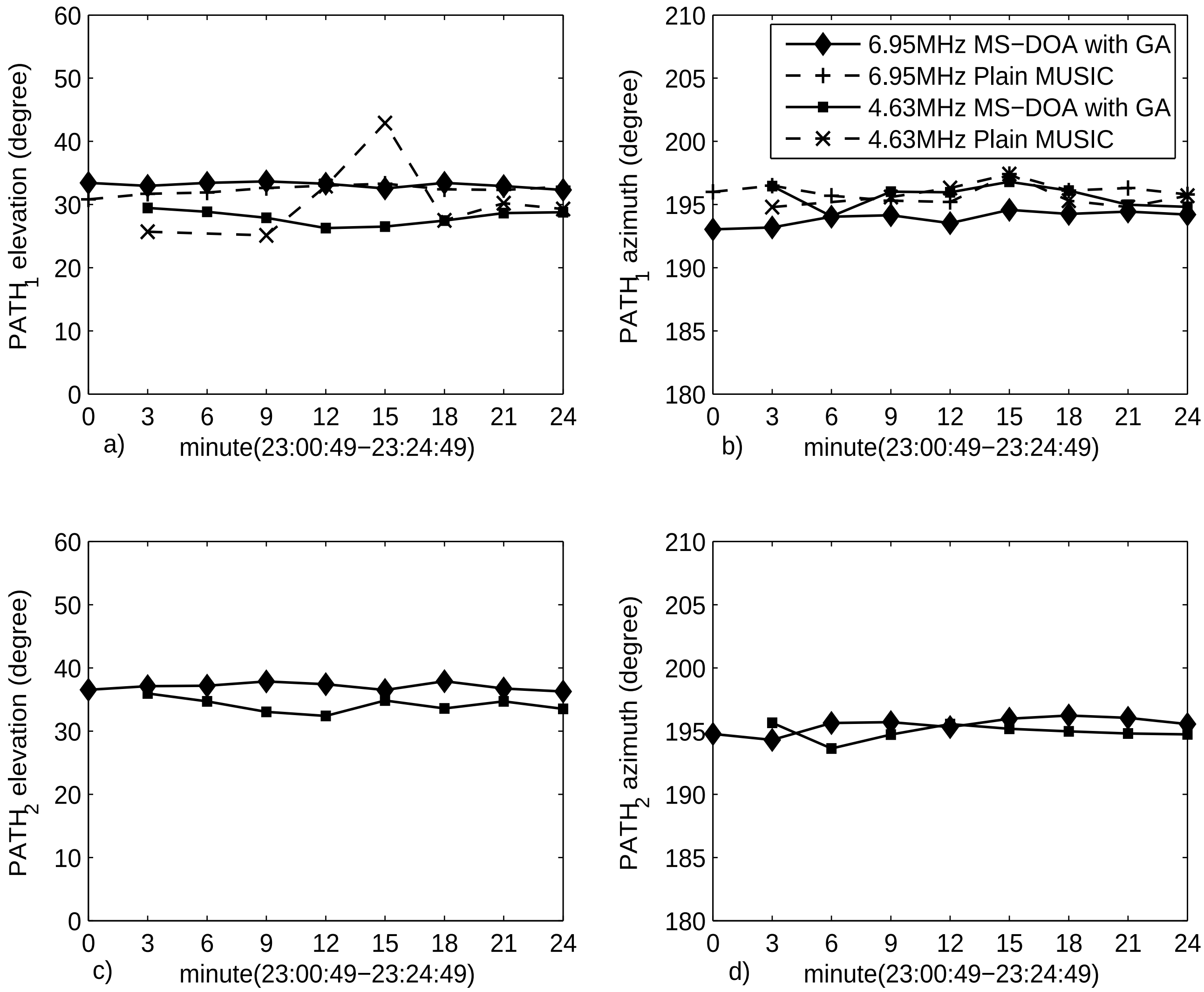

Figure 2.14: Estimation of arrival angles for MS-DOA with GA and MUSIC for two frequencies for path-1 a-) elevation b-) azimuth; for path-2 c-) elevation d-) azimuth.

Chapter 3

Multipath Channel Identification in Ambiguity Function Domain

3.1 Introduction

The new generation radio communication systems are faced with the ever increasing demand for higher communication rates. In order to meet this demand, the communication systems should obtain an accurate model for the communication channel [95]. For fuller utilization of multipath communication channels, communication systems utilize antenna arrays and sophisticated signal processing techniques to produce estimates for multipath channel parameters including direction of arrivals (DOA), time-delays, Doppler shifts and amplitudes.

In wideband communication channels with peak power limitations, typically coded waveforms with the time-bandwidth products significantly larger than 1 are employed. In these systems pulse compression of the receiver is a necessity to provide optimal extraction of the transmitted information. In delay only channels with bandlimited white noise, pulse compression can be achieved by a simple matched filter that implements correlation of the incoming signal with the transmitted waveform. However, in the presence of Doppler shifts a single matched filter cannot provide the optimal performance, rather a bank of matched filters each matched to a specific Doppler shift should be employed [23], providing individual Doppler slices of the CAF between the transmitted and received signals. Therefore, it is of both theoretical and practical interest to develop array signal processing techniques where CAF is an integrated component of the processing chain.

In this chapter, we present a new array signal processing technique to estimate the DOAs, time delays, Doppler shifts and amplitudes of a known waveform impinging onto an array of antennas from several distinct paths. The proposed technique detects the presence of multipath components by integrating CAF of array outputs, hence, it is called as the cross-ambiguity function direction finding (CAF-DF). The performance of the CAF-DF technique is compared with those of space-alternating generalized expectation-maximization (SAGE) and multiple signal classification (MUSIC) techniques as well as the Cramèr-Rao lower bound. The CAF-DF technique is found to be superior in terms of root-mean-squared-error (rMSE) to the SAGE and MUSIC techniques. Moreover, the performance of the CAF-DF technique is tested on recorded real ionospheric data and is found to be very effective in resolving multipaths [24], [25], [26], [27], [28], [29].

The outline of this chapter is as follows. Firstly, details and analysis of the CAF-DF algorithm is presented in section 3.2. The simulation results concerning the performances of the algorithms on synthetic signals are presented in section 3.3. Lastly, in section 3.4 performance of the proposed algorithm is tested on real ionospheric data.

3.2 Channel Modelling in Ambiguity Function Domain

The cross-ambiguity function domain direction finding (CAF-DF) is an iterative technique where at each iteration parameters of a single path are estimated. In the rest of this section, we present the steps of the technique in detail. The received signals are often modeled as delayed, Doppler-shifted and scaled versions of the transmitted signal. As it used in radar signal processing, the CAF can be used in order to estimate the time delay of a Doppler shifted signal for the received signal $x_m(t)$ and the transmitted signal $s(t)$ [23], [96]. Symmetrical version of the CAF is:

$$\chi_{x_m,s}(\tau,\nu) = \int_{-\infty}^{\infty} x_m\left(t+\frac{\tau}{2}\right)\, s^*\left(t-\frac{\tau}{2}\right)\, e^{-j2\pi\nu t}\, dt \quad . \tag{3.1}$$

Details and properties of AF is provided in appendix-B. Starting point of the CAF-DF technique is to estimate the DOA information which is captured in $e^{-j2\pi\nu_c\xi_{m,i}(\theta_i,\phi_i)}$. For this purpose, for each antenna output, its corresponding CAF with the transmitted waveform is computed. Since the antennas in the array are closely spaced, peak locations of the CAFs will be nearly the same for each antenna. When the phase of each impinging signal on the array is unknown, to detect the delay and Doppler coordinates of the path (highest peak point on the CAF surface), absolute values of CAFs at the output of each antenna is calculated and incoherently integrated as:

$$\chi_{total}(\tau,\nu) = \left|\chi_{x_1,s}(\tau,\nu)\right| + \ldots + \left|\chi_{x_M,s}(\tau,\nu)\right| \quad . \tag{3.2}$$

As a result of the incoherent integration, the SNR prior to the peak detection phase is increased with improved detection of the delay and Doppler coordinates $(\hat{\tau}_i, \hat{\nu}_i)$ of the highest peak that exceeds the detection threshold. Note that the resolution of delay and Doppler in the CAF domain are $\Delta\tau = 1/\mathrm{BW}$ and $\Delta\nu = 1/T$, respectively [23]. Here, BW corresponds to the bandwidth and T

is the duration of $s(t)$. Well known in radar literature [23], in the presence of single path, the incoherent integration provides considerable improvement. The incoherent integration based peak detection procedure is illustrated in Figs. 3.1, 3.2, 3.3 by using a fifteen-element circular antenna array output. Fig. 3.1(a)-(d) are the sample CAF surfaces calculated for four antennas and Fig. 3.2(a), Fig. 3.3(a) are the incoherent integration of fifteen CAF surfaces for path-1 and path-2, respectively. It is seen from the resultant normalized CAF that the noise level is suppressed relative to the peak when compared to the individual CAFs, and paths can be localized. Once the largest peak exceeding the detection threshold is identified, the following vector $\mathbf{P_i}$ is formed from the individual CAF values at the detected peak location $(\hat{\tau}_i, \hat{\nu}_i)$:

$$\mathbf{P_i} = \left[\chi_{x_1,s}(\hat{\tau}_i, \hat{\nu}_i), \ldots, \chi_{x_M,s}(\hat{\tau}_i, \hat{\nu}_i)\right]^T \quad . \tag{3.3}$$

The DOA of the detected path can be estimated from the phases of the elements of $\mathbf{P_i}$. For this purpose the following criterion can be used:

$$(\hat{\theta}_i, \hat{\phi}_i) = \arg\max_{\theta_i,\phi_i} \frac{|\mathbf{P_i}^H \mathbf{W}(\theta_i, \phi_i)|}{\|\mathbf{P_i}\|} \quad , \tag{3.4}$$

where $\mathbf{W}$ is defined as:

$$\mathbf{W}(\theta_i, \phi_i) = \frac{1}{\sqrt{M}} \left[e^{j\xi_{1,i}(\theta_i,\phi_i)}, \ldots, e^{j\xi_{M,i}(\theta_i,\phi_i)}\right]^T , \tag{3.5}$$

which is the vector whose elements are the phases across the receiver antennas due to a hypothesized path impinging onto the array from (θ_i, ϕ_i) direction. Note that, if there were a single path in the detected delay-Doppler cell, this criterion would have provided highly accurate estimates. Obtained $(\hat{\theta}_i, \hat{\phi}_i)$ pair is then used in the coherent integration process, that will further improve the accuracy of the obtained delay and Doppler estimates. For the sake of simplicity output of the m^{th} antenna can be written as:

$$x_m(t) = \sum_{i=1}^{d} \check{s}_i(t) e^{-j2\pi\nu_c \xi_{m,i}(\theta_i,\phi_i)} + n_m(t) \quad . \tag{3.6}$$

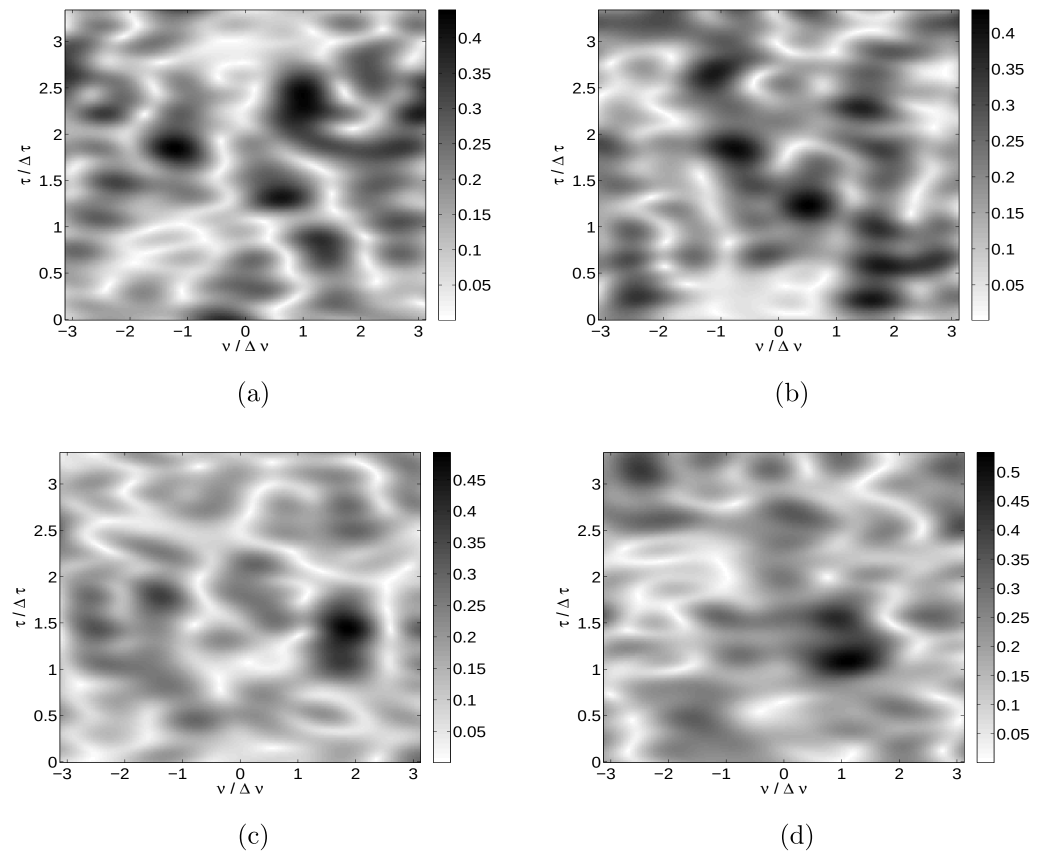

Figure 3.1: Calculated CAF surfaces of two signal paths with parameters $\tau/\boldsymbol{\Delta}\tau$=[1.5,1.5] and $\nu/\boldsymbol{\Delta}\nu$=[1.9,0.7]. (a,b,c,d): CAF surfaces of 4 antennas, which are selected arbitrarily from 15-element antenna array.

The estimated $\hat{\theta}_i$ and $\hat{\phi}_i$ enables coherent combination of individual antenna outputs to obtain $x_{coh}(t)$ as:

$$x_{coh}(t) \;=\; \sum_{m=1}^{M} x_m(t) e^{j2\pi\nu_c \xi_{m,i}(\hat{\theta}_i,\hat{\phi}_i)} \quad , \tag{3.7}$$

which can be decomposed into three terms as:

$$\begin{aligned} x_{coh}(t) \;&=\; M\check{s}_i(t) \\ &+\; \sum_{m=1}^{M}\sum_{i'\neq i}^{d} \check{s}_{i'}(t) e^{-j2\pi\nu_c(\xi_{m,i'}(\theta_{i'},\phi_{i'})-\xi_{m,i}(\hat{\theta}_i,\hat{\phi}_i))} \\ &+\; \sum_{m=1}^{M} n_m(t) e^{j2\pi\nu_c \xi_{m,i}(\hat{\theta}_i,\hat{\phi}_i)} \quad . \end{aligned} \tag{3.8}$$

Here, the first term is the sum of phase corrected versions of the i^{th} signal path at each antenna, the second term includes the other signal paths in the environment,

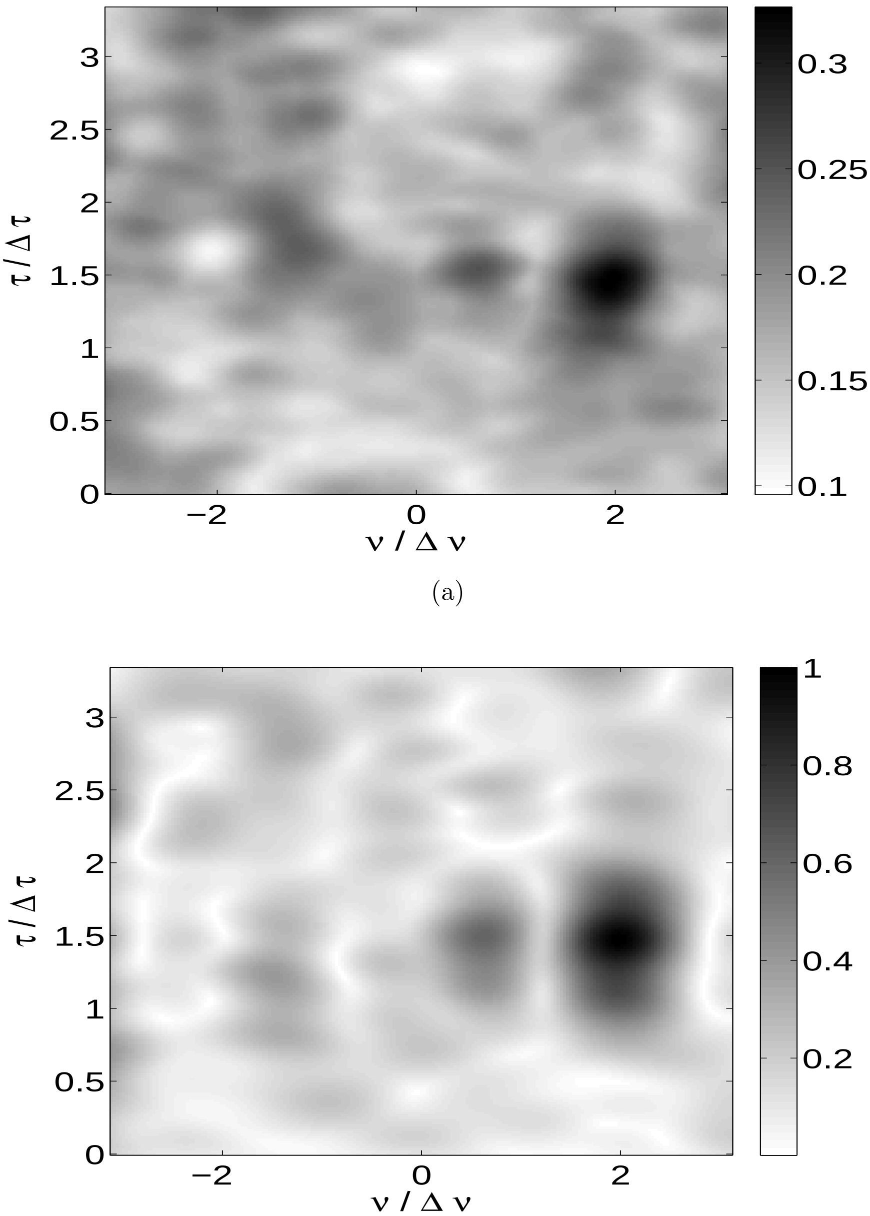

(a)

(b)

Figure 3.2: Calculated CAF surfaces of two signal paths with parameters $\tau/\mathbf{\Delta}\tau$=[1.5,1.5] and $\nu/\mathbf{\Delta}\nu$=[1.9,0.7]. (a): Incoherently integrated CAF surface of path-1. (b): Coherently integrated CAF surface of path-1.

and the third term is noise. SNR defined at a single antenna is

$$SNR_m = \frac{E[|\check{s}(t)|^2]}{E[|n_m(t)|^2]} = \frac{\mathbf{E}_{\check{s}}}{\sigma^2} \quad . \tag{3.9}$$

Therefore, when multipath components are separated from each other by a few delay-Doppler resolution cells, the coherent integration, as given in (3.8), of

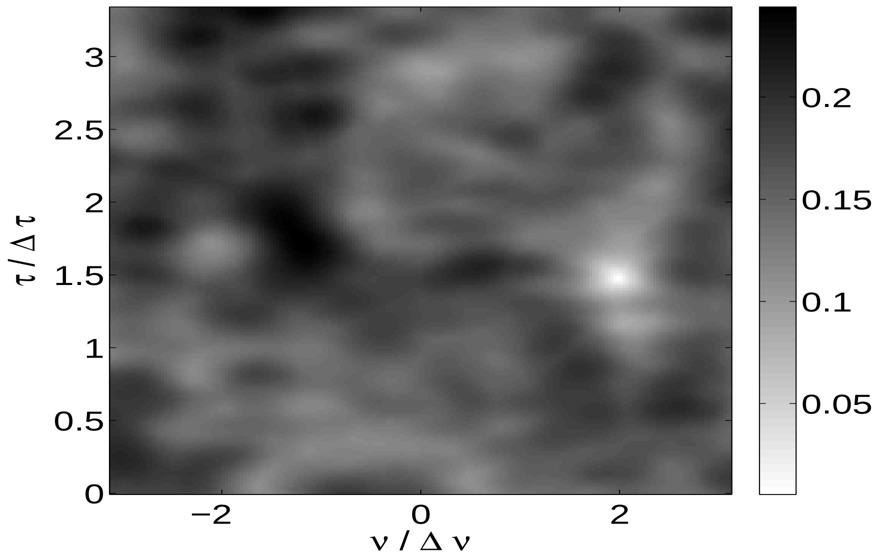

(a)

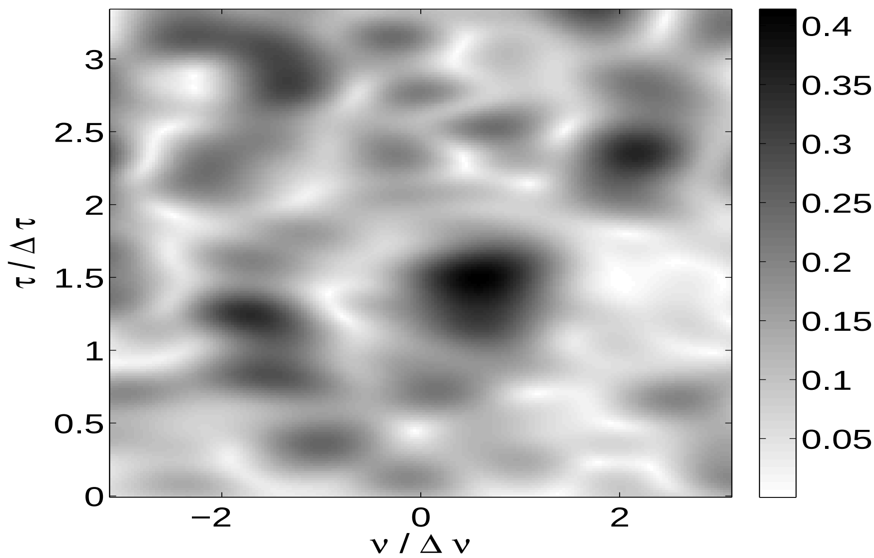

(b)

Figure 3.3: Calculated CAF surfaces of two signal paths with parameters $\tau/\mathbf{\Delta}\tau$=[1.5,1.5] and $\nu/\mathbf{\Delta}\nu$=[1.9,0.7]. (a): Incoherently integrated CAF surface of path-2. (b): Coherently integrated CAF surface of path-2.

the antenna outputs results in an improvement in the SNR by a factor almost equal to the number of array elements. The phase correction procedure, with respect to the array origin, given in (3.7) is illustrated as in Fig. 3.4, where the slow-time versions (sampled version of the pulse train with pulse repetition interval) of the antenna outputs are seen. If phase shifting with respect to the array

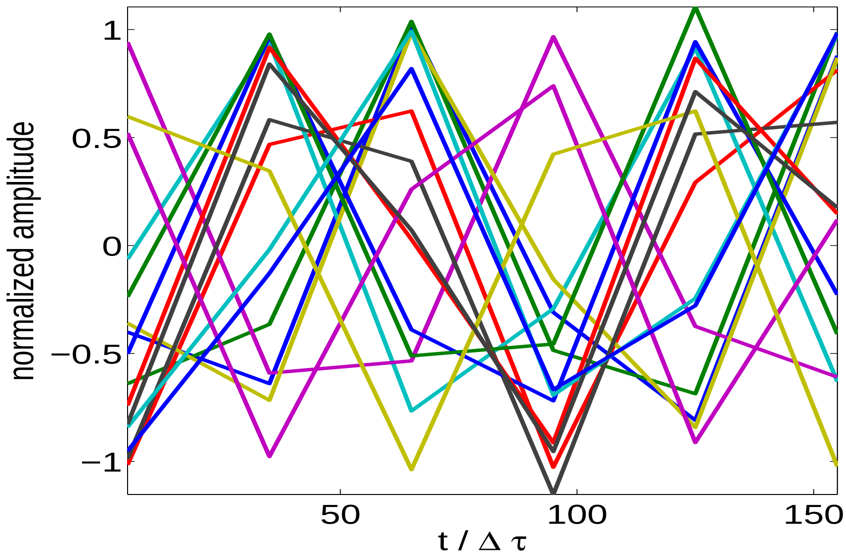

(a)

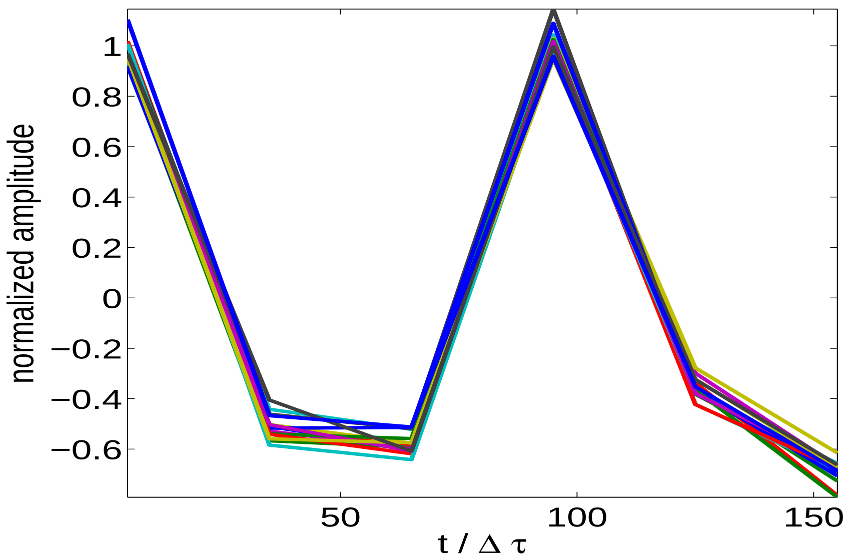

(b)

Figure 3.4: Coherent integration process in slow-time for 15-element antenna array. Real part of the complex array output is plotted. (a): Slow-time output of array before coherent integration. (b): Slow-time output of array after coherent integration.

origin occurs with the correct DOA estimates, than output slow-time signals overlap as in the Fig. 3.4.

As demonstrated in Fig. 3.2(b) and 3.3(b), the CAF between the transmitted signal and the signal obtained by coherent integration, $x_{coh}(t)$, yields more

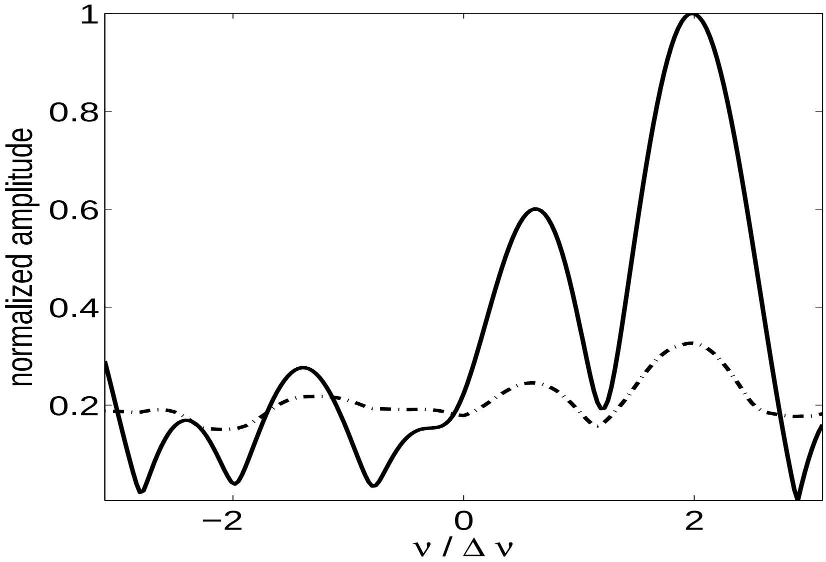

(a)

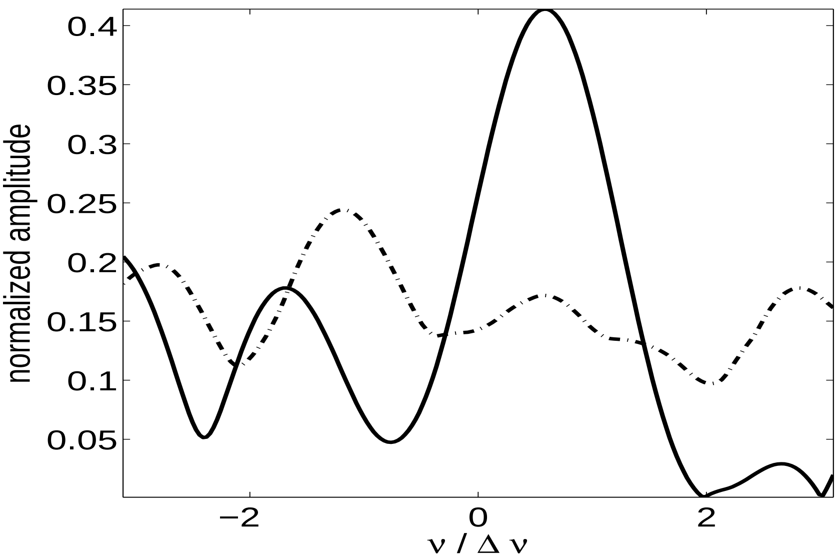

(b)

Figure 3.5: Two signal paths with parameters $\tau/\boldsymbol{\Delta}\tau$=[1.5,1.5] and $\nu/\boldsymbol{\Delta}\nu$=[1.9,0.7]. 1-D peak-delay slices of CAF surfaces of Fig. 3.2 - 3.3. Bold and dashed lines are for coherent and incoherent integration, respectively. (a): 1-D peak-delay slice of CAF surface of path-1. (b): 1-D peak-delay slice of CAF surface of path-2.

accurate detection of delay and Doppler of the detected path. In order to visualize the effect of the coherent integration clearly, a 1-D delay slice of the peak point on the incoherently integrated CAF and coherently integrated CAF surfaces, shown in Fig. 3.2 - 3.3, are presented in Fig. 3.5. Bold line represents the

1-D slice across the coherently integrated surface and the dashed line represents the 1-D slice across the incoherently integrated surface. Note that, interference from other signal paths and the noise is less detrimental around the peak of the coherently integrated CAF. Therefore, the delay-Doppler estimates for the detected path become more accurate. Also note that, in Fig. 3.5(b), peak location of the incoherently integrated CAF, which is the Doppler estimate of the path-2, is shifted left from its true value. However, peak location of the coherently integrated CAF points the true Doppler value clearly. The obtained estimates for azimuth, elevation, delay and Doppler parameters of one of the impinging paths enables to generate a copy of the impinging signal at each antenna output as:

$$\hat{x}_{m,i}(t) = \zeta_{m,i} s(t - \hat{\tau}_i) e^{j2\pi\hat{\nu}_i t} e^{-j2\pi\nu_c \xi_{m,i}(\hat{\theta}_i, \hat{\phi}_i)} \quad , \tag{3.10}$$

where i represents the i^{th} detected signal path and $\zeta_{m,i}$ is a complex scalar, which covers all the phase shifts and attenuation effects and modeled as an uniformly distributed phase between 0 and 2π. Due to, calibration inaccuracies of the antenna array, $\zeta_{m,i}$ may differ for each antenna. Under additive white Gaussian noise model, conditional maximum likelihood estimate of the $\zeta_{m,i}$ for a given set of estimated $(\hat{\tau}_i, \hat{\nu}_i, \hat{\theta}_i, \hat{\phi}_i)$ parameters can be obtained as the minimizer of the following cost function:

$$J_m(\zeta_{m,i}) = \int_0^{T_{coh}} \left| x_m(t) - \hat{x}_{m,i}(t) \right|^2 dt \quad . \tag{3.11}$$

The minimizer $\zeta_{m,i}$ of this quadratic cost function can be found by using the orthogonality property yielding:

$$\hat{\zeta}_{m,i} = \frac{\displaystyle\int_0^{T_{coh}} s^*(t - \hat{\tau}_i) e^{-j2\pi\hat{\nu}_i t} e^{j2\pi\nu_c \xi_{m,i}(\hat{\theta}_i, \hat{\phi}_i)} x_m(t) dt}{\displaystyle\int_0^{T_{coh}} s^*(t - \hat{\tau}_i) s(t - \hat{\tau}_i) dt} \quad . \tag{3.12}$$

Note that, if there is negligible calibration issue between the antennas, $\zeta_{m,i}$ will be approximately the same for each antenna and can be estimated optimally as:

$$\hat{\zeta}_i = \frac{1}{M} \sum_{m=1}^{M} \hat{\zeta}_{m,i} \quad . \tag{3.13}$$

Once the complex scaling parameter, $\hat{\zeta}_{m,i}$ is obtained, the identified path is fully characterized. Hence, a copy of the first signal path at each antenna output can be generated to eliminate it from the array outputs to recurse on the residual for detection of the remaining paths. Although it is in the class of suboptimal greedy optimization techniques, this iterative approach is highly efficient. Note that, the elimination of a path from the array outputs eliminates both its main and sidelobes from the CAF domain. Thus, weaker paths that are buried under the sidelobes of the detected and eliminated path might become detectable as well. An illustration of this fact is shown in Figs. 3.2, 3.3, where the CAF of the residual array outputs reveals the presence of a weaker path that was partially buried under the sidelobes of the eliminated path. This detection and elimination process is repeated until there is no peak exceeding the detection threshold that can be set to satisfy a constant false alarm rate. In Table 3.1, steps of the CAF-DF algorithm is summarized.

Table 3.1: CAF-DF algorithm

while there exist peaks exceeding detection threshold
for $i=1$; $i \le d$; $i++$
- CAF computation at each antenna output with transmitted known signal using (3.1).
- Incoherent integration of M CAFs using (3.2).
- Detect the peak point coordinates $(\hat{\tau}_i, \hat{\nu}_i)$ of the incoherently integrated CAFs.
- Collect M complex values on each CAF surface corresponding to the coordinates $(\hat{\tau}_i, \hat{\nu}_i)$ and create a M dimensional vector by (3.3).
- Using (3.4) and (3.5) estimate DOAs $(\hat{\theta}_i, \hat{\phi}_i)$.
- Correct the phases of each antenna output with respect to the array origin with $(\hat{\theta}_i, \hat{\phi}_i)$ and add them up by (3.7).
- Estimate $\hat{\tau}_i$ and $\hat{\nu}_i$ using (3.1).
- Estimate complex scalar using either (3.12) or (3.13).
- Create a copy of the i^{th} signal path with estimated parameters.
- Subtract the copy signal from each antenna output.
end
end

3.3 Simulation Results on Synthetic Signals

In this section, performances of the CAF-DF, SAGE and MUSIC algorithms are compared on synthetic signals at different SNR values by using Monte Carlo simulations. The SAGE algorithm [15] is a well known technique with recognized practical success. In chapter-2.6, details of the SAGE algorithm is presented [19]. The MUSIC-based algorithm is a classical technique, and widely used in many applications [6], [97]. The joint rMSE, the basis of our comparisons, is defined as:

$$\text{rMSE} = \sqrt{\frac{1}{dN_r}\sum_{\mu=1}^{N_r}\sum_{i=1}^{d}[\hat{\boldsymbol{\varphi}}_i^{\mu} - \boldsymbol{\varphi}_i^{\mu}]^2} \quad , \tag{3.14}$$

where N_r is the number of Monte-Carlo simulations, $\hat{\boldsymbol{\varphi}}_i^{\mu}$ is the parameter estimates of the i^{th} signal path found in the μ^{th} simulation and $\boldsymbol{\varphi}_i^{\mu}$ is the true parameter values of the i^{th} path in the μ^{th} simulation. A circular receiver array of M omnidirectional sensors at positions $[r\text{cos}(m2\pi/M), r\text{sin}(m2\pi/M)]$, $1 \leq \ldots \leq M$, is synthesized. The radius of the array $r = \lambda/4\text{sin}(\pi/M)$ is chosen such that the distance between two neighboring sensors is $\lambda/2$, where λ is the carrier wavelength. The transmitted training signal consists of 6 Barker-13 coded pulses with a duration of $13\Delta\tau$ where $\Delta\tau$ is the chip duration. The pulse repetition interval is $30\Delta\tau$ resulting a total signal duration of $qT = 167\Delta\tau$. The SNR is defined at a single sensor relative to the noise variance. Both the CAF-DF and the SAGE algorithms are iterated only 4 times, which is found to be sufficient for convergence.

In the first experiment there exist two equal power paths having parameters $\boldsymbol{\varphi}_1 = [50^o, 40^o, 2\Delta\tau, 1.7\Delta\nu, e^{j\psi_1}]$ and $\boldsymbol{\varphi}_2 = [54^o, 44^o, 1.5\Delta\tau, 0.8\Delta\nu, e^{j\psi_2}]$, where ψ_1 and ψ_2 are uniformly distributed between $[0, 2\pi]$. A uniform circular array of $M = 15$ sensors is used. Note that, the two paths are closely spaced in all parameters. Time-delay and Doppler shift difference between the two paths are $0.5\Delta\tau$ and $0.9\Delta\nu$ respectively in CAF domain.

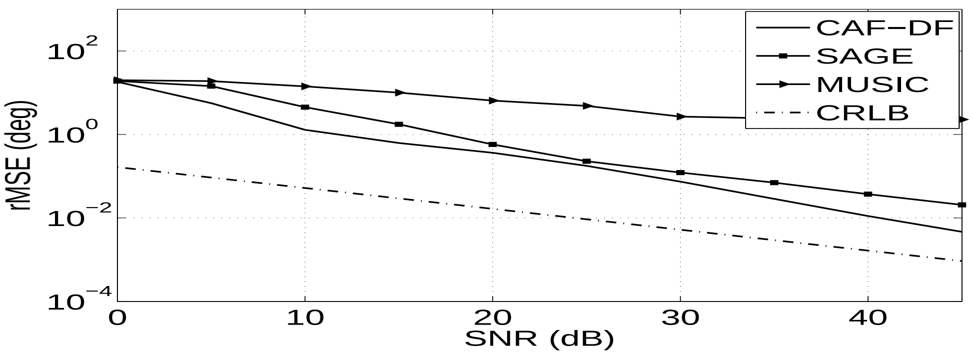

(a)

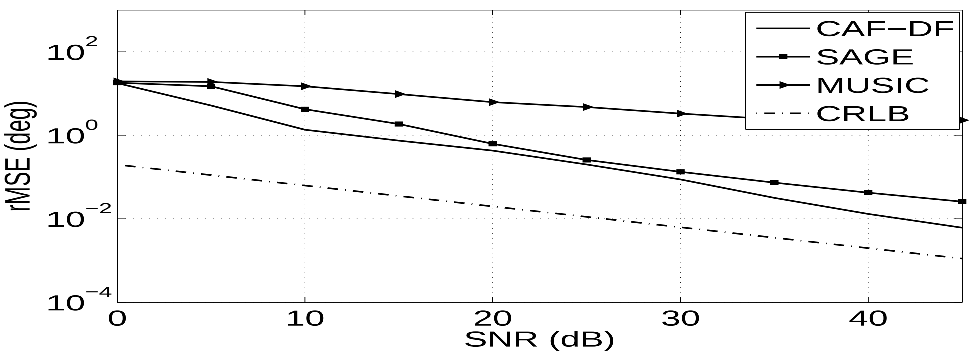

(b)

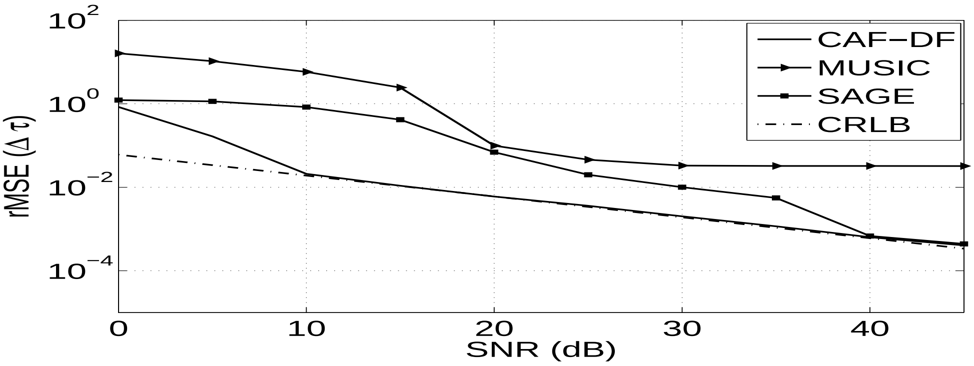

(c)

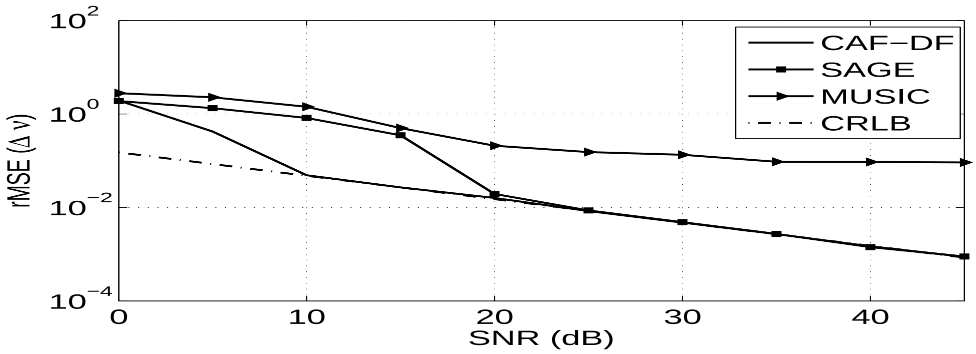

(d)

Figure 3.6: Joint-rMSE obtained with the CAF-DF, the SAGE and the MUSIC for two signal paths with $\boldsymbol{\varphi}_1 = [50^o, 40^o, 2\Delta\tau, 1.7\Delta\nu, e^{j\psi_1}]$ and $\boldsymbol{\varphi}_2 = [54^o, 44^o, 1.5\Delta\tau, 0.8\Delta\nu, e^{j\psi_2}]$ at different SNR values. (a): azimuth, (b): elevation, (c): time-delay and (d): Doppler shift.

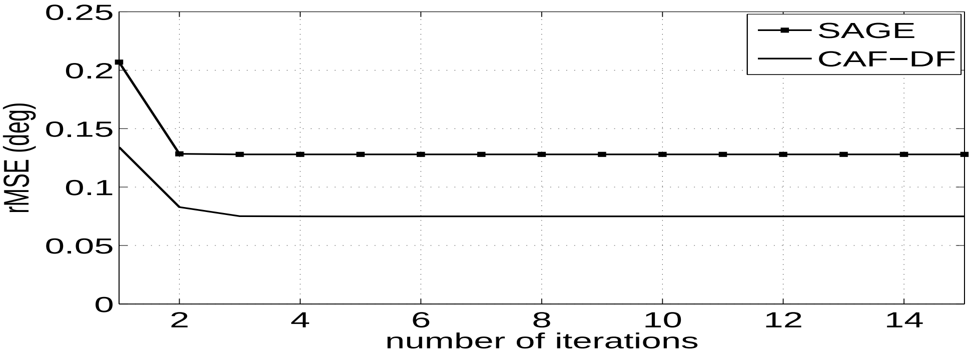

(a)

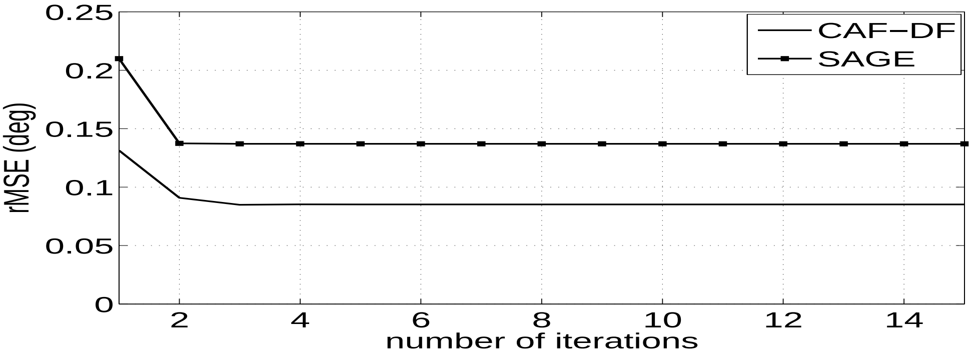

(b)

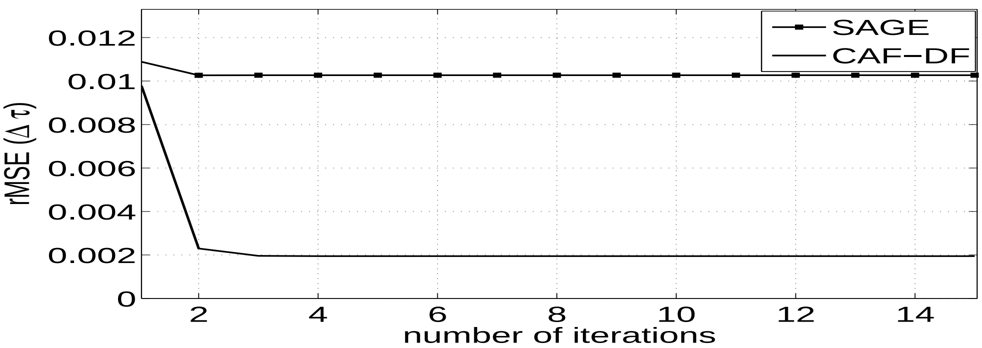

(c)

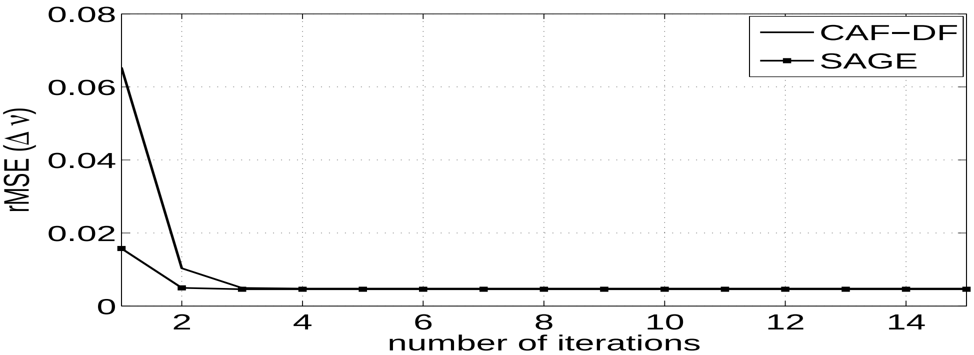

(d)

Figure 3.7: Joint-rMSE obtained with the CAF-DF and the SAGE for two signal paths with $\boldsymbol{\varphi}_1 = [50^o, 40^o, 2\Delta\tau, 1.7\Delta\nu, e^{j\psi_1}]$ and $\boldsymbol{\varphi}_2 = [54^o, 44^o, 1.5\Delta\tau, 0.8\Delta\nu, e^{j\psi_2}]$ for different number of iterations. (a): azimuth, (b): elevation, (c): time-delay and (d): Doppler shift.

Two paths are 4^o separated in spatial domain. Fig. 3.6 presents the rMSE obtained from 500 Monte Carlo runs at each SNR. Time-delay and Doppler rMSEs are normalized by $\Delta\tau$ and $\Delta\nu$, respectively. Obtained results show that both the CAF-DF and the SAGE techniques provide significantly better parameter estimates than the MUSIC technique. Furthermore, the CAF-DF technique outperforms the SAGE technique and provides more reliable estimates at all simulated SNR values. Since in many applications low SNR performance is a deciding factor, the superior performance of the CAF-DF at low SNRs is a significant improvement. Using the same settings of the first experiment, Fig. 3.7 illustrates the convergence of rMSE for the CAF-DF and the SAGE techniques at 30 dB SNR. As expected, the rMSE of each parameter has a monotonic decrease with iterations. Both algorithms converges in a few iterations.

In the second simulation study, there exist two equal power paths with parameters $\boldsymbol{\varphi}_1 = [50^o, 40^o, 1.5\Delta\tau, 1.6\Delta\nu, e^{j\psi_1}]$ and $\boldsymbol{\varphi}_2 = [54^o, 44^o, 1.66\Delta\tau, 0.8\Delta\nu, e^{j\psi_2}]$. A uniform circular array with $M = 15$ sensors is used. This time the paths are even more closer. Time-delay and Doppler shift difference between the two paths are $0.16\Delta\tau$ and $0.8\Delta\nu$, respectively. Paths can now be separated only by using the difference in their Doppler shift. The obtained results are tabulated in Table 3.2. As in the first experiment, MUSIC is not able to separate the paths. Performances of the CAF-DF and the SAGE are degraded slighltly, as expected. In this scenario, except the Doppler estimates at high SNRs, the CAF-DF consistently performs better than the SAGE.

In the third experiment, we investigated the identification of 10 paths with a circular array of 8 sensors. The path parameters are given in the Table 3.3. The delay-Doppler domain spread of these paths are shown in Fig. 3.8. Note that the number of paths exceeds the number of sensors which would made it impossible to resolve with narrowband systems. However, in wideband communication systems, delay-Doppler domain diversity of the paths can be exploited to resolve

Table 3.2: rMSE values of MUSIC(A1), SAGE(A2) and CAF-DF(A3) algorithms for various SNR values. CRLB(A4). Time-delay and Doppler rMSEs are normalized by $\Delta\tau$ and $\Delta\nu$, respectively.

SNR(dB)		rMSE(deg)	rMSE(deg)	rMSE / $\Delta\tau$	rMSE / $\Delta\nu$
10	A1	15.58	15.79	11.84	1.56
	A2	4.23	3.7	0.9	1.1
	A3	1.73	2.45	0.07	0.46
	A4	0.02	0.027	0.019	0.046
15	A1	14.48	14.24	11.62	1.42
	A2	2.07	1.91	0.44	0.76
	A3	0.83	0.84	0.01	0.051
	A4	0.011	0.016	0.01	0.025
20	A1	12.32	14.06	11.48	1.3
	A2	0.61	0.66	0.077	0.035
	A3	0.41	0.49	0.0068	0.025
	A4	0.006	0.0092	0.0061	0.014
25	A1	11.75	12.68	10.2	1.04
	A2	0.22	0.25	0.019	0.013
	A3	0.22	0.27	0.0037	0.016
	A4	0.0036	0.0052	0.0034	0.008
30	A1	10.6	10.18	8.2	0.63
	A2	0.12	0.12	0.011	0.006
	A3	0.08	0.11	0.0024	0.012
	A4	0.002	0.0026	0.0019	0.004

the paths as long as there are fewer paths than the number of array elements in each resolvable delay-Doppler cell. The joint rMSE in the estimated path parameters by the proposed CAF-DF and the SAGE algorithms are shown in Fig. 3.9. We observed that the CAF-DF technique provided significantly better estimates at all SNR levels. The main reason for failure of the SAGE is that, when the number of paths increases, the maximum likelihood based approach faces significant challenges in finding the global maximum of the likelihood function. This is mainly because of the fact that likelihood maximization is performed in time domain, where there is a considerable overlap between the signals received from different paths. However, CAF-DF technique transforms the array signal outputs to the CAF domain where different multipath signals are localized to their

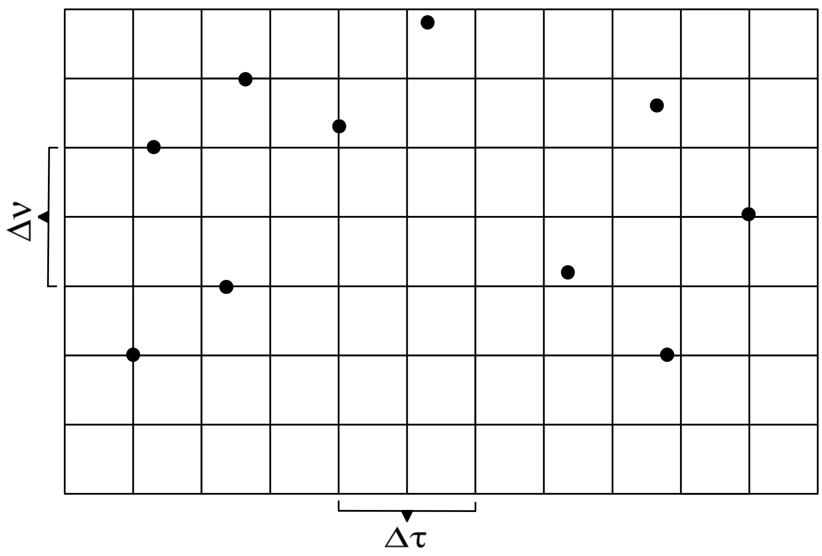

Figure 3.8: Delay-Doppler spread of the 10 signal paths are represented with black dots on the delay-Doppler domain.

respective delay and Doppler cell. Therefore, overlapping signals in time domain are separated in delay Doppler domain resulting in the observed performance improvement. Moreover, in Fig. 3.10, $\widehat{SNR}_{CAF-DF}/\widehat{SNR}_{SAGE}$ ratio is plotted for threshold and asymptotic regions of estimation performance at various SNR values using equations (2.33) and (2.34). Parallel with the results shown in Fig. 3.6, at all SNR levels CAF-DF combines diversity better than the SAGE which enable detector to accurately retrieve the transmitted information.

Table 3.3: 10 path parameters. Time-delay, Doppler and complex scaling factor values are normalized by $\Delta\tau$, $\Delta\nu$ and $e^{j\psi_i}$, respectively. ψ_i's, $i = 1, ..., d$, are uniformly distributed between $[0, 2\pi]$.

path	θ(deg)	ϕ(deg)	$\tau/\Delta\tau$	$\nu/\Delta\nu$	$\zeta/e^{j\psi_i}$
1	45	30	1	1	1
2	50	35	1.66	1.5	0.9
3	55	40	1.16	2.5	0.8
4	60	45	1.83	3	0.7
5	65	50	2.5	2.7	0.6
6	70	55	3.16	3.4	0.8
7	75	38	4.16	1.6	0.8
8	57	47	4.83	1	1
9	63	43	4.66	2.8	1
10	68	33	5.5	2.1	0.7

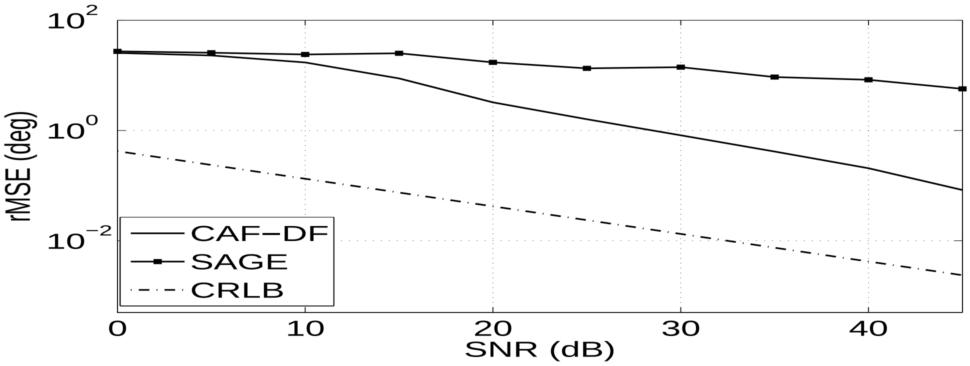

(a)

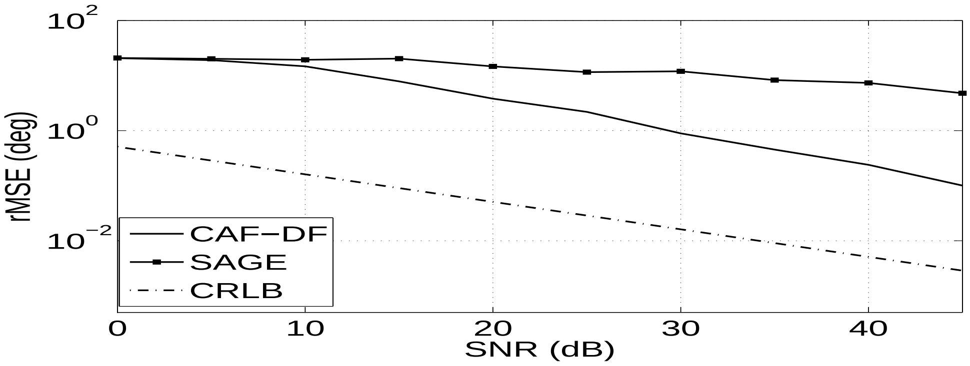

(b)

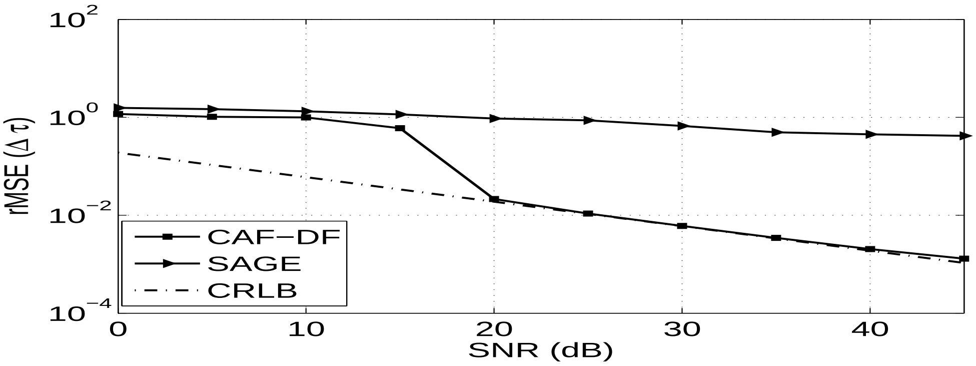

(c)

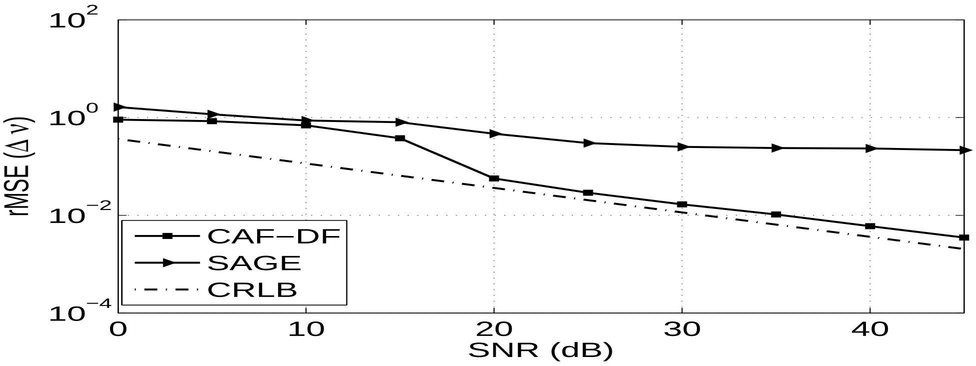

(d)

Figure 3.9: Joint-rMSE, obtained with the CAF-DF and the SAGE for 10 signal paths at different SNR values. (a): azimuth, (b): elevation, (c): time-delay and (d): Doppler shift.

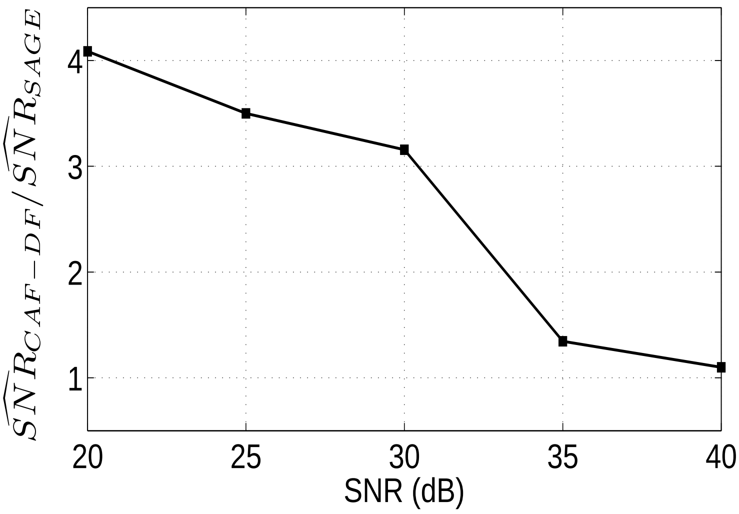

Figure 3.10: Ratio of estimated SNRs of CAF-DF and SAGE techniques for threshold and asymptotic regions of estimation performance using (2.33), (2.34).

3.4 Simulation Results on Real Ionospheric Data

In this section, performance of the CAF-DF technique is tested on recorded ionospheric data set from a high latitude HF link. The data sets are provided by Dr. E.M. Warrington and Dr. Alan Stocker from University of Leicester, Engineering Department, U.K. The signals were received on a six-element circular array. Transmitted pulse train consists of Barker-13 coded BPSK pulses modulated at 1667 baud with a repetition rate of 55 coded pulses per second. The total length of the sequence is 2 s. The transmitter and the receiver are located in Uppsala, Sweden and Kiruna, Sweden respectively. Data set is recorded in 2002. We analyzed a 1 hour data recorded at between $23:00:49-23:48:49$ at two different frequencies 4.63 MHz and 6.95 MHz, respectively. The obtained results for the CAF-DF technique are presented in figures 3.12, 3.13, and 3.14. As seen from the figures, the CAF-DF technique separated three different multipath components most of the observed time interval. Azimuth estimates are consistent with the relative orientations of the transmitter and receiver. There are no sharp changes in the azimuth, elevation, delay and Doppler shift estimates of the strongest signal source for nearly one hour measurement period. For the second and third signal sources we observe noisy elevation and delay estimates. We also investigated the performance of the CAF-DF technique over a second set of data which is recorded in April 13, 2007. This data set is recorded by using an eight-element inhomogeneous circular array is used as given in Fig. 3.11. As in the first set, Barker-13 coded BPSK pulses are used. In this data set, the baud rate is raised to 2000. The HF transmitter is located at Uppsala, Sweden and the receiver is at Bruntingthorpe, U.K. The distance between these two points is about 1417 km. In Fig. 3.15, estimated azimuth, elevation, delay and Doppler of the recorded data by CAF-DF at between $11:00:09-11:58:09$ are presented. Also for this data set, azimuth estimates are consistent with the relative orientations of the tranmitter and receiver. It is seen that elevation estimates of the 6.95 MHz are noisier than the other frequencies and consistent with the corresponding changes in delay estimates. Maybe the response of ionosphere at 6.95 MHz during the measurement period is not stable. Note that, the significant but orderly variation of the Doppler shifts observed within one hour duration indicate a physical mechanism that should be of interest to ionospheric physicists.

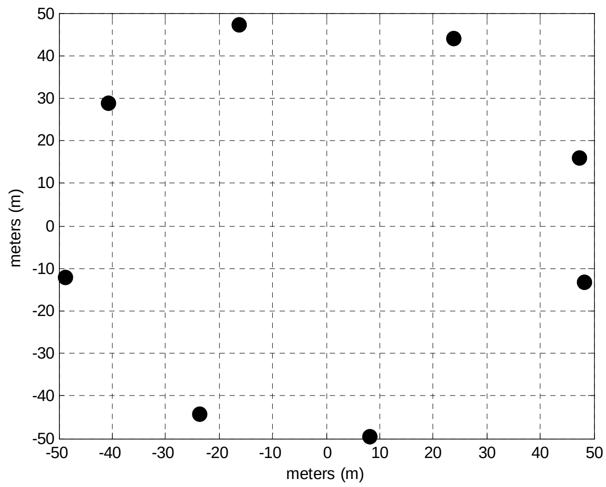

Figure 3.11: The spatial distribution of the eight-element circular antenna array used in the HF channel sounding experiment conducted between Uppsala, Sweden and Bruntingthorpe, U.K. The receiver array is located in Bruntingthorpe.

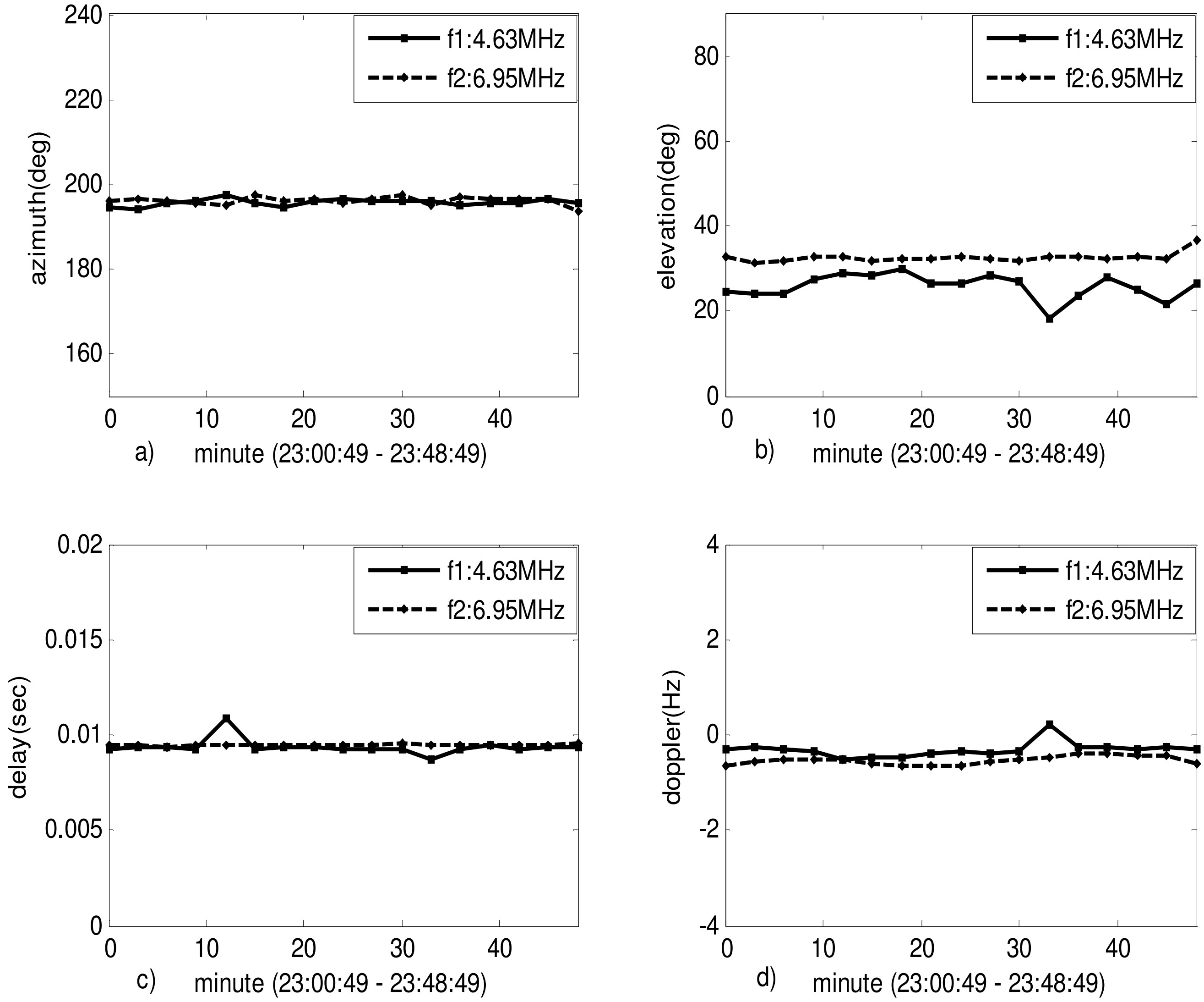

Figure 3.12: a)Azimuth, b)elevation, c)delay and d)Doppler shift estimates of the first signal source by CAF-DF of the data recorded in May 02, 2002 at between $23:00:49 - 23:48:49$ for two frequencies. Note that, in b) elevation estimates differ between two frequencies.

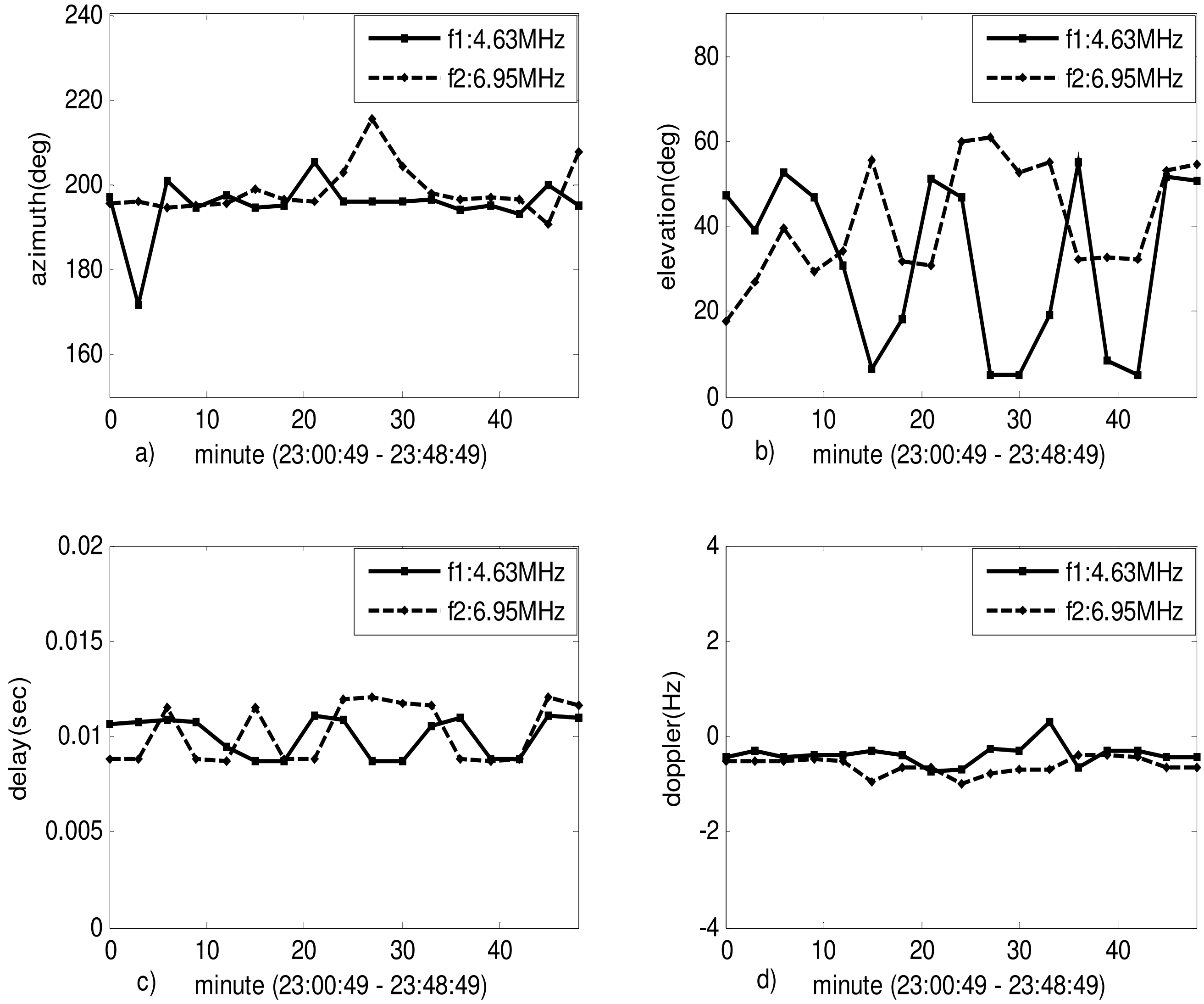

Figure 3.13: a)Azimuth, b)elevation, c)delay and d)Doppler shift estimates of the second signal source by CAF-DF of the data recorded in May 02, 2002 at between $23:00:49 - 23:48:49$ for two frequencies.

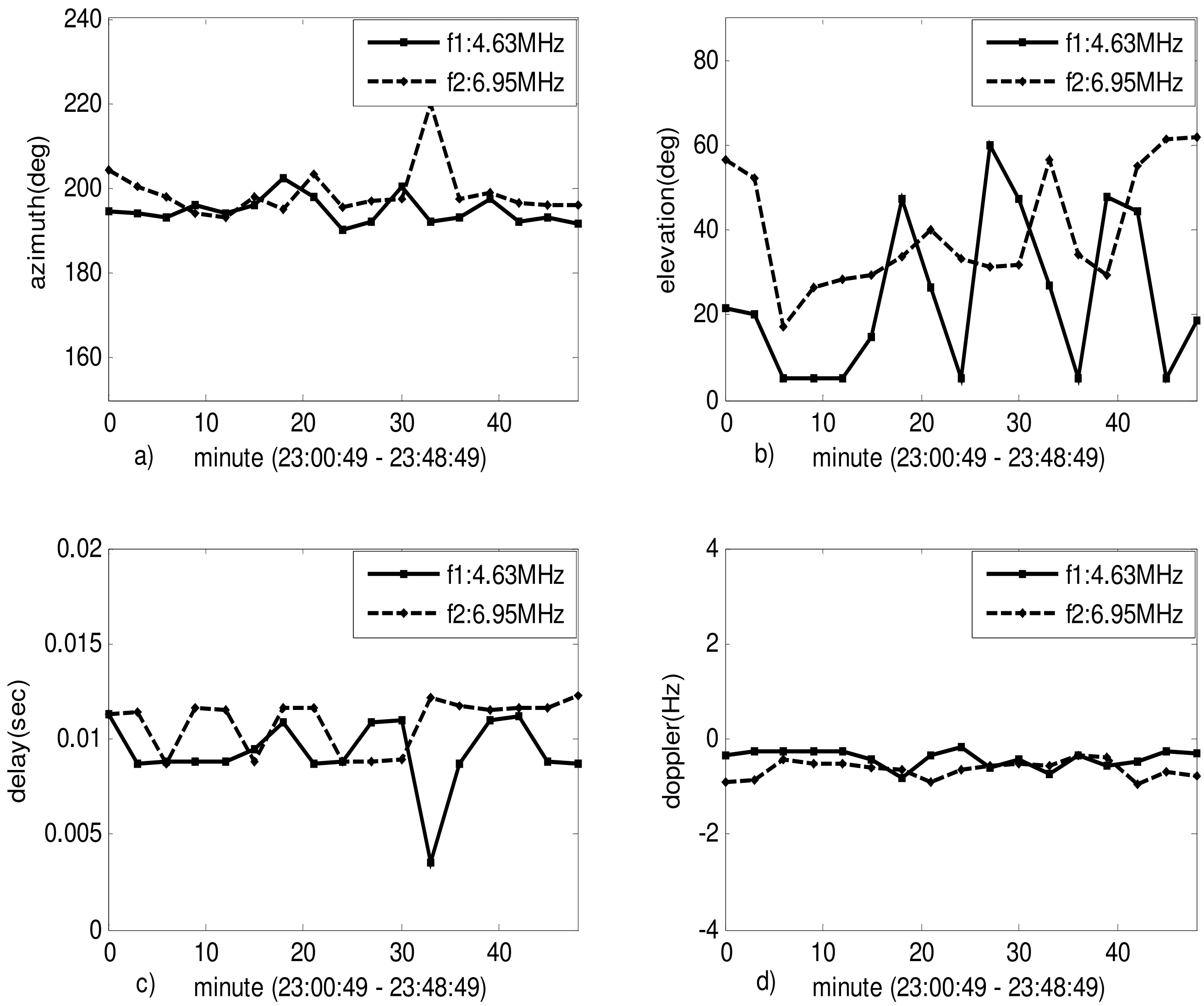

Figure 3.14: a)Azimuth, b)elevation, c)delay and d)Doppler shift estimates of the third signal source by CAF-DF of the data recorded in May 02, 2002 at between $23:00:49 - 23:48:49$ for two frequencies.

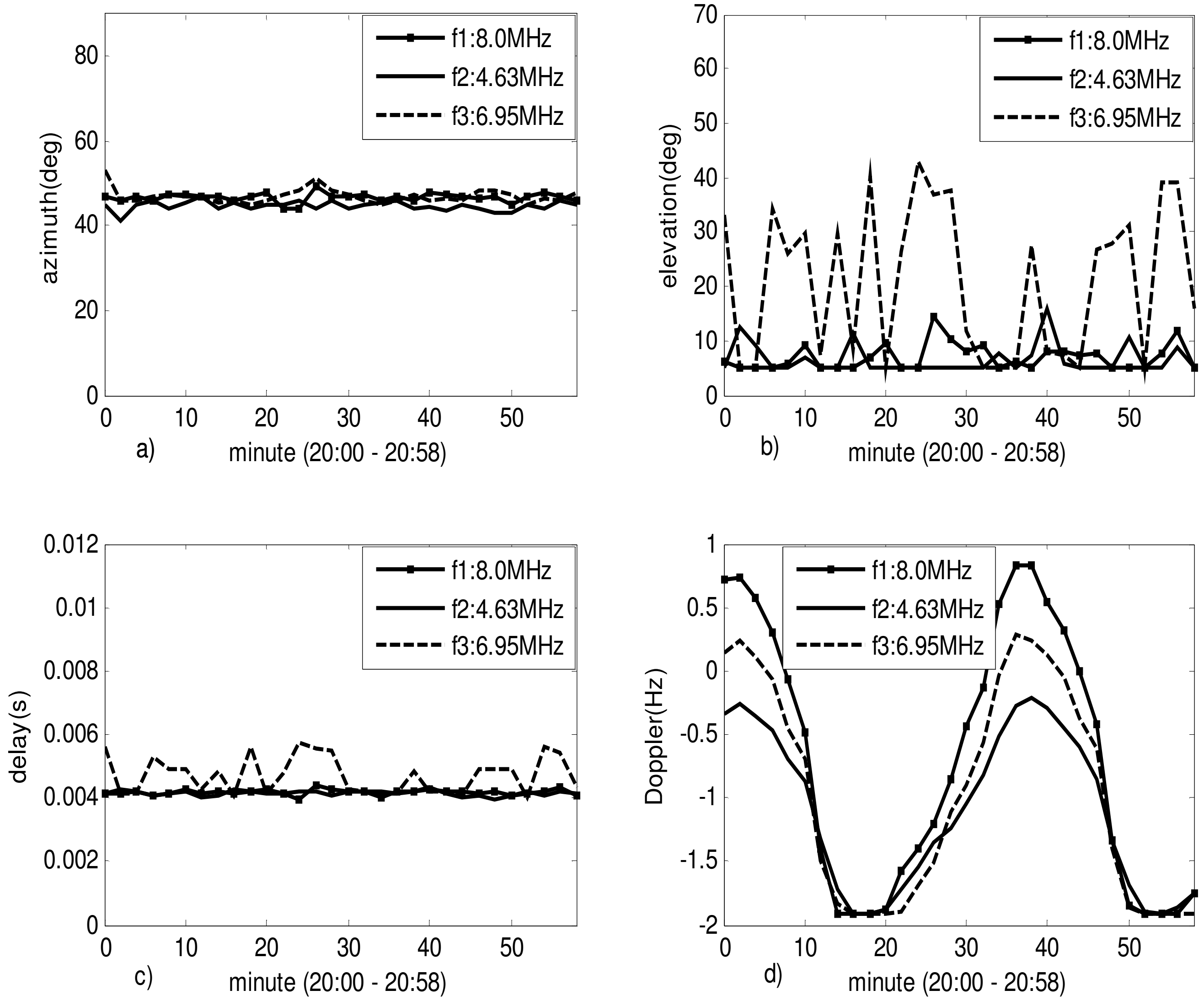

Figure 3.15: a)Azimuth, b)elevation, c)delay and d)Doppler estimates by CAF-DF of the data recorded in April 13, 2007 at between $11:00:09-11:58:09$ for three different frequencies. Note that the significant but orderly variations of the Doppler shifts in d) should be of interest.

3.5 Conclusions

A new array signal processing technique, the CAF-DF, is proposed for the estimation of multipath channel parameters including the path amplitude, delay, Doppler shift and DOAs. The proposed CAF-DF technique makes use of CAF computation for joint and reliable estimation of path parameters of individual multipath components. Extensive simulation results show that the CAF-DF technique is superior in terms of the rMSE to the SAGE technique over a wide range of SNR levels. Furthermore, the CAF-DF technique provides 2 to 3 dB improvement over the SAGE technique in the SNR of diversity combined detection signal. This improvement provided over the practical operational SNR range of receivers is a very significant advantage of the CAF-DF technique. Lastly, performance of the CAF-DF is verified on real ionospheric data.

Chapter 4

Multipath Channel Identification by Using Global Optimization in Ambiguity Function Domain

4.1 Introduction

Multipath is the most conspicuous feature of wireless channels that makes essential to model the communication channels due to the large number of propagating signals. Multipath propagation has bad and good faces. It is a bad thing because it leads to signal fading that effects reliable communication negatively. On the other hand, it is a good thing because it is the source of diversity which increases the rate and reliability of the communication. Multipath diversity shows up itself in several forms such as direction-of-arrival (DOA), time-delay and Doppler shift. In order to use diversity and mitigate the affect of multipath fading, wireless channel should be accurately modeled and channel state information (CSI) should be provided to the receiver.

In this chapter, a new array signal processing technique called particle swarm optimization - cross ambiguity function (PSO-CAF) is presented to estimate multipath channel parameters [48], [49], [50]. In order to exploit the delay Doppler diversity of the multipath signals, by using cross ambiguity function (CAF), the received array element outputs are transformed to delay-Doppler domain where the multipath signal components are localized to their respective delay and Doppler cell. Having identified the multipath clusters on the delay-Doppler domain, PSO is used to obtain globally optimal values of the channel parameters in each cluster.

In this chapter, algorithmic details of the PSO-CAF techniques is presented. The performance of the PSO-CAF technique is compared with the SAGE technique and with a recently proposed PSO based technique at various SNR levels.

4.2 Solution to CAF Domain Formulation by Using Particle Swarm Optimization

In a multipath environment, the receiver array output signals are delayed, Doppler-shifted and scaled versions of the transmitted signal. As mentioned in section 2.6, formulating a likelihood function for the channel estimation problem is a very common way to extract the signal parameters. However, when the number of paths increase, the ML approach face significant challenges in finding the global maximum of the likelihood function. This is mainly because of the fact that, likelihood maximization is performed in time domain, where there is a considerable overlap between the signals received from different paths. Therefore, it is desirable to formulate an alternative optimization problem other than the time domain where the multipath signal components are localized reducing the significant overlapping of components in the time domain. Since typical communication signals are phase or frequency modulated, with large time-bandwidth

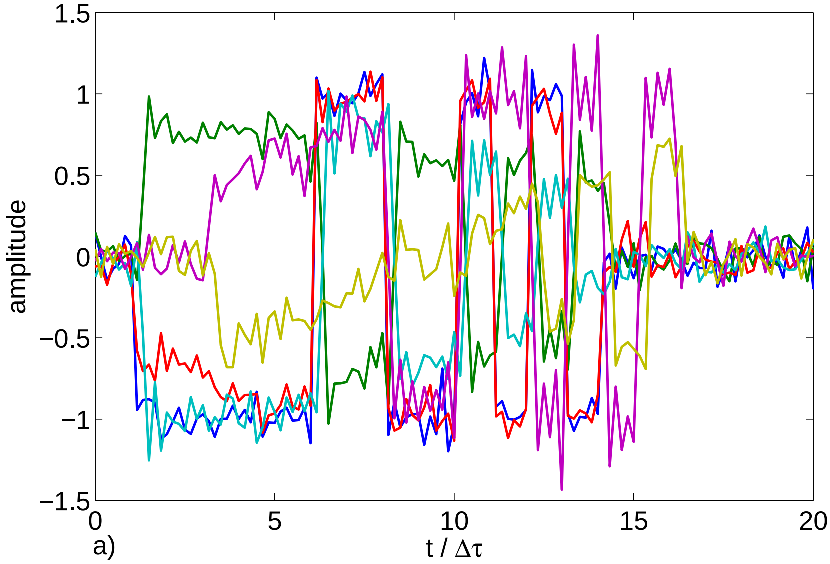

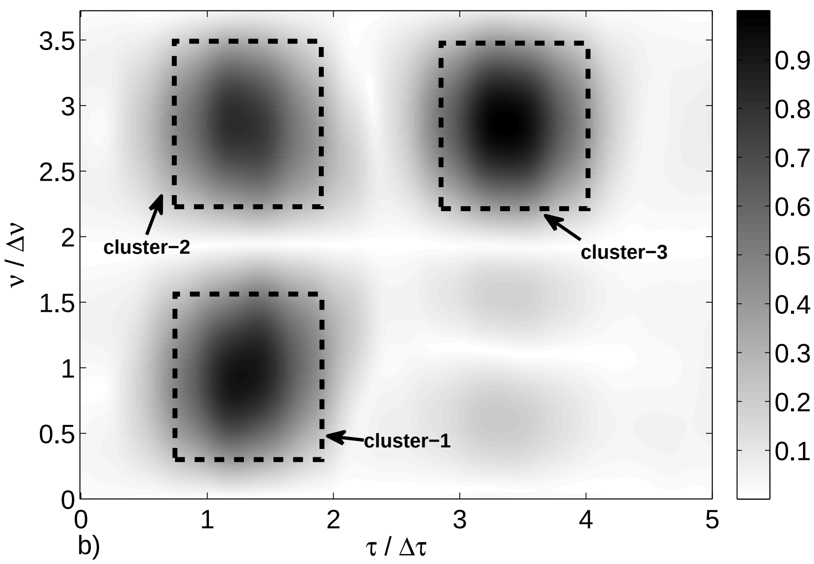

Figure 4.1: Barker-13 coded 6 paths a-) in time domain, and b-) in delay-Doppler domain localized in 3 clusters each of which has 2 paths.

products, as in radar detection their CAFs are highly localized in the delay-Doppler domain. Therefore, the transformation of the array signal outputs to the CAF domain localizes different multipath signals in clusters to their respective delay and Doppler cell. To detect the existing multipath signals, a constant false alarm criterion rate (CFAR) based adaptive threshold can be set. Such a strategy is commonly employed by radar target detection and will not be detailed here [98].

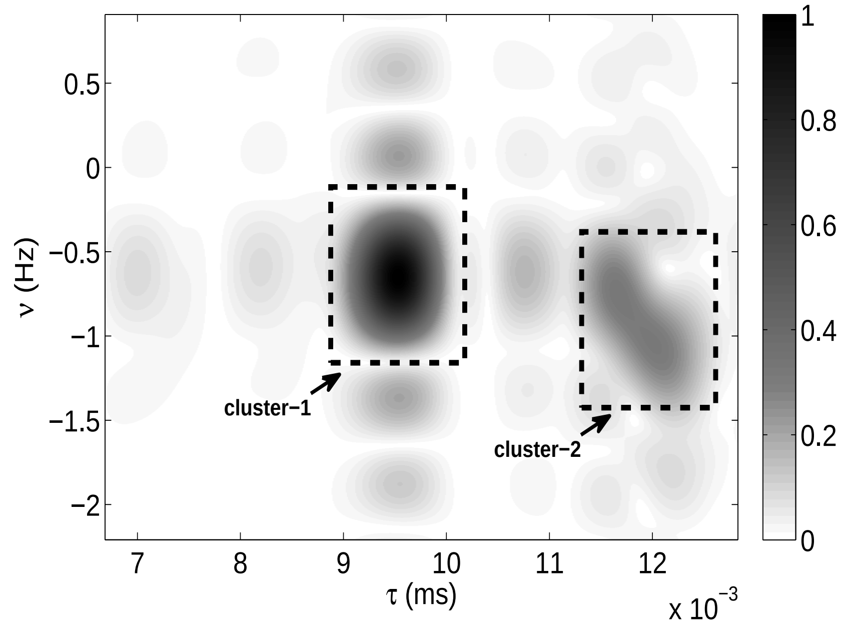

Figure 4.2: CAF between recorded multipath high-latitude ionosphere data and the transmitted signal. One dominant reflection in cluster-1 at $\tau = 9.5$ ms. Two reflections in cluster-2 between $\tau = 11.5 - 12.5$ ms.

Following the detection phase, around each detected delay-Doppler cell, a windowed set of data is extracted to be used for path identification. To illustrate this procedure, consider a synthetic multipath channel with 6 distinct paths. As shown in Fig. 4.1(a), the individual multipath signals overlap significantly in time at the output of an array element. However, as shown in Fig. 4.1(b), the CAF given in Eqn. (4.1) between the received signal and the transmitted signal localizes the contribution of different path components in delay-Doppler domain [96], [23]:

$$\boldsymbol{\chi}_{x(t),s(t)}(\tau,\nu) = \int_{-\infty}^{\infty} x\left(t+\frac{\tau}{2}\right) s^*\left(t-\frac{\tau}{2}\right) e^{-j2\pi\nu t} dt \ . \tag{4.1}$$

To illustrate the localization of multipath components in delay-Doppler domain, the CAF surface of a real high-latitude ionospheric communication channel is shown in Fig. 4.2. As seen from the result, two clusters can be reliably detected. Further analysis on the data has revealed that one of the clusters has a single component and the other has two multipath components [25],[24]. There is one dominant reflection in cluster-1 at $\tau = 9.5$ ms, and there are two reflections in cluster-2 between $\tau = 11.5 - 12.5$ ms. This localization enables us to reformulate the channel identification problem as a set of loosely coupled optimization problems in lower dimensional parameter spaces.

Signal flow diagram of the PSO-CAF algorithm is presented in Figs. 4.3 and 4.4. Note that, here we assume CAF peak detection has provided C clusters of paths in delay-Doppler domain and the number of paths in cluster c is d_c for $1 \le c \le C$. For example as shown in Fig. 4.1(b), 6 paths are localized in $C = 3$ clusters and each cluster consists of 2 paths. Having identified the location of each cluster, individual PSO searches are conducted for estimation of parameters of multipaths in each cluster. Following PSO searches in each cluster, effects of the estimated multipath components are eliminated for a better estimation in the remaining clusters. Since, optimization in each cluster has to be performed multiple times, PSO iterations in each cluster need not to be pursued until convergence is established. Therefore, by cycling over the identified set of clusters, the PSO-CAF technique iteratively provides estimates for each path in each cluster. In the following, details of the CAF domain optimization for each cluster is presented.

The optimization problem associated with the c^{th} cluster makes use of the following fitness function:

$$f_c(\boldsymbol{\varphi}(\mathbf{S_c}, \boldsymbol{\eta}), \boldsymbol{\zeta}_c(\eta)) = \sum_{m=1}^{M} \left\| \boldsymbol{\Gamma}_{c,m} - \mathbf{vec}\left(\mathbf{W}_c \boldsymbol{\chi}_{\hat{u}_m(t;\boldsymbol{\varphi}(\mathbf{S}_c,\eta)),s(t)}(\tau,\nu) \right) \right\|^2 \quad , \tag{4.2}$$

where $\mathbf{S}_c$ is the set containing indexes of d_c path components in the c^{th} cluster, $\mathbf{vec}(.)$ is vector operator stacking the columns of a matrix into a single column vector, $\mathbf{W}_c$ is the identifier mask for the c^{th} cluster that selects the patch that will be used in PSO, and

$$\boldsymbol{\Gamma}_c = [\boldsymbol{\Gamma}_{c,1}, ..., \boldsymbol{\Gamma}_{c,M}]^T \quad , \tag{4.3}$$

is the matrix of the c^{th} cluster CAF patch for M antennas with elements:

$$\boldsymbol{\Gamma}_{c,m} = \mathbf{vec}\left(\mathbf{W}_c \boldsymbol{\chi}_{\hat{y}_{c,m}(t;\eta),s(t)}(\tau,\nu) \right) \quad . \tag{4.4}$$

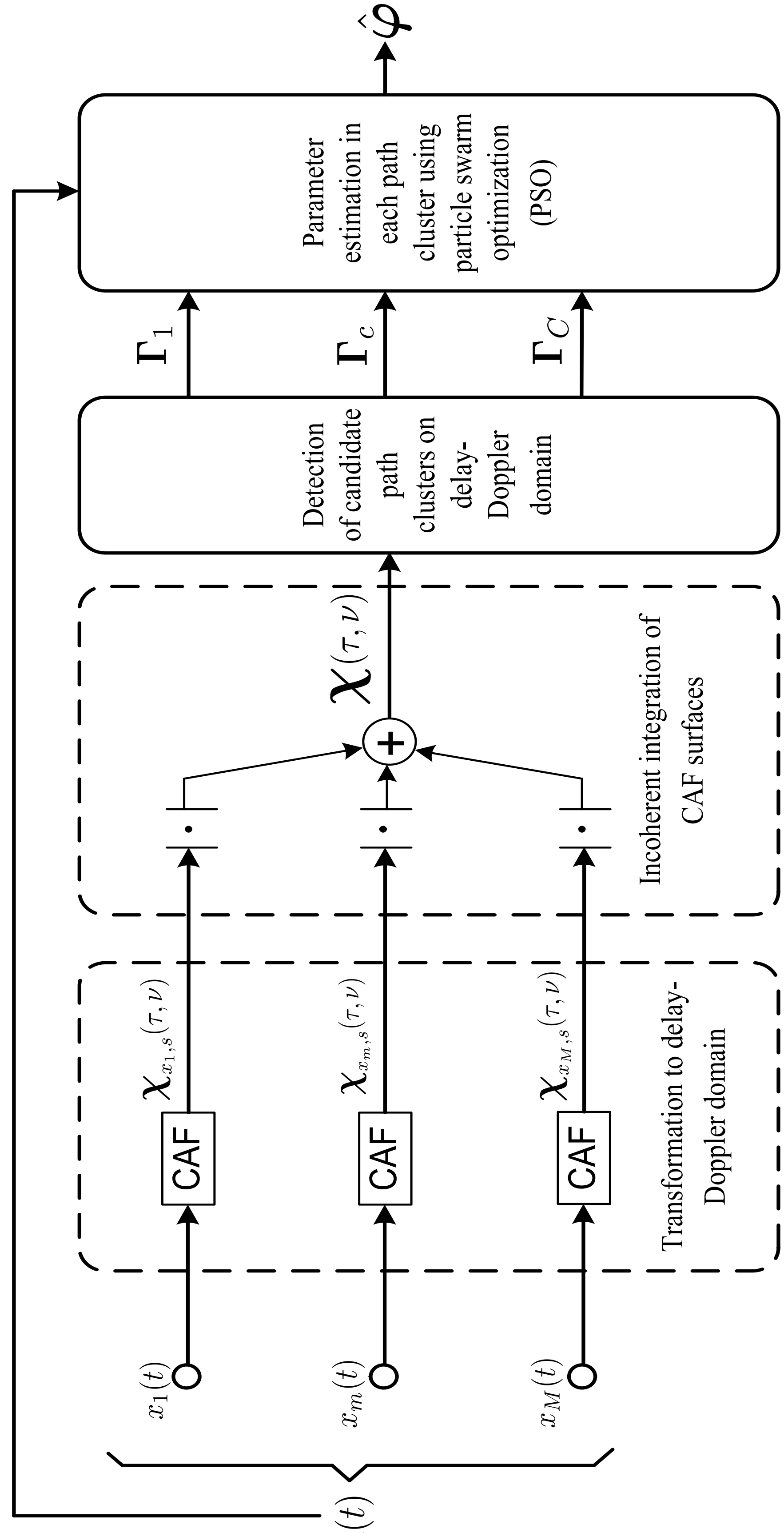

Figure 4.3: Signal flow diagram of the PSO-CAF algorithm.

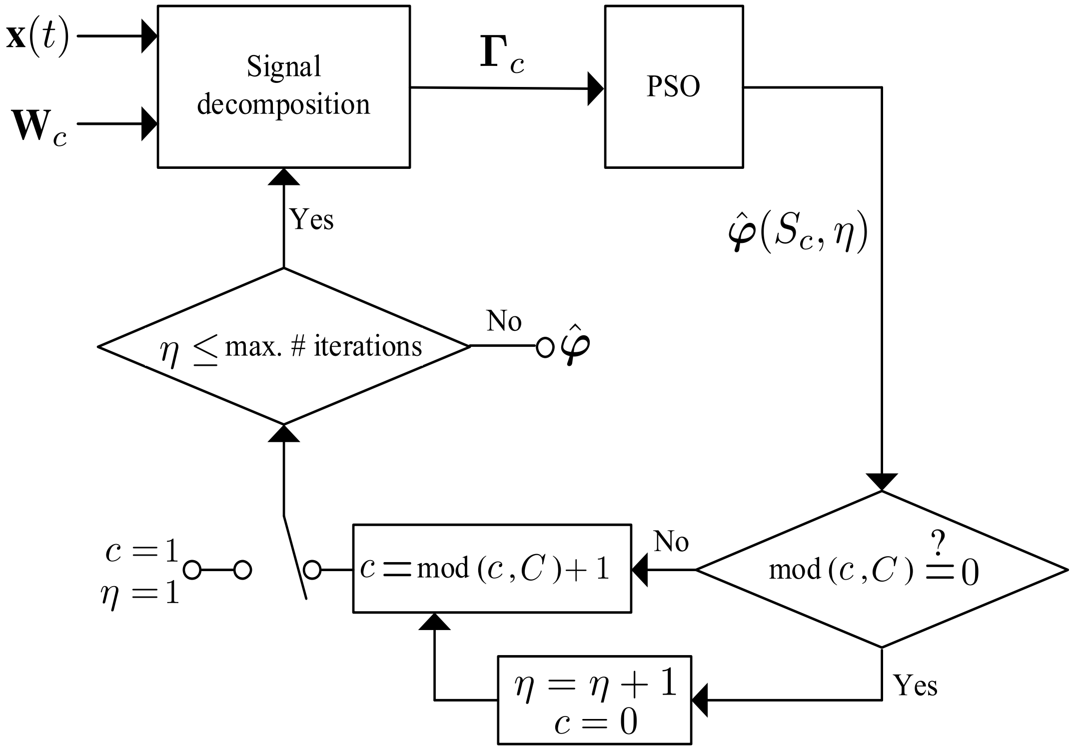

Figure 4.4: Signal flow sub-block diagram of the parameter estimation in each cluster using PSO block in Fig. 4.3 .

$\boldsymbol{\chi}_{\hat{y}_{c,m}(t;\eta),s(t)}(\tau,\nu)$ is the CAF between $\hat{y}_{c,m}(t;\eta)$ and $s(t)$, $\boldsymbol{\chi}_{\hat{u}_m(t;\boldsymbol{\varphi}(\mathbf{S}_c,\eta)),s(t)}(\tau,\nu)$ is the CAF between $\hat{u}_m(t;\boldsymbol{\varphi}(\mathbf{S}_c,\eta))$ and $s(t)$, and

$$\hat{\mathbf{y}}_c(t;\eta) = [\hat{y}_{c,1}(t;\eta), ..., \hat{y}_{c,M}(t;\eta)] \quad , \tag{4.5}$$

is the estimated array output at the η^{th} iteration corresponding to c^{th} cluster:

$$\hat{\mathbf{y}}_c(t;\eta) = \mathbf{x}(t) - \sum_{\gamma=1,\gamma\neq c}^{C} \hat{\mathbf{u}}(t;\boldsymbol{\varphi}(\mathbf{S}_\gamma,\eta)) \quad , \tag{4.6}$$

where

$$\hat{\mathbf{u}}(t;\boldsymbol{\varphi}(\mathbf{S}_c,\eta)) = [\hat{u}_1(t;\boldsymbol{\varphi}(\mathbf{S}_c,\eta)), .., \hat{u}_M(t;\boldsymbol{\varphi}(\mathbf{S}_c,\eta))]^T \quad , \tag{4.7}$$

is the matrix generated with the c^{th} cluster estimated multipath parameters for M antennas with elements:

$$\hat{\mathbf{u}}(t;\boldsymbol{\varphi}(\mathbf{S}_c,\eta)) = \sum_{i\in\mathbf{S}_c} \zeta_i(\eta) s(t-\tau_i(\eta)) e^{j2\pi\nu_i(\eta)t} \mathbf{a}(\theta_i(\eta),\phi_i(\eta)) \ . \tag{4.8}$$

In the first iteration, $\eta = 1$, for the first cluster, $\hat{\mathbf{y}}_c(t;\eta)$ is initialized as $\hat{\mathbf{y}}_c(t;\eta) = \mathbf{x}(t)$. Using (4.8), $\boldsymbol{\chi}_{\hat{u}_m(t;\boldsymbol{\varphi}(\mathbf{S}_c,\eta)),s(t)}(\tau,\nu)$ can be written as

$$\boldsymbol{\chi}_{\hat{u}_m(t;\boldsymbol{\varphi}(\mathbf{S}_c,\eta)),s(t)}(\tau,\nu) = \sum_{i\in\mathbf{S}_c} \zeta_i(\eta)\mathbf{A}_m(\tau,\nu;\boldsymbol{\varphi}_i(\eta)) \quad , \tag{4.9}$$

where $\mathbf{A}_m(\tau,\nu;\boldsymbol{\varphi}_i(\eta))$ is defined as:

$$\begin{aligned} \mathbf{A}_m(\tau,\nu;\boldsymbol{\varphi}_i(\eta)) \quad &= \quad a_m(\theta_i(\eta),\phi_i(\eta)) \\ &\cdot \quad \int_{-\infty}^{\infty} s\left(t-\tau_i(\eta)+\frac{\tau}{2}\right)s^*\left(t-\frac{\tau}{2}\right)e^{-j2\pi(\nu-\nu_i(\eta))t}dt \quad . \end{aligned} \tag{4.10}$$

By using (4.4) and (4.10), a more compact form for the fitness function in (4.2) can be obtained as:

$$f_c(\boldsymbol{\varphi}(\mathbf{S}_c),\boldsymbol{\zeta}_c) = \sum_{m=1}^{M} \|\boldsymbol{\Gamma}_{c,m} - \boldsymbol{\Upsilon}_{c,m}\boldsymbol{\zeta}_c\|^2 \quad . \tag{4.11}$$

Here, matrix $\boldsymbol{\Upsilon}_{c,m}$ is defined as:

$$\boldsymbol{\Upsilon}_{c,m} = \left[\mathbf{vec}(\mathbf{W}_c\mathbf{A}_m(\tau,\nu;\boldsymbol{\varphi}_{\varrho_1}(\eta))),...,\mathbf{vec}(\mathbf{W}_c\mathbf{A}_m(\tau,\nu;\boldsymbol{\varphi}_{\varrho_{d_c}}(\eta)))\right] \quad , \tag{4.12}$$

where ϱ_1 is the first index element of the index set $\mathbf{S}_c$ and each column correspond to a multipath component in the c^{th} cluster. Straightforward minimization with respect to the scale variables $\boldsymbol{\zeta}$ yields:

$$\hat{\boldsymbol{\zeta}}_c(\eta) = \frac{1}{M}\sum_{m=1}^{M} \left(\boldsymbol{\Upsilon}_{c,m}^H\boldsymbol{\Upsilon}_{c,m}\right)^{-1}\boldsymbol{\Upsilon}_{c,m}^H\boldsymbol{\Gamma}_{c,m} \quad , \tag{4.13}$$

which, as in the ML approach culminating with (2.56), when substituted into (4.11), reduces the fitness function for the c^{th} cluster to:

$$f_c(\boldsymbol{\varphi}(\mathbf{S}_c,\eta)) = \sum_{m=1}^{M} \left\|\boldsymbol{\Gamma}_{c,m} - \boldsymbol{\Upsilon}_{c,m}\hat{\boldsymbol{\zeta}}_c(\eta)\right\|^2. \tag{4.14}$$

Thus, the channel parameter estimates for the c^{th} cluster at η^{th} iteration are obtained by minimizing the following optimization problem:

$$\hat{\boldsymbol{\varphi}}(S_c,\eta) = \arg\min_{\boldsymbol{\varphi}} \quad f_c(\boldsymbol{\varphi}(\mathbf{S}_c,\eta)) \quad . \tag{4.15}$$

Location of each particle, $\mathbf{z}_l = [\boldsymbol{\varphi}_{\varrho_1}, ..., \boldsymbol{\varphi}_{\varrho_i}, ..., \boldsymbol{\varphi}_{\varrho_{d_c}}]$, $i \in \mathbf{S}_c$, in the $K = 4 \times d_c$ dimensional search space is a solution candidate. The size of the target delay-Doppler patch, $\boldsymbol{\Gamma}_c$, determined by the identifier mask $\mathbf{W}_c$, is chosen to be $1.5\Delta\tau \times 1.5\Delta\nu$ around the detected peak for the c^{th} cluster. Resolution of delay and Doppler in the CAF domain are $\Delta\tau = 1/BW$ and $\Delta\nu = 1/T$, respectively [23]. Here, BW corresponds to the bandwidth and T is the duration of $s(t)$. Moreover, particle movements are confined in a window of size $\Delta\tau \times \Delta\nu$ around the detected peak for the c^{th} cluster. Equation (4.14) is evaluated using the location values of each particle and the location that gives the best fitness chosen as the ***globalBest***. Having estimated the parameters of each multipath component in the c^{th} cluster, effects of these multipath components are eliminated as in (4.6) from the array output for a better estimation in remaining clusters. Iterations, η, continue until convergence is established or a preset number of iterations is reached.

4.3 Simulation Results

In this section, we present results of simulated experiments conducted to compare the performances of the PSO-CAF, SAGE and PSO-ML techniques on signals at different SNR values. The CRLB for the joint estimation problem is also included for comparison. In Table 2.1, the basic form of the SAGE algorithm, which is widely used in channel identification, is presented. PSO-ML is a recently proposed technique, which applies PSO to ML criterion to estimate the path parameters [99]. Since, PSO-ML does not exploit the delay-Doppler localization of the multipath components, it operates in a significantly higher dimensional search space than the PSO-CAF.

In the experiments, received signals of a circular receiver array of $M = 9$ omnidirectional sensors at positions $[r\cos(m2\pi/M), r\sin(m2\pi/M)]$, $1 \leq \ldots \leq$

M, is simulated. The radius of the array $r = \lambda/4\sin(\pi/M)$ is chosen such that the distance between two neighboring sensors is $\lambda/2$, where λ is the carrier wavelength. The transmitted training signal consists of 6 Barker-13 coded pulses with a duration of $13\Delta\tau$ where $\Delta\tau$ is the chip duration. The pulse repetition interval is $30\Delta\tau$ resulting a total signal duration of $qT = 167\Delta\tau$. The SNR is defined at a single sensor relative to the noise variance as $E[|x_m(t)|^2]/E[|n_m(t)|^2]$. The joint rMSE defined in (3.14) is used for performance comparisons.

Moreover, for both of the experiments, the same PSO settings, such as swarm size, update rules, swarm topology and swarm initialization, are chosen based on recommendations in the literature and empirical simulations [100]. We observed that fine tuning the parameters would not provide significant improvements. Therefore, here standard PSO is used and results of different PSO variants are not presented. Initial locations and velocities of the particles are randomly distributed throughout the search space. As stated previously, size of the delay-Doppler swarm search space is taken as $\Delta\tau \times \Delta\nu$ around the detected peak of each cluster. Number of particles in the swarm is chosen as 50. Necessary number of PSO evaluations and SAGE iterations are conducted for PSO-ML, PSO-CAF and SAGE techniques, respectively, to ensure the convergence.

In the first experiment, we considered a multipath scenario with 6 paths, whose parameters are given in the top 6 rows of Table 4.1. Note that these 6 paths are clustered in 3 clusters each containing 2 paths. As stated previously and presented in Fig. 4.1(a)-4.1(b), the key advantage of the PSO-CAF technique is the localization of different multipath signals to their respective delay and Doppler cells by transforming the array signal outputs to the CAF domain. By this way, we are able to use PSO in lower dimensional parameter search spaces in each cluster to estimate the respective path parameters. The performance improvement due to clustering on delay-Doppler domain is presented in Fig. 4.5 and Fig. 4.6 for the PSO-CAF technique. In the figures one snapshot coordinates

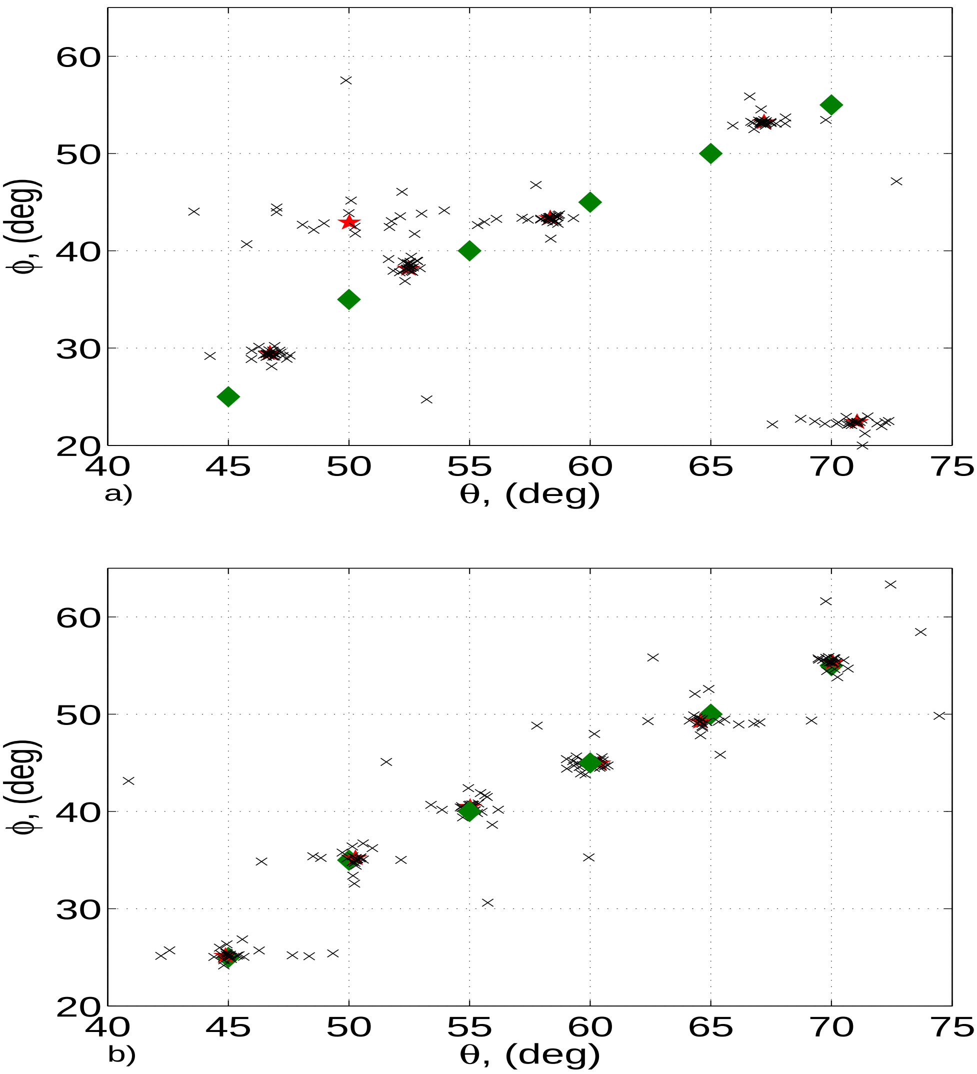

Figure 4.5: One snapshot coordinates, obtained by using the PSO-CAF, of particles ($\mathbf{z}$, $\times$), exact path parameter values ($\blacklozenge$) and **globalBest** ($\mathbf{p}_g$, $\star$) distributed on the azimuth (θ)-elevation ((ϕ)) plane. a): No clustering, PSO is conducted in 24-dimensional space. b): 3 clusters, parallel PSO is conducted in each of them in 8-dimensional spaces.

of particles ($\mathbf{z}$, $\times$), exact path parameter values ($\blacklozenge$) and coordinate of **globalBest** ($\mathbf{p}_g$, $\star$) are plotted during the PSO optimization. As can be seen, when all the paths are tried to be identified without delay-Doppler domain clustering, particles typically converge to local minima of the fitness function and rarely reach the exact path parameter coordinates. However, if we conduct 3 separate 8 dimensional PSO path parameter searches on each cluster, particles converge

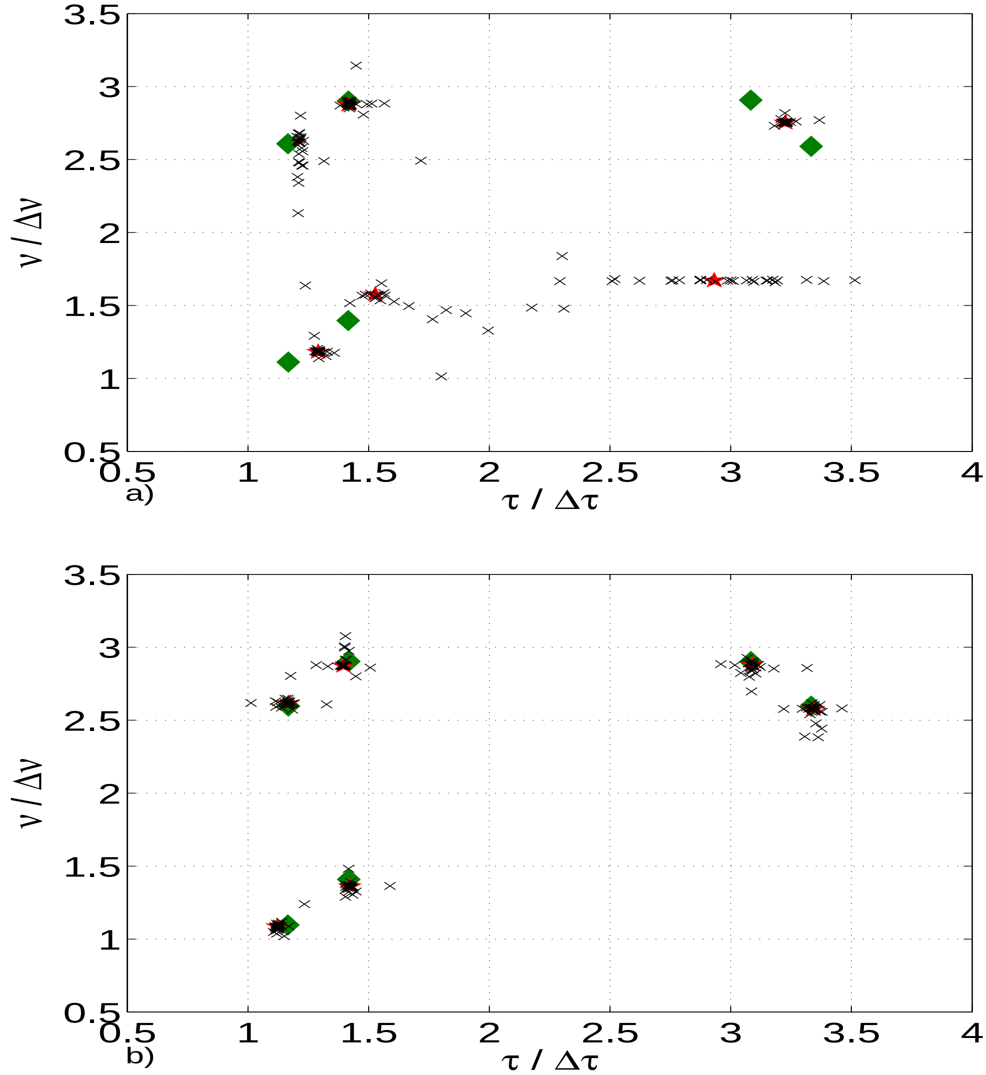

Figure 4.6: One snapshot coordinates, obtained by using the PSO-CAF, of particles ($\mathbf{z}$, $\times$), exact path parameter values ($\blacklozenge$) and **globalBest** ($\mathbf{p}_g$, $\star$) distributed on the delay-Doppler plane. a): No clustering, PSO is conducted in 24-dimensional space. b): 3 clusters, parallel PSO is conducted in each them in 8-dimensional spaces.

to the global minima in each cluster in a shorter time with increased frequency. In Fig. 4.7(a), normalized fitness progress curves of PSO-ML and PSO-CAF techniques are seen. As expected, PSO-CAF has better convergence properties. Fig. 4.7(b) shows the normalized error progress of the array output estimates of the SAGE algorithm. All simulations are conducted on an HP xw6400 Workstation with Intel Xeon 3Ghz processor. A single iteration for the PSO-CAF, the

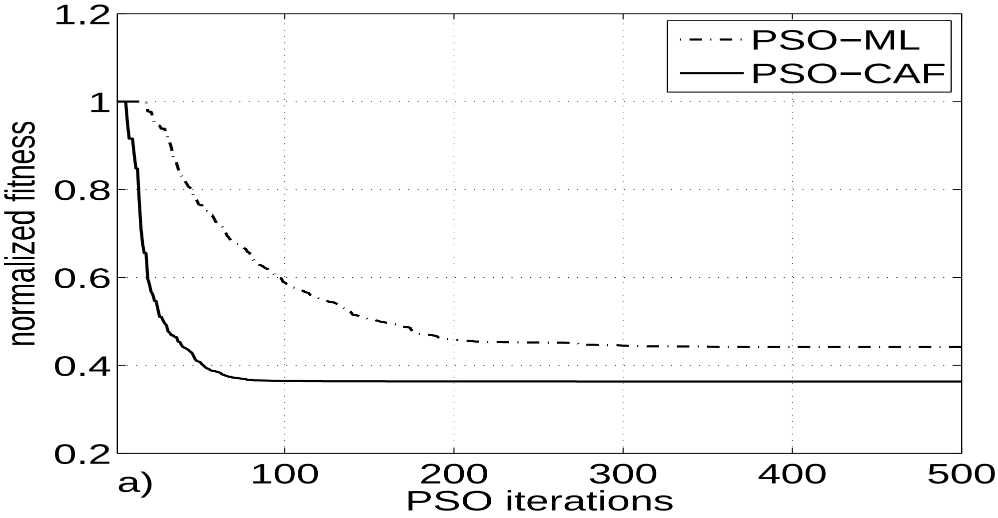

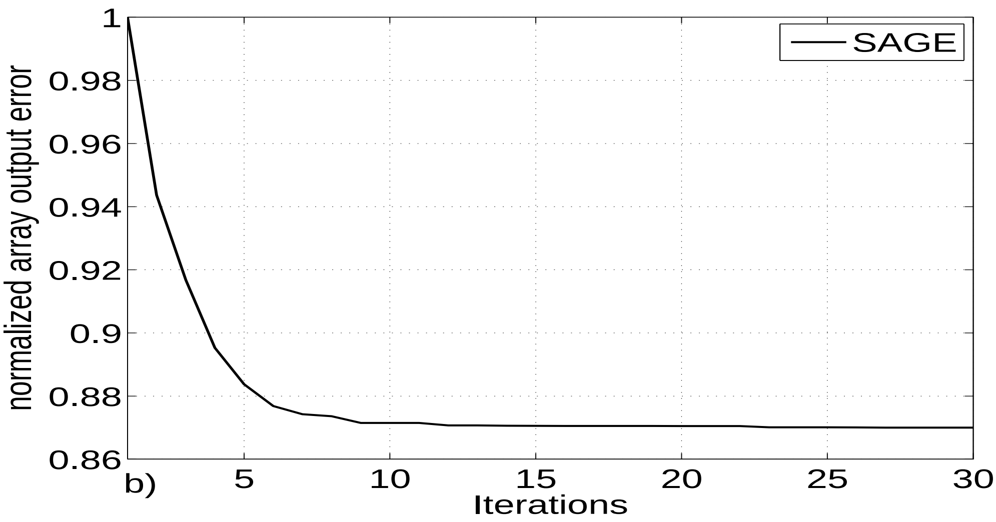

Figure 4.7: a) Normalized fitness progress curves of the PSO-ML and the PSO-CAF. b) Normalized array output error progress curve of SAGE.

PSO-ML and the SAGE techniques take approximately as 2.5, 1.1, and 9.4 sec, respectively. As shown in Fig. 4.7(a) and 4.7(b), the PSO-CAF, the PSO-ML and the SAGE techniques establish their convergence at around 80, 200 and 10 iterations. Therefore, until convergence, the PSO-CAF, the PSO-ML and the SAGE techniques require approximately 200, 220, and 94 sec, respectively. Since the PSO based techniques can be implemented on a multicore processor environment with significantly less interprocessor communication requirements, the processing times can be reduced to the level of the SAGE technique. Therefore,

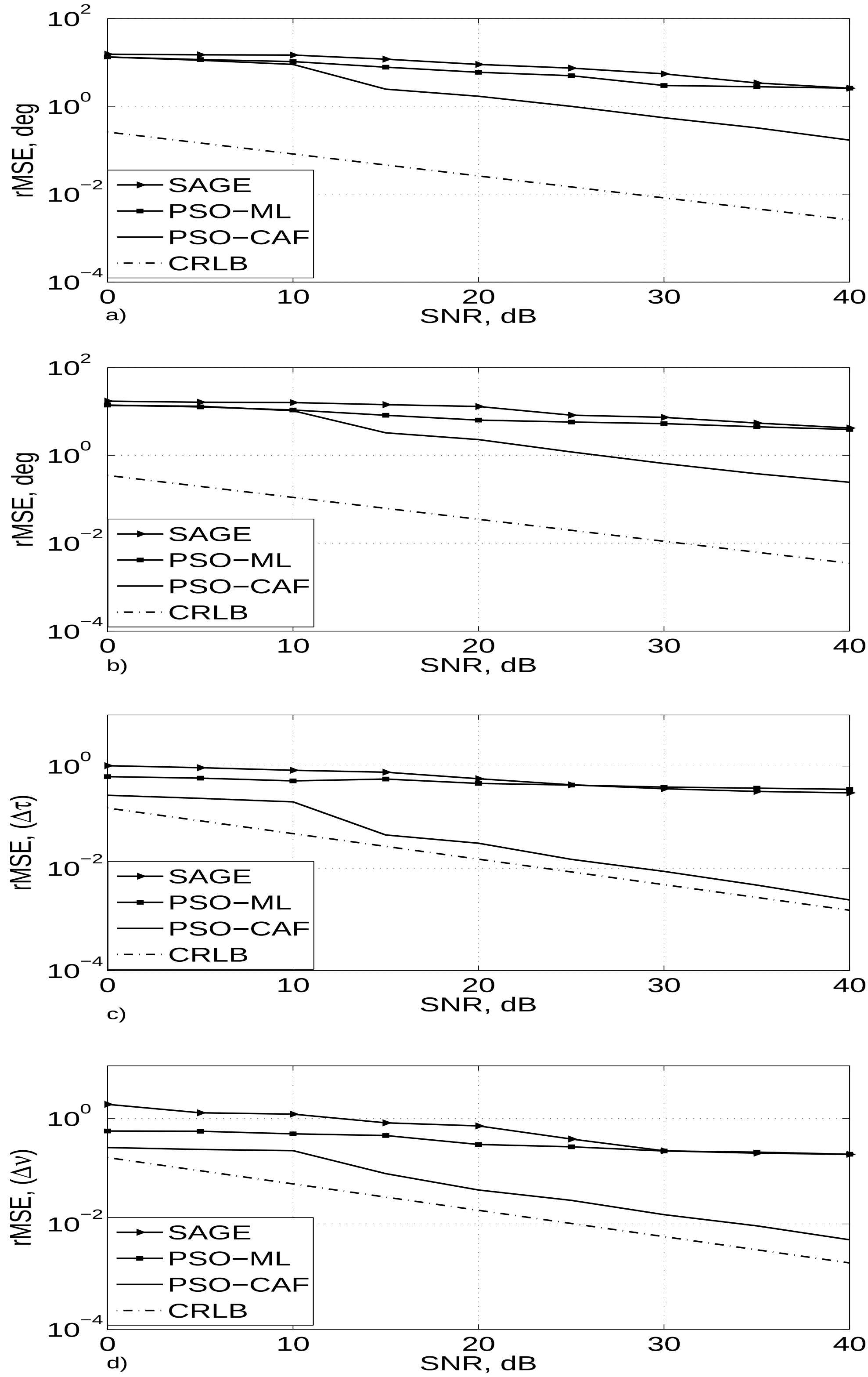

Figure 4.8: Joint-rMSE, obtained with the PSO-CAF, the PSO-ML and the SAGE, of (a): azimuth, (b): elevation, (c): time-delay and (d): Doppler shift of 6 signal paths. Dash-dot line represents the CRLB.

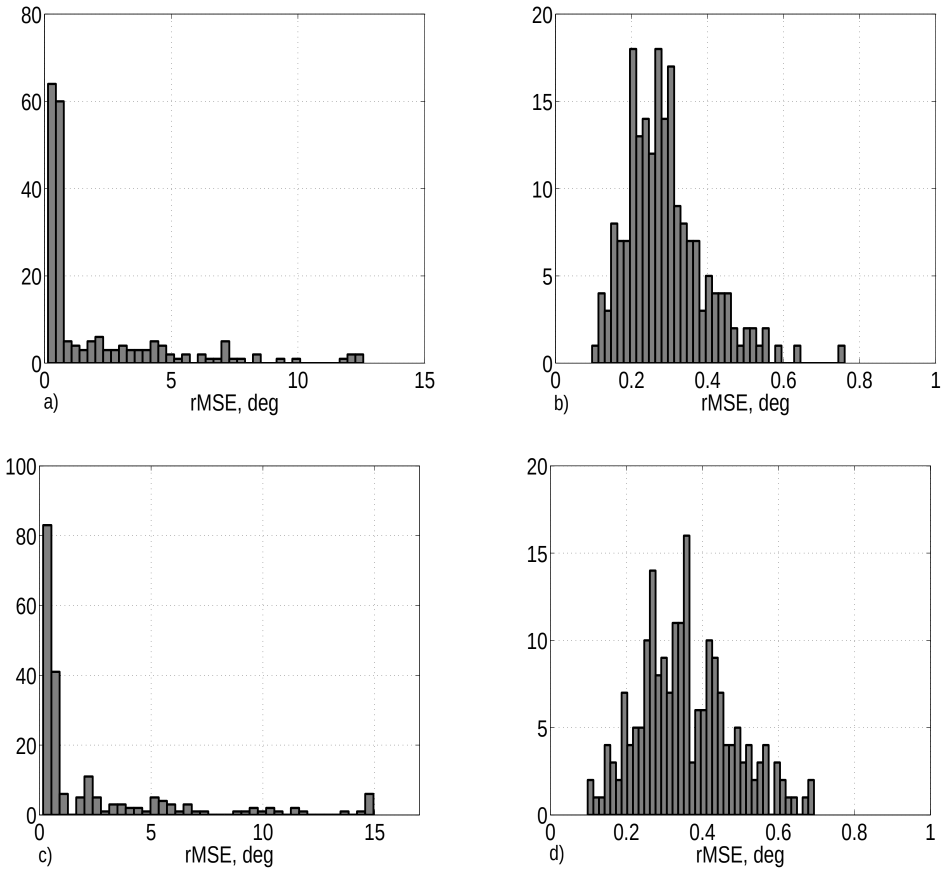

Figure 4.9: Histograms of joint rMSE values of a-b): azimuth, c-d): elevation obtained with the PSO-ML and PSO-CAF techniques. b-d): PSO-CAF. a-c): PSO-ML.

in the following we will base our comparison results to the accuracy of the estimated parameters. Fig. 4.8 shows the joint rMSE values obtained from the SAGE, PSO-ML and PSO-CAF for various SNR values. Also to provide a lower bound on the error, the CRLB is included. Obtained results shows the superior performance of the PSO-CAF over the PSO-ML and the SAGE techniques for all SNR values. The PSO-ML and the SAGE techniques have similar performances at high SNR values, however at lower SNR values the PSO-ML outperforms the SAGE technique. Moreover, histograms of joint rMSE of each technique are presented in Fig. 4.9 to provide an insight into the failure statistics. Consistent with the previous results, most of the time, the PSO-ML and SAGE techniques fail to convergence true parameter values. By using (2.33) and (2.34), in Fig. 4.11, estimated $\widehat{\mathrm{SNR}}_{PSO-CAF}/\widehat{\mathrm{SNR}}_{PSO-ML}$ ratio is plotted for threshold and asymptotic

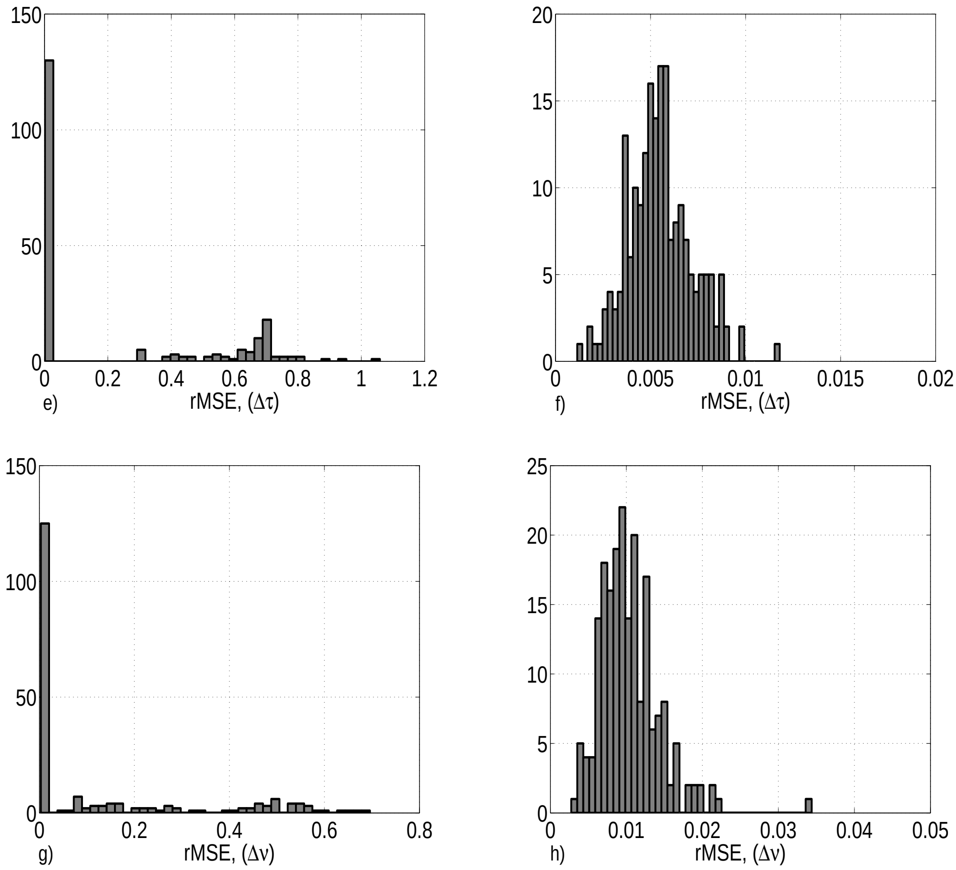

Figure 4.10: Histograms of joint rMSE values of e-f): delay, g-h): Doppler obtained with the PSO-ML and PSO-CAF techniques. f-h): PSO-CAF. e-g): PSO-ML.

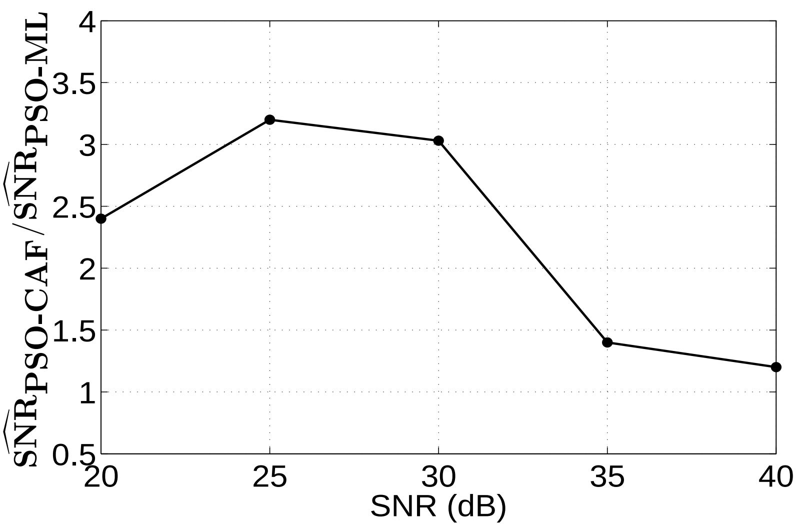

Figure 4.11: Ratio of estimated SNR levels of the PSO-CAF and the PSO-ML techniques for threshold and asymptotic regions of estimation performance.

regions of estimation performance. The PSO-CAF combines diversity better than the PSO-ML which enable detector to accurately retrieve the transmitted information.

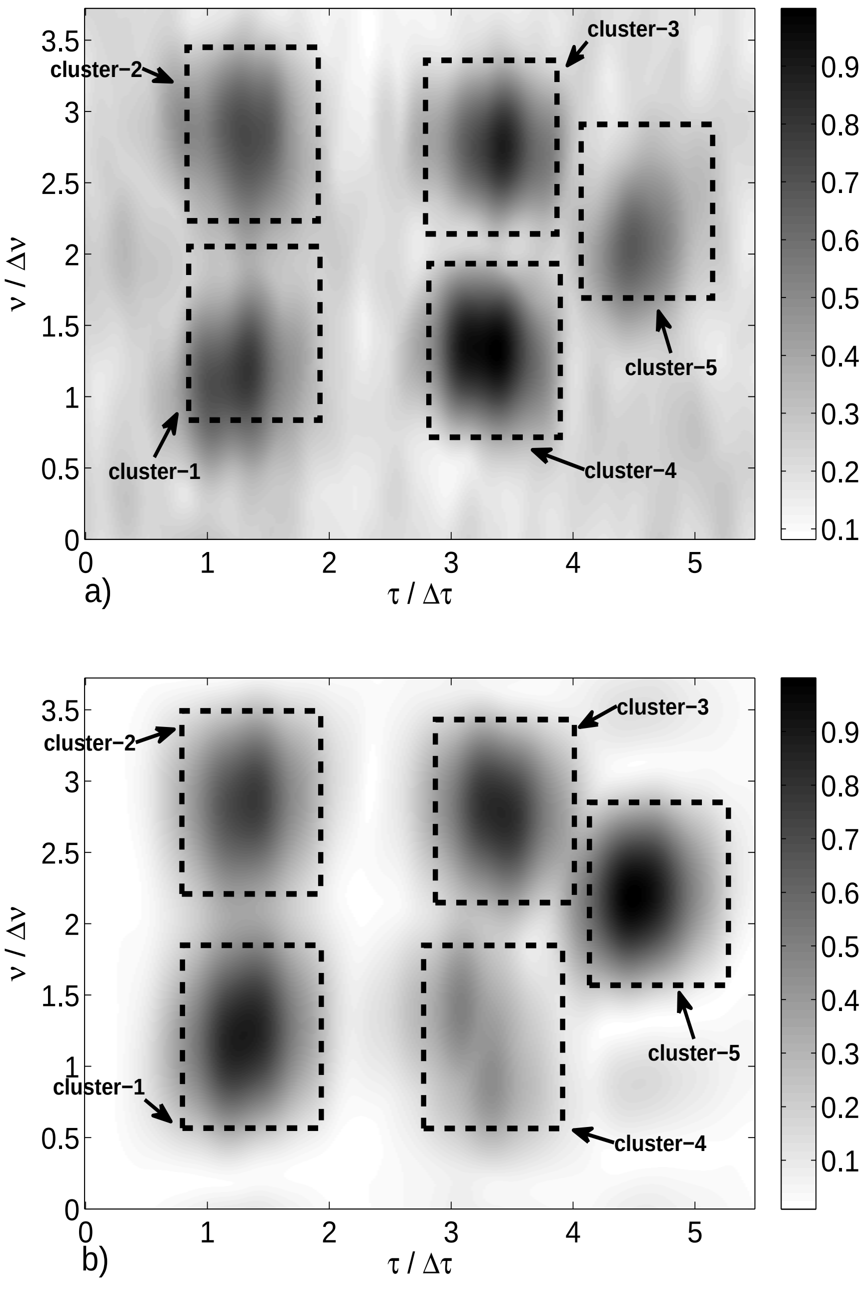

Figure 4.12: CAF's between received signal, consisting of 10 multipath components, with the transmitted signal at a): 10 dB, b): 35 dB.

Table 4.1: 10 path parameters. Time-delay, Doppler and complex scaling factor values are normalized by $\Delta\tau$, $\Delta\nu$ and $e^{j\psi_i}$, respectively. ψ_i's, $i = 1, ..., d$, are uniformly distributed between $[0, 2\pi]$.

path	θ(deg)	ϕ(deg)	$\tau/\Delta\tau$	$\nu/\Delta\nu$	$\zeta/e^{j\psi_i}$
1	45	25	1.16	1.1	1
2	50	35	1.41	1.4	0.9
3	55	40	1.16	2.6	0.9
4	60	45	1.41	2.9	1
5	65	50	3.08	2.9	0.9
6	70	55	3.33	2.6	0.85
7	75	38	3.16	1.4	1
8	57	47	3.5	1.1	0.8
9	63	43	4.41	2.1	0.9
10	63	43	4.66	2.3	0.92

In the second experiment, we considered a multipath scenario where there exist 5 clusters containing 2 paths each totaling 10 paths with parameters tabulated in Table 4.1, distributed in 5 different clusters. In Fig. 4.12, to clarify the detection process of delay-Doppler cells corresponding to each multipath cluster, locations of 5 different clusters on the CAF surface are presented at different SNR values. Even at the 10 dB SNR, all clusters are localized and can be identified on the CAF detection surface. Note that the number of paths exceeds the number of sensors which would made it impossible to resolve with narrowband systems. However, if there exist fewer paths than the number of array elements in each resolvable delay-Doppler cell then delay-Doppler domain diversity of the paths can be exploited to resolve the paths in wideband communication systems. Fig. 4.13, illustrates the joint rMSE values obtained from SAGE, PSO-ML and PSO-CAF for various SNR values. Similar to the results of the first experiment, PSO-CAF is able to resolve multipath components even in this scenario successfully and outperforms the PSO-ML and SAGE.

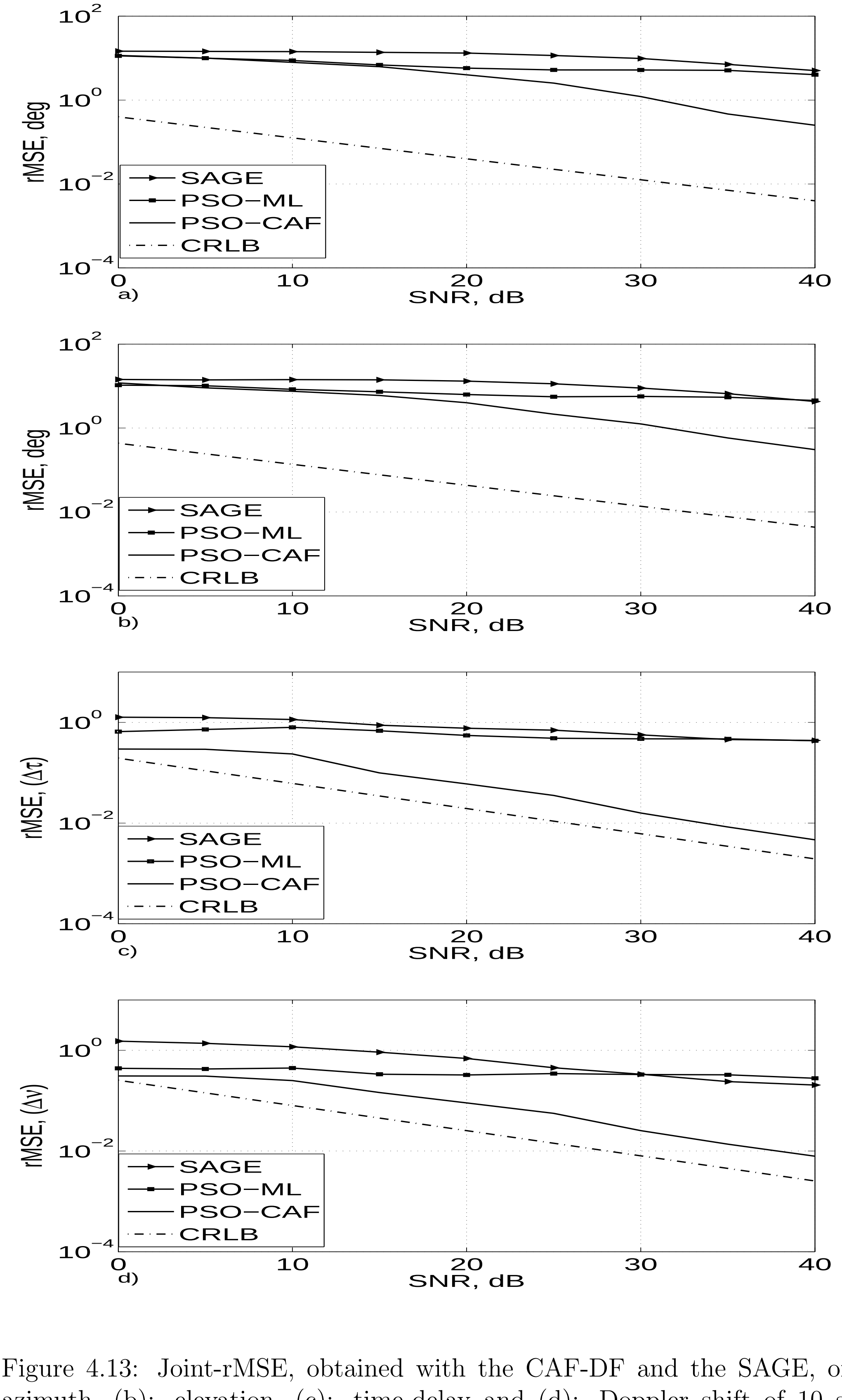

Figure 4.13: Joint-rMSE, obtained with the CAF-DF and the SAGE, of (a): azimuth, (b): elevation, (c): time-delay and (d): Doppler shift of 10 signal paths. Dash-dot line represents the CRLB.

4.4 Conclusions

A new multipath channel parameter estimation technique called the PSO-CAF, is proposed. PSO-CAF transforms the received array outputs to delay-Doppler domain by CAF calculation for efficient exploitation of the delay-Doppler diversity of the multipath signal components. Clusters of multipath components are identified in the delay-Doppler domain. Localization of multipath components to their respective delay and Doppler cells enabled the reformulation of the channel identification problem as a set of loosely coupled optimization problems in lower dimensional parameter spaces. PSO is used to identify parameters of multipath components in each cluster. Simulation results show that the PSO-CAF provides significantly better parameter estimates than the SAGE and recently proposed PSO-ML technique.

Chapter 5

Multipath Channel Identification Techniques by Using Compressed Sensing Theory

5.1 Introduction

A general assumption in research for wireless multipath channel identification is that there exist rich multipath environment, and the linear reconstruction techniques are optimal in these channels. Nevertheless, recent studies revealed the fact that the wireless channels have a sparse structure in time, frequency and space. Additionally, it has been proven that the linear reconstruction techniques cannot fully exploit the sparse structure of the channel and produce non-sparse multipath structures. In order to better model sparse multipath channels, new techniques that have better performance than usual least-squared based approaches are proposed within the context of newly developed CS theory. However, the CS based approaches assume that the parameters of all multipath components fall on a standard grid, which is practically impossible as the channel parameters can assume any value in a wide range. Performances of these techniques based on discretization of the multipath channel parameter space degrade significantly when the actual channel parameters deviate from the assumed discrete set of values. This problem is called the off-grid problem and results in a mismatch of the dictionary and severely degrades the performance.

In this chapter, we present the details of a novel algorithm to overcome the so called off-grid problem [64], [65]. In order to exploit the delay-Doppler diversity of the multipath components, the proposed technique transform receiver output to delay-Doppler domain by using cross ambiguity function calculation. After that, multipath clusters are determined on the delay-Doppler domain by a simple thresholding to formulize the original channel identification problem in reduced channel identification problems. Having determined the locations of multipath clusters, on-grid points that reside in each cluster are perturbed by using PSO and multipath components are recovered by using the orthogonal matching pursuit (OMP) algorithm.

5.2 Compressed Sensing Theory

The main purpose of sampling or sensing is to accurately capture the significant information in a recorded signal of interest by taking as few samples as possible. The question at this point is: *in order to perfectly recover the original signal, what is the required number of samples?*. For bandlimited signals, the Nyquist-Shannon sampling theorem, which is a fundamental tenet in information theory and modern telecommunication, gives an answer to this crucial question: *"when converting an analog signal, which is bandlimited to BW Hz, to a discrete signal, the sampling rate should be greater than BW samples per second in order to be able to reconstruct the original signal perfectly from its samples"* [101],[102]. This fundamental theorem, gives a sufficient but not a necessary condition for perfect reconstruction. The relatively new theory of compressed sensing (CS), provides a stricter sampling condition when the interested signal has a sparse structure [103],[104],[105],[106]. Different from the Nyquist-Shannon sampling theorem, in CS, signals are assumed to be sparse in different transform domains, not necessarily the Fourier transform. CS theory, introduces new sampling schemes that enable us to uniquely represent the original sparse signal with low number of required samples. Contrary to traditional techniques that employ oversampling and then apply compression, new techniques based on CS theory have lower computational complexities by achieving compression at the same time with sampling.

In order to motive the theoretical idea behind the CS, we begin with the following model:

$$\mathbf{v} = \boldsymbol{\Upsilon}\boldsymbol{\alpha} \quad , \tag{5.1}$$

where $\mathbf{v} \in \mathbb{C}^N$ is the discrete signal in time domain which has to be undersampled, $\boldsymbol{\Upsilon} \in \mathbb{C}^{N\times N}$ is the transform domain matrix and $\boldsymbol{\alpha} \in \mathbb{C}^N$ is the $\mathcal{S}$-sparse ($\|\boldsymbol{\alpha}\|_0 \leq \mathcal{S}$) vector with suppot set $\Lambda_{\mathcal{S}} = \text{supp}(\boldsymbol{\alpha})$. In practical scenarios, insignificant elements of $\boldsymbol{\alpha}$ are set to zero and $\mathcal{S}$ most significant elements are taken account. To illustrate this approach, let $\mathbf{v}$ be the pixels of an image and $\boldsymbol{\Upsilon}$ be the inverse discrete cosine transform matrix (IDCT). For images it is known that, most of the DCT coefficients can be set to zero with no perceptible degradation in image quality. Actually, this is the main idea behind the famous JPEG-2000 compression technique. This approach efficiently compresses $\mathbf{v}$. However, at first, to produce $\boldsymbol{\alpha}$, it requires all samples of $\mathbf{v}$. In this situation, the CS theory provides an alternative reconstruction technique [107].

Assume that, instead of directly using samples of $\mathbf{v}$, take M ($M << N$) linear combinations of samples. These linear combinations can be represented with the matrix $\mathbf{\Phi} \in \mathbb{C}^{M \times N}$ and new model can be written as:

$$\begin{aligned} \mathbf{\Phi v} &= \mathbf{\Phi \Upsilon} \boldsymbol{\alpha} \\ \mathbf{x} &= \mathbf{\Psi} \boldsymbol{\alpha} \quad , \end{aligned} \tag{5.2}$$

where $\mathbf{x} \in \mathbb{C}^{M}$ can be termed as the observation or measurement vector and $\mathbf{\Psi} \in \mathbb{C}^{M \times N}$ is the sensing matrix. Here we are looking for a matrix $\mathbf{\Psi}$, which has as few rows as possible and can guarantee recovery of a sparse input.

Our aim is to reliably recover $\boldsymbol{\alpha}$ from knowledge of $\mathbf{x}$ and $\mathbf{\Psi}$. However, the dictionary matrix $\mathbf{\Psi}$ consists of more columns, called as atoms, than rows. Therefore, in the absence of further prior information, $\boldsymbol{\alpha}$ is unidentifiable from $\mathbf{x}$. This problem can be resolved by regularizing via sparsity constraints. That is, we search for approximate solutions to linear systems in which the unknown vector has few nonzero entries relative to its dimension:

$$\text{Find sparse } \boldsymbol{\alpha} \qquad \text{s.t. } \mathbf{x} \approx \mathbf{\Psi} \boldsymbol{\alpha} \quad . \tag{5.3}$$

In literature, this formulation is known as sparse approximation [108]. In a nutshell, the CS theory, also referred to as sparse approximation theory, tries to produce answers to the following questions to reliably recover $\boldsymbol{\alpha}$ from knowledge of $\mathbf{x}$ and $\mathbf{\Psi}$:

- Which conditions should dictionary matrix $\mathbf{\Psi}$ satisfy?
- How can we design efficient algorithms for a given class of dictionaries that provably recover a nearly optimal sparse representation of an arbitrary input signal?
- What recovery guarantees can be provided for different algorithms under different conditions?

These questions are successfully addressed in a number of work up to now and extensive research is going on the theory and applications of CS [109],[110],[111], [112],[63].

5.2.1 Requirements on the Dictionary

In order to reliably recover $\boldsymbol{\alpha}$, we must have a guarantee notifying that different values of $\boldsymbol{\alpha}$ produce different values of $\mathbf{x}$. One way of having such a guarantee is determining all possible $\mathcal{S}$-element sets of atoms called subdictionaries and verifying that the subspaces spanned by these subdictionaries differ from each other. There exists several methods that formulize the suitability of a dictionary for sparse approximation. These methods can be itemized as follows:

- The mutual coherence [113]
- The cumulative coherence [114]
- The exact recovery coefficient (ERC) [114]
- The spark [115]
- The restricted isometry constants (RICs). [116]

Mutual and cumulative coherence measures provide close values and they are easy to calculate but suboptimal when the RICs of $\boldsymbol{\Psi}$ are known. However, for arbitrary dictionary $\boldsymbol{\Psi}$, calculation of other three approaches is not efficient. In the following we will shortly clarify what exactly means some of these measures and their relations with each other.

The mutual coherence $\mu = \mu(\boldsymbol{\Psi})$ is defined as:

$$\mu \triangleq \max_{i \neq j} \ |\boldsymbol{\psi}_i^T \boldsymbol{\psi}_j| \ , \tag{5.4}$$

where columns $\boldsymbol{\psi}_i$ of dictionary $\boldsymbol{\Psi}$ are atoms of the dictionary. Assuming that each atom $\|\boldsymbol{\psi}_i\|_2 = 1$, then the coherence is bounded by [117]:

$$\sqrt{\frac{N-M}{M(N-1)}} \leq \mu(\boldsymbol{\Psi}) \leq 1 \ . \tag{5.5}$$

Two atoms are aligned when $\mu(\mathbf{\Psi}) = 1$ and we have the maximal coherence which is the worst case scenario. When $\mu(\mathbf{\Psi}) = \sqrt{(N-M)/M(N-1)}$ we have the maximal incoherence which is the best case scenario. In maximal incoherence scenario, the atoms are spread out in $\mathbb{C}^M$. Although it is very efficient to calculate directly using (5.4), the relation between μ and requirement, which saying the subdictionaries must span different subspaces, is not clear. What we are really interested is that the distinction between $\mathcal{S}$-element dictionaries rather than just the correlation between single atoms. RICs is such a measure that is related to the subdictionaries of dictionary matrix $\mathbf{\Psi}$. However, mutual coherence can be used as an efficient bridge for accurate dictionary quality measures, such as RICs, which are not computationally efficient.

In RICs measure, a dictionary is accepted as good, if it satisfies the restricted isometry property (RIP) and restricted orthogonality property (ROP). We say that the matrix $\mathbf{\Psi}$ satisfies the RIP of order $\mathcal{S}$ with constant $\delta_{\mathcal{S}}$ if for every index set Λ of size $\mathcal{S}$ we have:

$$(1-\delta_{\mathcal{S}})\|\mathbf{b}\|_2^2 \leq \|\mathbf{\Psi}_\Lambda \mathbf{b}\|_2^2 \leq (1+\delta_{\mathcal{S}})\|\mathbf{b}\|_2^2 \quad , \tag{5.6}$$

for all $\mathbf{b} \in \mathbb{R}^{\mathcal{S}}$. Here, if $\delta_{\mathcal{S}}$ is small, the RIP ensures that any $\mathcal{S}$-atom subdictionary is nearly orthogonal. This also implies that any two disjoint $(\mathcal{S}/2)$-atom subdictionaries are well-separated. In a similar fashion, We say that the matrix $\mathbf{\Psi}$ satisfies the ROP of order $(\mathcal{S}_1, \mathcal{S}_2)$ with parameter $\varsigma_{\mathcal{S}_1,\mathcal{S}_2}$ if for every pair of disjoint index sets Λ_1 and Λ_2 having cardinalities $\mathcal{S}_1$ and $\mathcal{S}_2$, respectively, we have

$$|\mathbf{b}_1^T \mathbf{\Psi}_{\Lambda_1}^T \mathbf{\Psi}_{\Lambda_2} \mathbf{b}_2| \leq \varsigma_{\mathcal{S}_1,\mathcal{S}_2} \|\mathbf{b}_1\|_2 \|\mathbf{b}_2\|_2 \quad , \tag{5.7}$$

for all $\mathbf{b}_1 \in \mathbb{R}^{\mathcal{S}_1}$ and for all $\mathbf{b}_2 \in \mathbb{R}^{\mathcal{S}_2}$. Shortly, ROP requires any two disjoint nearly orthogonal subdictionaries that are containing $\mathcal{S}_1$ and $\mathcal{S}_2$ elements respectively.

It has been shown that, if the constant $\delta_{\mathcal{S}}$ and $\varsigma_{\mathcal{S}_1,\mathcal{S}_2}$ sufficiently small, various sparse approximation algorithms can reliably recover $\boldsymbol{\alpha}$ from $\mathbf{x}$ [116], [118].

These important results are valid, when the elements of dictionary $\mathbf{\Psi}$ are independent identically distributed Gaussian random variables or when in some specific deterministic dictionary matrices. However, in most of the practical estimation scenarios, there is no chance to design the so called system matrix $\mathbf{\Psi}$ according to the stated specific rules. Actually, if we are given a particular dictionary matrix $\mathbf{\Psi}$ beforehand, then there exists no known efficient algorithm for determining its RICs. RICs require searching over an exponential number of index sets to find the worst subdictionaries. On the other hand, although mutual coherence μ given in (5.4) is less accurate in finding the accuracy of a dictionary, it is a good tool that enable us to comment on RICs based only on μ. In the following Lemma this point can be noticed [119].

Lemma 1: For any matrix $\mathbf{\Psi}$, the RIP constant $\delta_{\mathcal{S}}$ of (5.6) and the ROP constant $\varsigma_{\mathcal{S}_1,\mathcal{S}_2}$ of (5.7) satisfy the bounds:

$$\delta_{\mathcal{S}} \leq (\mathcal{S}-1)\mu \tag{5.8}$$

$$\varsigma_{\mathcal{S}_1,\mathcal{S}_2} \leq \mu\sqrt{\mathcal{S}_1\mathcal{S}_2} \ , \tag{5.9}$$

where μ is the mutual coherence (5.4). In the following section we will concentrate on some sparse estimation techniques that are very well known in the literature and have well studied performance guarantees.

5.2.2 Sparse Estimation Techniques

The system model in (5.3) can be expressed as:

$$\mathbf{x} = \mathbf{\Psi}\boldsymbol{\alpha} + \mathbf{n} \ , \tag{5.10}$$

where $\mathbf{n}$ is the random noise. Based on this model, in the following list we will provide short descriptions of some proposed estimation techniques. After that, we will focus on the first two dominant approaches. There are five major classes of sparse estimation techniques [120]:

- **Convex relaxation:** Combinatorial problem is replaced with a convex optimization problem. Nonconvex constraint $\|\boldsymbol{\alpha}\|_0 = \mathcal{S}$ is relaxed to a constraint on the l_1 norm of the estimated vector $\boldsymbol{\alpha}$ [108].
- **Greedy Pursuit:** Iteratively optimize a sparse approximation by successively identifying one or more components that produce the greatest improvement in the approximation [121].
- **Nonconvex optimization:** Try to identify a stationary point by relaxing the l_0 problem to a related nonconvex problem [122].
- **Brute-force:** Search all the possible support sets [123].
- **Bayesian techniques:** Assume a prior distribution for the unknown coefficients favoring sparsity. A maximum a posteriori estimator incorporating the observation is developed. Then, determine a region of posterior mass [124].

Convex relaxation based and greedy pursuit techniques are the preferred techniques in the rapidly growing literature on CS theory.

The convex relaxation problem can be written as:

$$\min_{\boldsymbol{\alpha}} \frac{1}{2}\|\mathbf{x} - \boldsymbol{\Psi}\boldsymbol{\alpha}\|_2^2 + \gamma\|\boldsymbol{\alpha}\|_1 \quad , \tag{5.11}$$

where γ is a regularization parameter which effects the sparsity of the solution. Typically large values produce sparser solutions. This optimization problem is known as basis pursuit denoising (BPDN) [108],[125]. BPDN is also known as follows in some contexts:

$$\min_{\boldsymbol{\alpha}} \|\boldsymbol{\alpha}\|_1 \quad \text{s.t.} \quad \|\mathbf{x} - \boldsymbol{\Psi}\boldsymbol{\alpha}\|_2^2 \leq \delta \quad , \tag{5.12}$$

where δ is a constant.

Another formulation based on the l_1 relaxation is the Dantzig selector [116]:

$$\min_{\boldsymbol{\alpha}} \|\boldsymbol{\alpha}\|_1 \quad \text{s.t.} \quad \|\boldsymbol{\Psi}^{\mathrm{T}}(\mathbf{x} - \boldsymbol{\Psi}\boldsymbol{\alpha}\|_\infty \leq \beta \quad , \tag{5.13}$$

where β is an user-defined parameter. Similar to BPDN, Dantzig selector is a convex relaxation method. However, different than the BPDN, which penalize the l_2 norm of residual $\mathbf{x} - \boldsymbol{\Psi}\boldsymbol{\alpha}$, the Dantzig selector makes sure that the residual $\mathbf{x} - \boldsymbol{\Psi}\boldsymbol{\alpha}$ is poorly correlated with all the atoms in the dictionary.

Greedy approaches estimate the support set Λ from the measurements $\mathbf{x}$ by iteratively refining the current estimate for the vector $\boldsymbol{\alpha}$ by updating one or several coefficients that yield a considerable improvement in approximating the signal. Having found a support set Λ, $\boldsymbol{\alpha}$ can be estimated by using least-squares (LS) as:

$$\hat{\boldsymbol{\alpha}} = \boldsymbol{\Psi}_{\Lambda}^{\dagger}\mathbf{x} \quad , \tag{5.14}$$

and $\mathbf{0}$ elsewhere. Greedy techniques differ from each other in selecting the support set. Thresholding algorithm, which is the simplest one, computes correlation of $\mathbf{x}$ with each atom in the dictionary and determines a support set Λ with indices of the $\mathcal{S}$ atoms having the highest correlation. After that, (5.14) is used to get the thresholding estimate of $\boldsymbol{\alpha}$.

Another very effective greedy algorithm is the orthogonal matching pursuit (OMP) [66]. Table. 5.1, contains a mathematical flow of the OMP. Computationally most costly part of the OMP is the identification step [120] which requires $O(M \times N)$ number of multiplications for an unstructured dense matrix. LS technique is used in the reconstruction step. For this purpose, QR factorization of $\boldsymbol{\Psi}_{\Lambda_k}$, which has a cost of $O(Mk)$ in the k^{th} iteration, can be used. To stop the algorithm, following listed criteria can be used:

- stop after a fixed number of iterations, $k = \mathcal{S}$,
- stop when the residual has a small enough magnitude, $\|\mathbf{r}_k\|_2 \leq \epsilon$.

Most important property of the OMP is that the algorithm never chooses the same atom twice [115]. Therefore, stopping after $\mathcal{S}$ iterations guarantees the

$\|\hat{\boldsymbol{\alpha}}\|_0 = \mathcal{S}$. Many different greedy pursuit based algorithms have been proposed in the literature [121],[126], [127], [128].

Table 5.1: Orthogonal Matching Pursuit (OMP)

- **Input:** $\mathbf{x} \in \mathbb{C}^M$ and $\boldsymbol{\Psi} \in \mathbb{C}^{M \times N}$
- **Output:** sparse vector $\boldsymbol{\alpha} \in \mathbb{C}^N$

1) **Initialization:** set $\Lambda_0 = \emptyset$, the residual $\mathbf{r}_0 = \mathbf{x}$ and set counter $k = 1$
2) **Determination:** find a atom n_k of $\boldsymbol{\Psi}$, which is most strongly correlated with the residual $\mathbf{r}$ as

$$n_k \quad = \quad \arg\max_{\mathrm{n}} \quad |\langle \mathbf{r}_{\mathrm{k}-1}, \boldsymbol{\psi}_{\mathrm{n}} \rangle|$$
$$\Lambda_k = \Lambda_{k-1} \bigcup \{n_k\}$$

3) **Estimation:** using the chosen atoms up to now, find the best coefficients for approximating the signal.

$$\alpha_k = \arg\min_{\mathbf{b}} \quad \|\mathbf{x} - \boldsymbol{\Psi}_{\Lambda_\mathrm{k}} \mathbf{b}\|_2$$

4) **Iteration:** update the residual:

$$\mathbf{r}_k = \mathbf{x} - \boldsymbol{\Psi}_{\Lambda_k} \alpha_k$$
$$k = k + 1$$

repeat $2) - 4)$

5) **Output:** return the vector $\boldsymbol{\alpha}$ with components $\alpha(n) = \alpha_k(n)$ for $n \in \Lambda_k$ and $\alpha(n) = 0$ otherwise.

Lastly, it would be very beneficial to mention so called *oracle estimator* that is based on the known support set Λ_o and on the $\mathbf{x}$. In this approach, Λ_o is assumed to have been given by an oracle. Then the optimal estimate for $\boldsymbol{\alpha}$ is obtained by:

$$\hat{\boldsymbol{\alpha}}_o = \boldsymbol{\Psi}^{\dagger}_{\Lambda_o} \mathbf{x} \quad , \tag{5.15}$$

and $\mathbf{0}$ on the complement of Λ_o. Here, Λ_o is the support set of oracle estimator and $\boldsymbol{\Psi}_{\Lambda_o}$ is the subdictionary obtained from the columns of $\boldsymbol{\Psi}$ corresponding to nonzero entries of $\boldsymbol{\alpha}$. Oracle estimator is the LS solution among all other vectors, whose support coincides with the support of oracle. In practice, Λ_o is unknown, therefore $\hat{\boldsymbol{\alpha}}_o$ cannot be calculated. However, for the purpose of performance comparison, one can use $\hat{\boldsymbol{\alpha}}_o$, whose mean-squared error (MSE) is [116]:

$$\sigma^2 \mathrm{Tr}((\boldsymbol{\Psi}^{\mathrm{T}}_{\Lambda_\mathrm{o}} \boldsymbol{\Psi}_{\Lambda_\mathrm{o}})^{-1}) \quad . \tag{5.16}$$

In [129], it is presented that the MSE of oracle estimator equals that of the CRLB.

5.2.3 Sensing Sparse Doubly Selective Multipath Channels

In this section, based on the virtual model presented in section (2.5), we will model the sensing matrix or dictionary matrix. Firt of all, let's write the discrete time representation of the channel output given in 2.43 as:

$$x_n = \sum_{k=0}^{K-1} \sum_{p=-P}^{P} \mathcal{H}(k,p) e^{j2\pi \frac{p}{N_b} n} s_{n-k} \quad n = 0, 1, \ldots, N_b + K - 2 \tag{5.17}$$

where $N_b = TBW$. Let's define a $\check{N}_b = N_b + K - 1$ length sequence of vectors $\mathbf{s}_n \in \mathbb{C}^K$ as:

$$\mathbf{s}_n = [s_n \ \ s_{n-1} \ \ \ldots s_{n-K+1}]^T \quad , \quad n = 0, 1, \ldots, \check{N}_b - 1 \tag{5.18}$$

where $s_\gamma = 0$ for $\gamma \notin (0, 1, 2, \ldots, N_b - 1)$. The $K \times 2(P+1)$ channel matrix $\check{\mathcal{H}}$, each column of which represents the impulse response for a fixed Doppler shift, is defined as

$$\check{\mathcal{H}} = \begin{bmatrix} \mathcal{H}(0,-P) & \ldots & \ldots & \mathcal{H}(0,P) \\ \mathcal{H}(1,-P) & \ldots & \ldots & \mathcal{H}(0,P) \\ \vdots & \ldots & \ldots & \vdots \\ \mathcal{H}(K-1,-P) & \ldots & \ldots & \mathcal{H}(K-1,P) \end{bmatrix} . \tag{5.19}$$

Lastly, let $\boldsymbol{\varrho} \in \mathbb{C}^{2P+1}$ be a $\check{N}_b$-length sequence of phase vectors with elements $w_{N_b} = e^{j2\pi/N_b}$:

$$\boldsymbol{\varrho}_n = \begin{bmatrix} w_{N_b}^{Pn} & w_{N_b}^{(P-1)n} & \ldots & w_{N_b}^{-(P-1)n} & w_{N_b}^{-Pn} \end{bmatrix}^T \tag{5.20}$$

where $n = 0, 1, \ldots, \check{N}_b - 1$. Channel output in (5.17) can be written as follows:

$$\begin{aligned} x_n &= \mathbf{s}_n^T \check{\mathcal{H}} \boldsymbol{\varrho}_n && (5.21) \\ &= (\boldsymbol{\varrho}_n^T \otimes \mathbf{s}_n^T)\mathfrak{h} \quad , \quad n = 0, 1, \ldots, \check{N}_b - 1 && (5.22) \end{aligned}$$

where $\mathfrak{h} = \text{vec}(\check{\mathcal{H}}) \in^{N_h}$ is the channel coefficients vector. In a more compact form, channel system of equations is

$$\mathbf{x} = \boldsymbol{\Psi}\mathfrak{h} \tag{5.23}$$

where $\boldsymbol{\Psi}$ is the $\check{N}_b \times N_h$ sensing matrix:

$$\boldsymbol{\Psi} = \begin{bmatrix} (\boldsymbol{\varrho}_0 \otimes \mathbf{s}_0)^T \\ (\boldsymbol{\varrho}_1 \otimes \mathbf{s}_1)^T \\ \vdots \\ (\boldsymbol{\varrho}_{\check{N}_b-1} \otimes \mathbf{s}_{\check{N}_b-1})^T \end{bmatrix} \quad . \tag{5.24}$$

Sensing matrix $\boldsymbol{\Psi}$ can also be expressed as the concatenation of K blocks each of which are $\check{N}_b \times 2P + 1$ dimensional matrices:

$$\boldsymbol{\Psi} = [\boldsymbol{\Psi}_0 \quad \boldsymbol{\Psi}_1 \quad \ldots \quad \boldsymbol{\Psi}_{K-1}] \quad . \tag{5.25}$$

If we have noise, Eq. (5.23) becomes:

$$\mathbf{x} = \boldsymbol{\Psi}\mathfrak{h} + \mathbf{n} \quad , \tag{5.26}$$

where $\mathbf{n}$ is a zero-mean white Gaussian noise. In the following discussions, $\mathfrak{h}$ is treated as an unknown-deterministic vector.

Linear measurement model in (5.26) contains N_h unknowns and sensing matrix $\boldsymbol{\Psi}$ is a full rank matrix. Therefore, without a prior sparsity assumption, least squares solution of $\mathfrak{h}$ is:

$$\hat{\mathfrak{h}} = (\boldsymbol{\Psi}^H \boldsymbol{\Psi})^{-1} \boldsymbol{\Psi}^H \mathbf{x} \quad . \tag{5.27}$$

This solution is also the maximum likelihood estimate [130]. Clearly, we can write the $\hat{\mathfrak{h}}$ as [89], [119], [116]:

$$\hat{\mathfrak{h}} = \mathfrak{h} + (\boldsymbol{\Psi}^H \boldsymbol{\Psi})^{-1} \boldsymbol{\Psi}^H \mathbf{n} \tag{5.28}$$

and the mean squared error of the LS estimator is bounded by the following equation.

$$\begin{aligned} \mathbb{E}\|\hat{\mathfrak{h}} - \mathfrak{h}\|_2^2 &= \mathbb{E}\|(\boldsymbol{\Psi}^H\boldsymbol{\Psi})^{-1}\boldsymbol{\Psi}^H\mathbf{n}\|_2^2 && (5.29) \\ &= \sigma^2\mathrm{tr}\left((\boldsymbol{\Psi}^H\boldsymbol{\Psi})^{-1}\right) && (5.30) \\ &\geq \sigma^2 N_h \quad . && (5.31) \end{aligned}$$

If we have a prior sparsity information, oracle estimator solution of $\mathfrak{h}$ is:

$$\hat{\mathfrak{h}} = (\boldsymbol{\Psi}_{\Lambda_o}^H\boldsymbol{\Psi}_{\Lambda_o})^{-1}\boldsymbol{\Psi}_{\Lambda_o}^H\mathbf{x} \quad . \tag{5.32}$$

Similarly, the mean squared error of the oracle estimator is bounded by:

$$\begin{aligned} \mathbb{E}\|\hat{\mathfrak{h}} - \mathfrak{h}\|_2^2 &= \sigma^2\mathrm{tr}\left((\boldsymbol{\Psi}_{\Lambda_o}^H\boldsymbol{\Psi}_{\Lambda_o})^{-1}\right) && (5.33) \\ &\geq \sigma^2\mathcal{S} \quad . && (5.34) \end{aligned}$$

If we compare the results presented in 5.31 and 5.34, conventional LS estimator shows poor performance in the identification of sparse multipath channels.

As it is stated before, although constructing an oracle estimator is practically impossible, there exists efficient algorithms that provide much more better estimates than the conventional LS estimator and have proven performance guarantees in sparse multipath channels. In the following, we will give two theorems that quantify the MSE upper bounds for Dantzig selector and OMP techniques, respectively.

Theorem 1 ([116], [119]): Assume that $\mathfrak{h}$ is an unknown deterministic vector with $\|\alpha\| = \mathcal{S}$ and $\mathbf{x} = \boldsymbol{\Psi}\mathfrak{h}$ where $\mathbf{n}$ is a Gaussian random vector with mean 0 and covariance $\sigma^2\mathbf{I}$. Assume that

$$\mathcal{S} < 1 + \frac{1}{\mu(\Psi)(1+\sqrt{2})} \tag{5.35}$$

and the user defined parameter of the Dantzig selector (5.13) is

$$\beta = \sigma\sqrt{2(1+\varepsilon)\mathrm{log}N_h} \tag{5.36}$$

for some constant $\varepsilon > 0$. Then, with probability exceeding

$$1 - \frac{1}{N_h^{\varepsilon}\sqrt{\pi \log N_h}} \quad , \tag{5.37}$$

the obtained solution $\hat{\mathfrak{h}}$ satisfies

$$\|\hat{\mathfrak{h}} - \mathfrak{h}\|_2^2 \leq 2\rho^2(1+\varepsilon)\mathcal{S}\sigma^2 \log N_h \quad , \tag{5.38}$$

where ρ is given by:

$$\rho = \frac{4}{1 - \mu(\Psi)((1+\sqrt{2})\mathcal{S} - 1)} \quad . \tag{5.39}$$

$\square$

Although, the solution given by Dantzig selector cannot reach the oracle estimator, with very high probability it gives MSE within $2\rho^2(1+\varepsilon)\log N_h$ multiplied by the MSE bound of oracle estimator given in (5.34).

Now, we provide error bounds for the greedy algorithm OMP.

Theorem 2 [119]: Assume that $\mathfrak{h}$ is an unknown deterministic vector with $\|\alpha\| = \mathcal{S}$ and $\mathbf{x} = \mathbf{\Psi}\mathfrak{h}$ where $\mathbf{n}$ is a Gaussian random vector with mean 0 and covariance $\sigma^2\mathbf{I}$. Define

$$|\mathfrak{h}_{min}| = \min_{i \in \Lambda_o} |\mathfrak{h}_i| \quad , \tag{5.40}$$

$$|\mathfrak{h}_{max}| = \max_{i \in \Lambda_o} |\mathfrak{h}_i| \quad . \tag{5.41}$$

Assume that

$$2\sigma\sqrt{2(1+\varepsilon)\log N_h} \leq |\mathfrak{h}_{min}| - (2\mathcal{S} - 1)\mu(\mathbf{\Psi})|\mathfrak{h}_{min}| \quad , \tag{5.42}$$

for some constant $\varepsilon > 0$. Then with probability exceeding

$$1 - \frac{1}{N_h^{\varepsilon}\sqrt{\pi(1+\varepsilon)\log N_h}} \tag{5.43}$$

the obtained solution $\hat{\mathfrak{h}}$ of the OMP satisfies

$$\|\hat{\mathfrak{h}} - \mathfrak{h}\|_2^2 \leq \frac{2(1+\varepsilon)}{(1 - (\mathcal{S} - 1)\mu(\mathbf{\Psi}))^2}\mathcal{S}\sigma^2 \log N_h \quad . \tag{5.44}$$

$\square$

The MSE guarantee given in (5.44) is better than the one given in Theorem-1. Analysis given in the literature suggest that the OMP can outperform l_1-based techniques when the entries of $\mathfrak{h}$ are large compared with noise. However, when the noise level increases, the performance of the OMP deteriorates [119]. Moreover, we provide another theorem which gives the relation between sparsity level and coherency for guaranteed recovery.

Theorem 3 [131]: For a general dictionary Ψ, every $\mathcal{S}$-sparse signal $\mathfrak{h}$ with

$$\mathcal{S} < \frac{1}{2}\left(\frac{1}{\mu(\Psi)} + 1\right), \tag{5.45}$$

is the unique sparsest representation and is guaranteed to be recovered by OMP when observing

$$\mathbf{x} = \boldsymbol{\Psi}\boldsymbol{\mathfrak{h}}. \tag{5.46}$$

As we noticed before, coherency of a dictionary is crucial in representing known data. Atoms in the dictionary should not resemble each other. Namely, the sequence which is used to construct the dictionary should have good incoherency properties and constructed dictionary should have a coherency value close to the lower bound given in (5.5). In the last part of this section, we will present a candidate channel probing sequence called Alltop sequences, which enable us to construct dictionaries with very good incoherence properties [132]. Alltop sequences have been used effectively in several different areas [133], [134]. For some prime number $\check{N}_b \geq 5$, Alltop sequence, $\mathbf{s}_A = (s_b)_{b=0}^{\check{N}_b - 1}$, has the following elements

$$s_b = \frac{1}{\sqrt{\check{N}_b}} e^{2\pi j b^3/\check{N}_b} \quad . \tag{5.47}$$

Considering that the $\|\mathbf{s}_A\|_2 = 1$ and the dictionary structure in (5.25), within the same block we have the following property:

$$\left\|\langle \psi_{k,i}, \psi_{k,i'}\rangle\right\| = 0, \quad \text{if } i \neq i' \tag{5.48}$$

$$\left\|\langle \psi_{k,i}, \psi_{k,i'}\rangle\right\| = 1, \quad \text{if } i = i' \tag{5.49}$$

For different blocks, $k \neq k^{'}$, we have the following property:

$$\left\| \langle \psi_{k,i}, \psi_{k^{'},i^{'}} \rangle \right\| = \frac{1}{\sqrt{\check{N}_b}} \quad , \tag{5.50}$$

for all $i, i^{'} = 0, \ldots, K-1$. In order to emphasize this desirable feature of Alltop sequences, assume that there exists the same number of delay and Doppler bins as $\check{N}_b$ and the resulting dictionary is $\mathbf{\Psi} \in \mathbb{C}^{\check{N}_b \times \check{N}_b^2}$. By using (5.5) we know that the lower coherency bound is $\frac{1}{\sqrt{\check{N}_b+1}}$. Therefore, using Alltop sequences and for large values of $\check{N}_b$, it is clearly seen that this bound can be practically achieved.

5.3 Off-Grid Problem in Sparse Signal Recovery

Using the theory of CS and sparse approximation theory, new training based techniques have been proposed for sparse multipath channels. These techniques exploit the sparse structure of the multipath channel and provide much better performance than the least-squared based approaches [55], [57]. By using virtual representation of physical multipath channels, the time frequency response of sparse multipath communication channels are modeled and performance of some sparse approximation techniques are discussed [55], [54]. In [56], [57], matrix identification problem, where the matrix has a sparse representation in some basis, is investigated. Compressed sensing radar providing much better time frequency resolutions over classical radar by exploiting the sparse structure is introduced in [57].

General assumption used in all of these sparse multipath/target detection techniques is that all of the multipath components fall on the discrete grid points. Dictionary matrix $\mathbf{\Psi}$ is typically constructed based on the assumption of all the possible multipath components are on-grid points. In other words, each atom in the dictionary corresponds to a signal created with a delay-Doppler pair, which

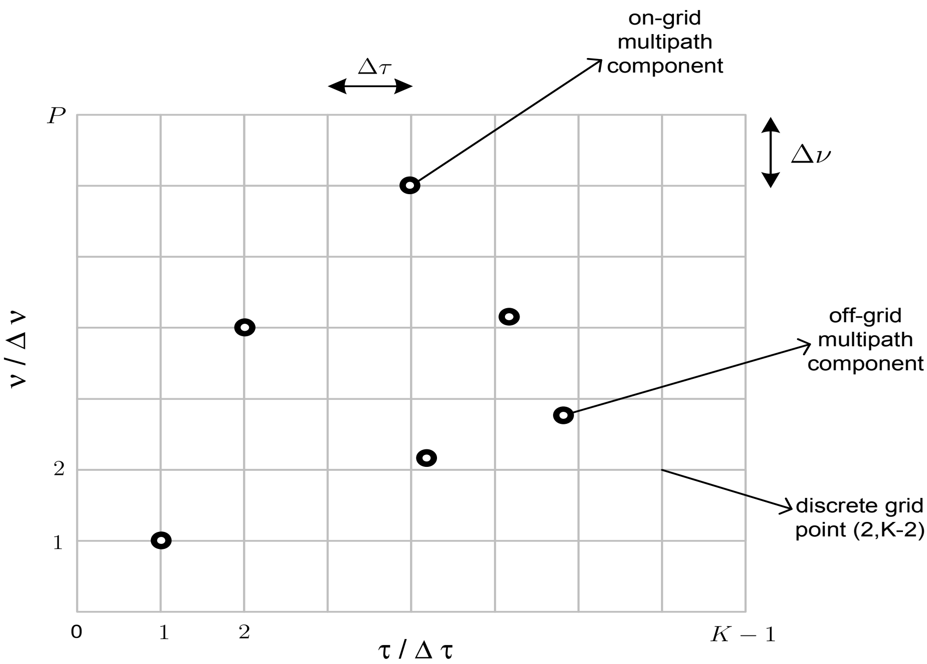

Figure 5.1: On-grid and off-grid multipath components on delay-Doppler domain.

fall onto a discrete grid point. However, this situation is practically impossible as the multipath parameters are unknown. In Fig. 5.1, multipath components that fall on the discrete grid and off-grid points are illustrated. Therefore, the true grid, which is possibly irregular, cannot be known beforehand. This so called off-grid problem, results in a mismatch of the dictionary and severely degrades the performance of techniques that exploit sparsity. If there exists off-grid multipath components, then we won't be able to represent the received signal by using the dictionary $\mathbf{\Psi}$ which is created based on the on-grid assumption. Furthermore, such methods exhibit an unstable behavior as previously shown in theoretical studies on dictionary errors. Therefore, atoms of the dictionary $\mathbf{\Psi}$ should be properly modified to sparsely represent the receiver output. In several papers, the problem is pointed out and very simple grid refinement approaches are presented [62], [63]. In the vicinity of the multipath components grid is iteratively refined to match with the exact location of the off-grid component. The major drawbacks of these approaches are that this grid refinement is a costly procedure and secondly addition of new atoms to the dictionary adversely affects the recovery guarantees. Therefore, to the best of our knowledge, there exist no viable solution to the off-grid problem in the existing literature up to now.

Negative effects of the off-grid problem can be verified on a four-path scenario. In this scenario we used length 53 Alltop sequence and OMP as a recovery technique. In Fig. 5.2, all on-grid multipath components are recovered. However, as in Fig. 5.3, if we perturb the delay-Doppler location of each multipath component in the vicinity of the on-grid point, OMP fails to recover the two paths and makes estimation error in recovery of other two paths. As we pointed out, this result is due to the fact that there exist no atom in the dictionary corresponding to the off-grid multipath components. Detailed simulation results on off-grid problem will be provided in section 5.5.

In the next section, details of the proposed technique to alleviate the off-grid problem by using particle swarm optimization and OMP will be presented.

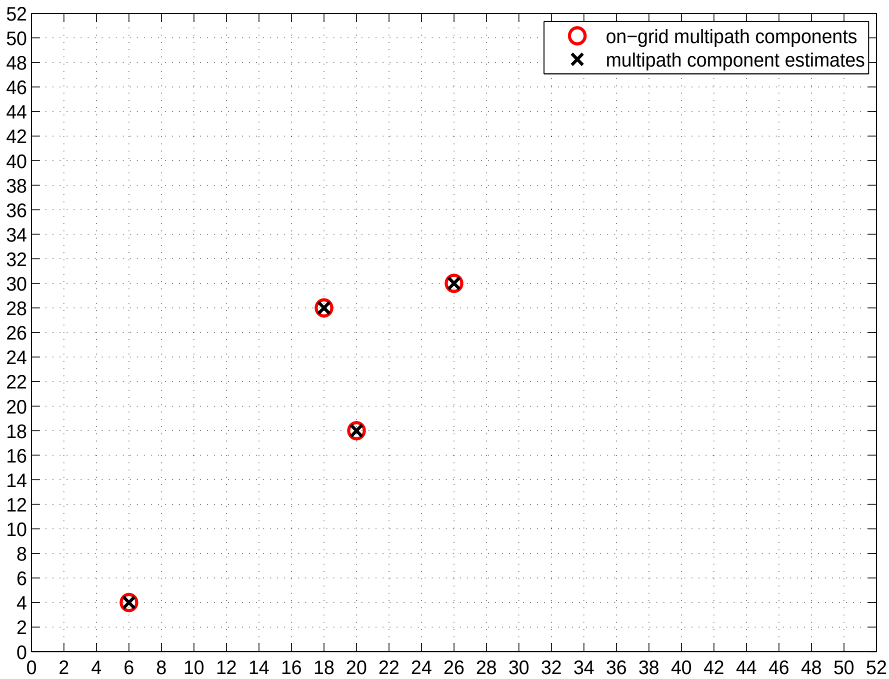

Figure 5.2: True on-grid and estimated position of each multipath component is illustrated with red circles and black crosses, respectively.

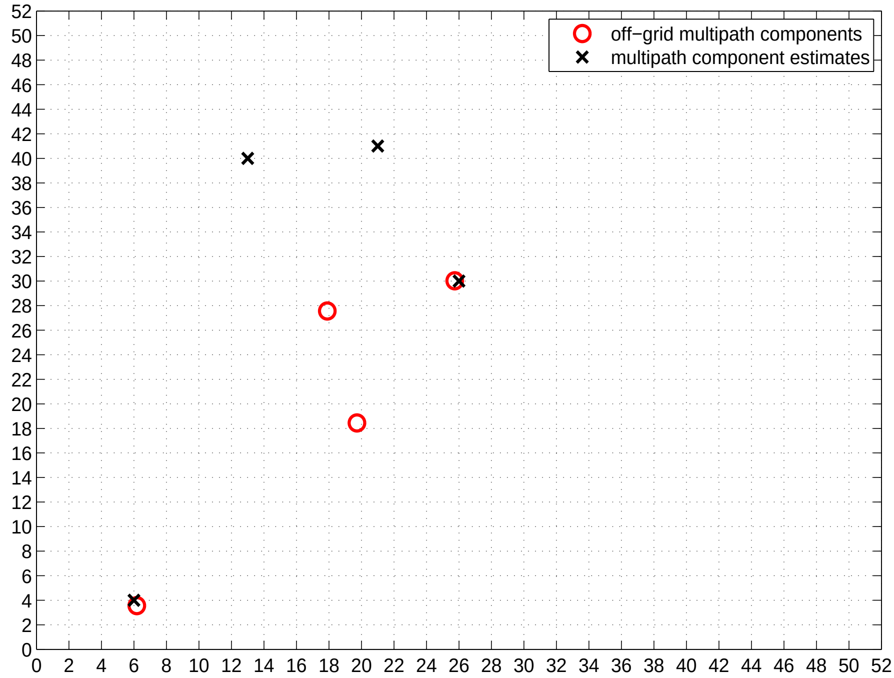

Figure 5.3: True off-grid and estimated position of each multipath component is illustrated with red circles and black crosses, respectively.

5.4 Sparse Approximation on Cross Ambiguity Function Surface

In this section, we will propose a novel technique to overcome the so called off-grid problem in sparse multipath channel modeling. In a multipath environment, as given in Eq. (2.43) the receiver output signal is the superposition of delayed, Doppler-shifted and scaled versions of the transmitted signal. In time domain, there exists a considerable overlap between the signals received from different paths. Therefore, similar to the process discussed in Chapter-4 it is desirable to have a preprocessing, transforming the receiver output signals, that enables localization the multipath signal components and reduction of the significant overlapping of components in the time domain. Since typical communication signals are phase or frequency modulated, with large time-bandwidth products, as in radar detection their CAFs are highly localized in the delay-Doppler domain.

Therefore, the transformation of the signal outputs to the CAF domain localizes different multipath signals in clusters to their respective delay and Doppler cell. To detect the existing multipath signals, a constant false alarm criterion rate (CFAR) based adaptive threshold can be set.

Having completed the detection, around each detected delay- Doppler cell, a windowed set of contributing grid points are determined to be perturbed and used for multipath identification. To illustrate this procedure, consider a synthetic multipath channel with 6 distinct multipath components. As shown in Fig. 5.4, the CAF between the received signal and the transmitted signal localizes the contribution of different path components in delay-Doppler domain. This localization enables us to determine corresponding grid points that will be perturbed to be able to detect multipath components that reside on possible off-grid locations.

Signal flow diagram of the proposed approach is presented in Figs. 5.5, 5.6. Note that, here we assume CAF peak detection has provided C clusters of paths in delay-Doppler domain and the number of paths in cluster c is d_c for $1 \leq c \leq C$. For example as shown in Fig. 5.4, 6 paths are localized in $C = 2$ clusters and each cluster consists of 3 paths. Having identified the location of each cluster, individual PSO searches are conducted to perturb the assumed discrete set of values that are in the support of each cluster, separately.

Having obtained the optimized dictionary matrix, OMP is used as a sparse reconstruction method to estimate delay-Doppler parameters of multipaths. Following PSO searches and multipath reconstruction in each cluster, effects of the estimated multipath components are eliminated for a better estimation in the remaining clusters. Since, optimization in each cluster has to be performed multiple times, PSO iterations in each cluster need not to be pursued until convergence

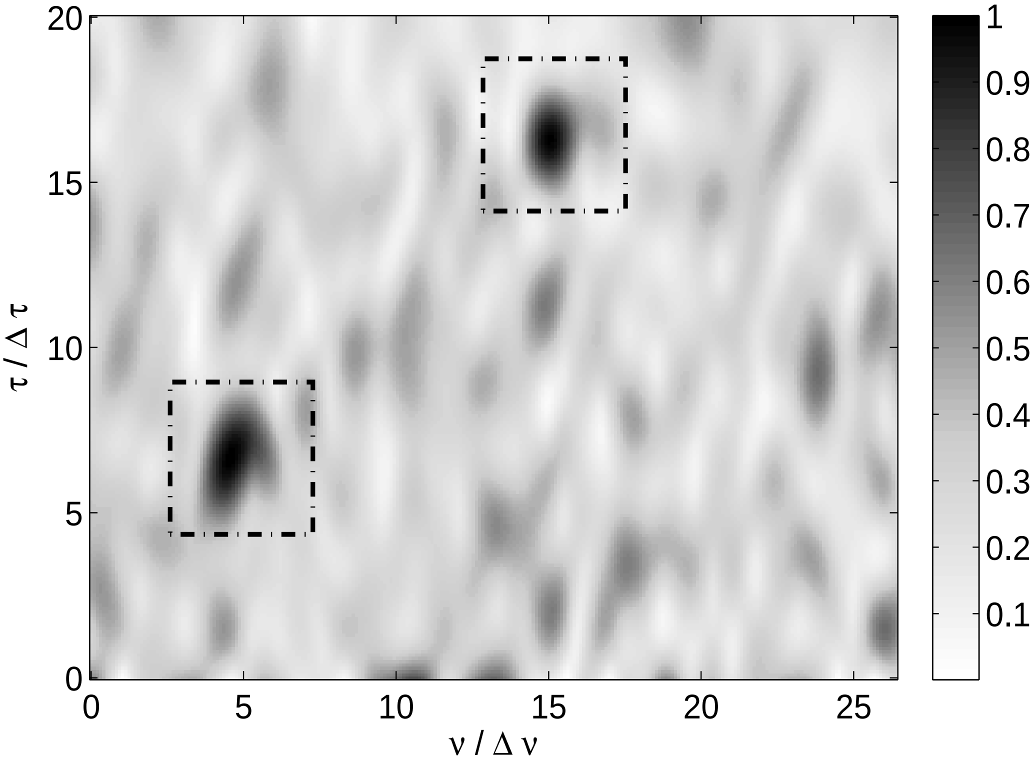

Figure 5.4: 6 Alltop sequences in delay-Doppler domain localized in 2 clusters each of which has 3 paths.

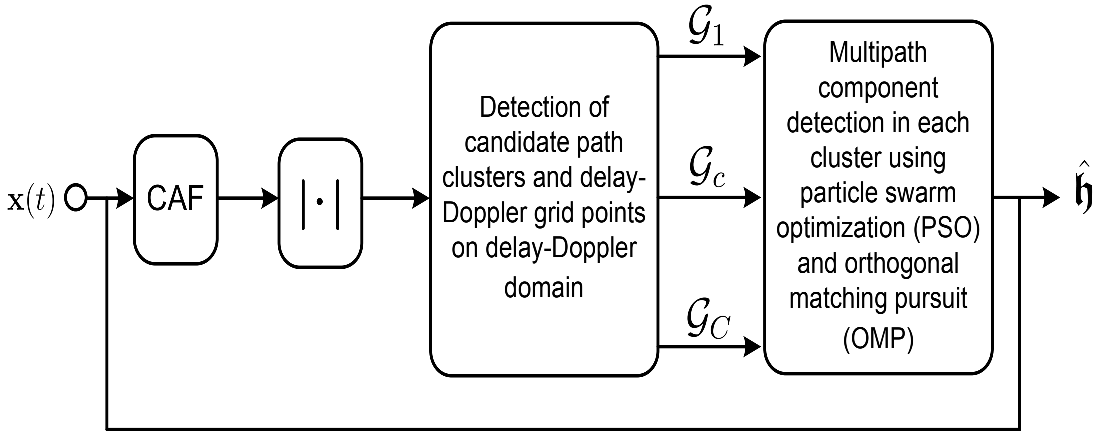

Figure 5.5: Signal flow diagram of the algorithm.

is established. Therefore, by cycling over the identified set of clusters, the proposed technique iteratively provides estimates for each path in each cluster. In the following, details of the proposed technique for each cluster is presented.

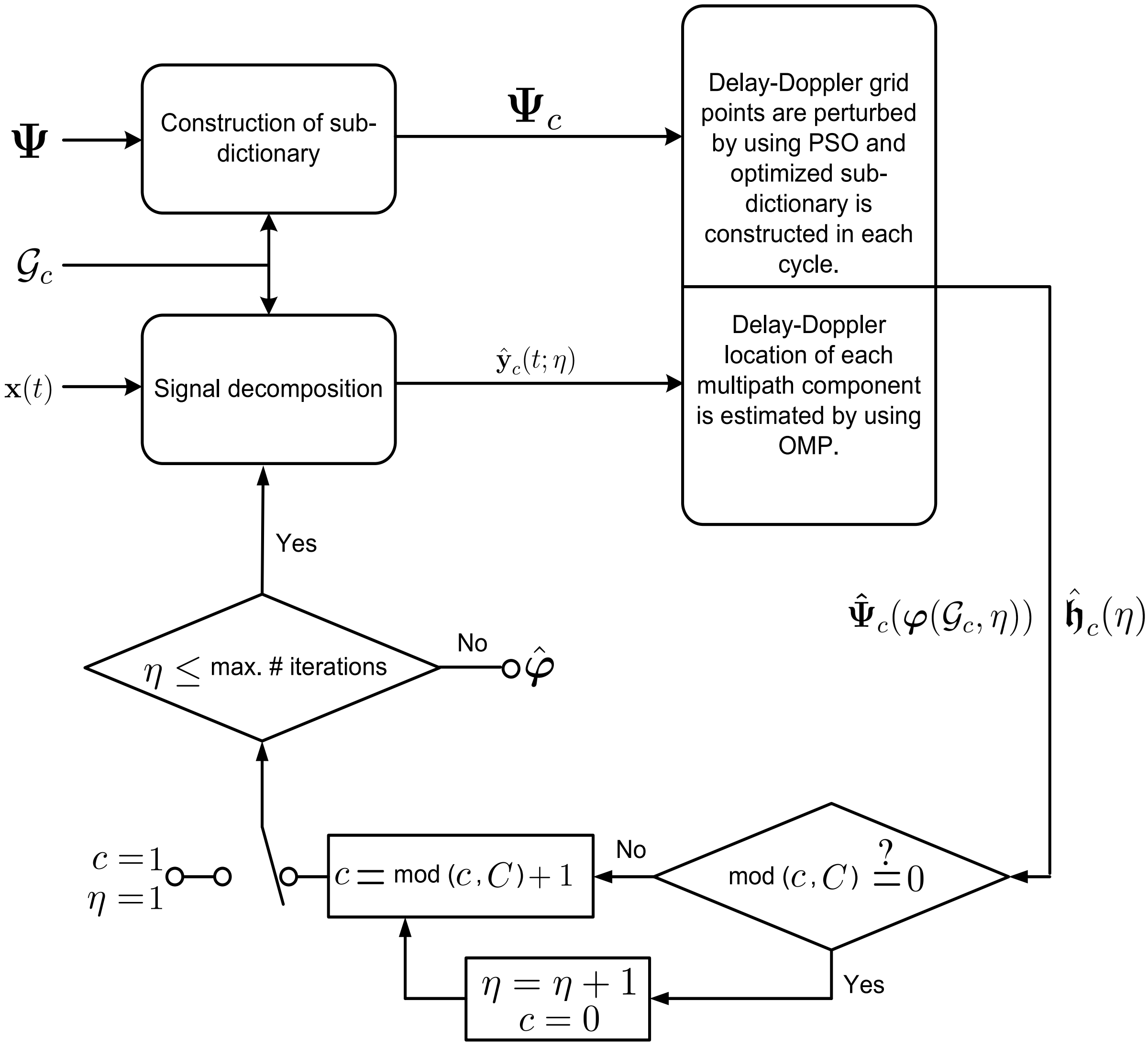

Figure 5.6: Signal flow sub-block diagram of the parameter estimation in each cluster using PSO and OMP block in Fig. 5.5

The optimization problem associated with the c^{th} cluster makes use of the following fitness function:

$$f_c(\mathbf{\Psi}_c(\boldsymbol{\varphi}(\mathcal{G}_c),\eta),\mathfrak{h}_\eta) = \|\hat{\mathbf{y}}_c(t,\eta) - \mathbf{\Psi}_c(\boldsymbol{\varphi}(\mathcal{G}_c),\eta)\mathfrak{h}_c(\eta)\|_2^2 \quad , \tag{5.51}$$

where η represents the iteration index, $\boldsymbol{\varphi} \in \mathbb{R}^{N^2}$ is the vector containing all possible discrete delay-Doppler values:

$$\boldsymbol{\varphi} = [\varphi_{11}, ..., \varphi_{1N}, \varphi_{21}, ..., \varphi_{NN}] \quad , \tag{5.52}$$

$\varphi_{1N} = [\tau_1, \nu_N]$, $\mathcal{G}_c$ is the set containing index of grid points (each grid point corresponds to a delay-Doppler value pair) inside the c^{th} cluster, $\hat{\mathbf{y}}_c(t,\eta)$ is the

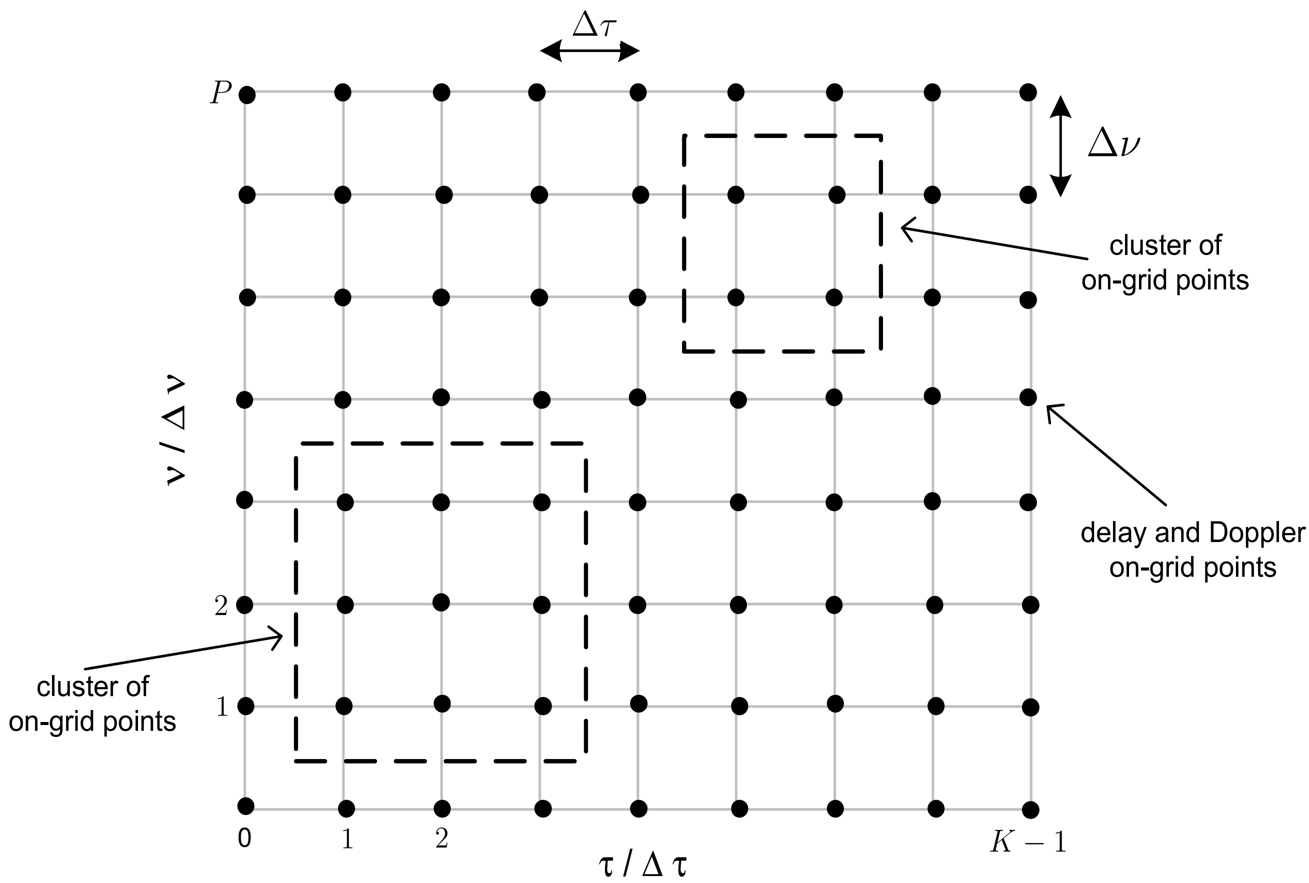

Figure 5.7: Equally spaced $P+1 \times K$ discrete on-grid points on delay-Doppler domain. 2 clusters of on-grid points are selected.

estimated output signal and $\boldsymbol{\Psi}_c$ is the sub-dictionary created using the columns of dictionary matrix $\boldsymbol{\Psi}$ that are in the set Λ_c which contains column index of vectors of $\boldsymbol{\Psi}$, that are in support of cluster c:

$$\boldsymbol{\Psi}_c = (\boldsymbol{\psi}_i : i \in \Lambda_c) \tag{5.53}$$

In Fig. 5.7, two clusters of on-grid points are shown. For each cluster, during PSO cycles, location of these grid points are changed to update the corresponding atoms that belong to the cluster. With these definitions, $\boldsymbol{\varphi}(\mathcal{G}_c)$ holds the delay-Doppler pairs that will be perturbed and $\boldsymbol{\Psi}_c(\boldsymbol{\varphi}(\mathcal{G}_c), \eta)$ holds the vectors that are created with these perturbed delay-Doppler pairs during the PSO cycles at η^{th} iteration. Estimated output signal $\hat{\mathbf{y}}_\eta$ is found as:

$$\hat{\mathbf{y}}_c(t;\eta) = \mathbf{x}(t) - \sum_{\gamma=1,\gamma\neq c}^{C} \hat{\boldsymbol{\Psi}}_\gamma(\boldsymbol{\varphi}(\mathcal{G}_\gamma, \eta))\hat{\mathfrak{h}}_c(\eta) \quad . \tag{5.54}$$

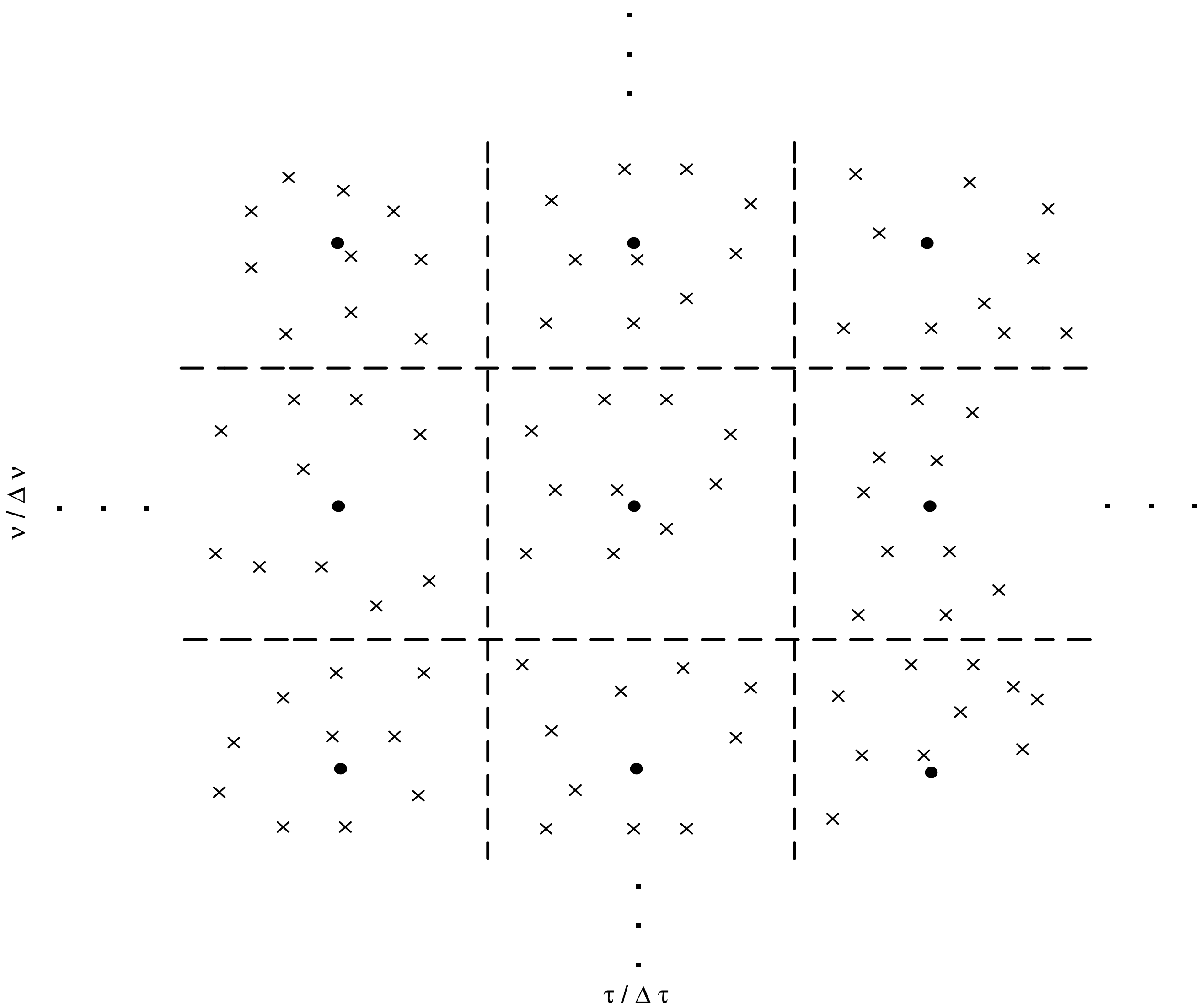

Figure 5.8: On-grid points that reside in a cluster are zoomed. Boundaries around each on-grid point is marked with dash lines. Crosses represent particles. In each boundary same amount of particles exist.

In the first iteration, $\eta = 1$, for the first cluster, $\hat{\mathbf{y}}_c(t;\eta)$ is initialized as $\hat{\mathbf{y}}_c(t;\eta) = \mathbf{x}(t)$. Thus, the channel parameter estimates and proper sub-dictionary to represent off-grid multipaths for the c^{th} cluster at η^{th} iteration are obtained by minimizing the following optimization problem:

$$\hat{\boldsymbol{\Psi}}_c(\boldsymbol{\varphi}(\mathcal{G}_c,\eta)), \hat{\mathfrak{h}}_c(\eta) = \arg \min_{\boldsymbol{\Psi}_c, \mathfrak{h}_c} \; f_c(\boldsymbol{\Psi}_c(\boldsymbol{\varphi}(\mathcal{G}_c),\eta), \mathfrak{h}_c(\eta)) \tag{5.55}$$

Channel parameters and sub-dictionary corresponding to the c^{th} cluster are estimated using swarm of particles in a $|\mathcal{G}|$-dimensional search space. As shown in

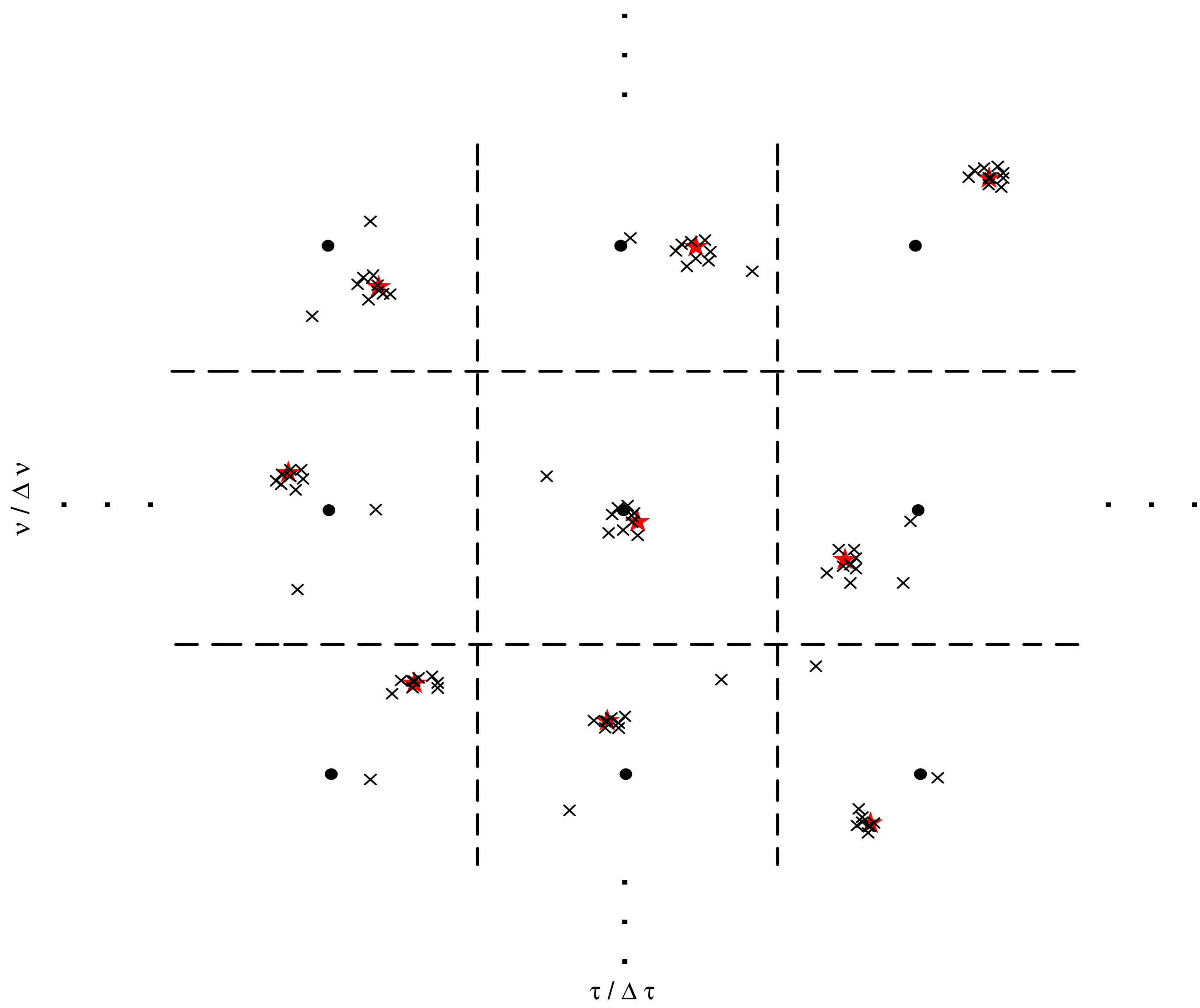

Figure 5.9: One snapshot coordinates of particles $\mathbf{z}, (\times)$ and $\mathbf{globalBest}(\mathbf{p}_g, \star)$ distributed on the delay-Doppler domain. Particles swarm to the **globalBest** position.

Fig. 5.8, at the beginning of the PSO cycles, particle locations (each of which is a solution candidate) are randomly initialized as follows:

$$\mathbf{z}_l = \boldsymbol{\varphi}(\boldsymbol{\mathcal{G}_c}) + \boldsymbol{\mathcal{U}}(-\Delta g/2, \Delta g/2) \tag{5.56}$$

and updated according to Eq. (A.1) in each PSO cycle. Here, $\boldsymbol{\mathcal{U}}$ represents uniform random distribution and Δg is the spacing between discrete grid points. Location, $\mathbf{z}_l \in \mathbb{R}^{|\mathcal{G}|}$, of each particle in the $|\mathcal{G}|$-dimensional search space is a candidate off-grid location solution. Fig. 5.9 illustrates the search of particles

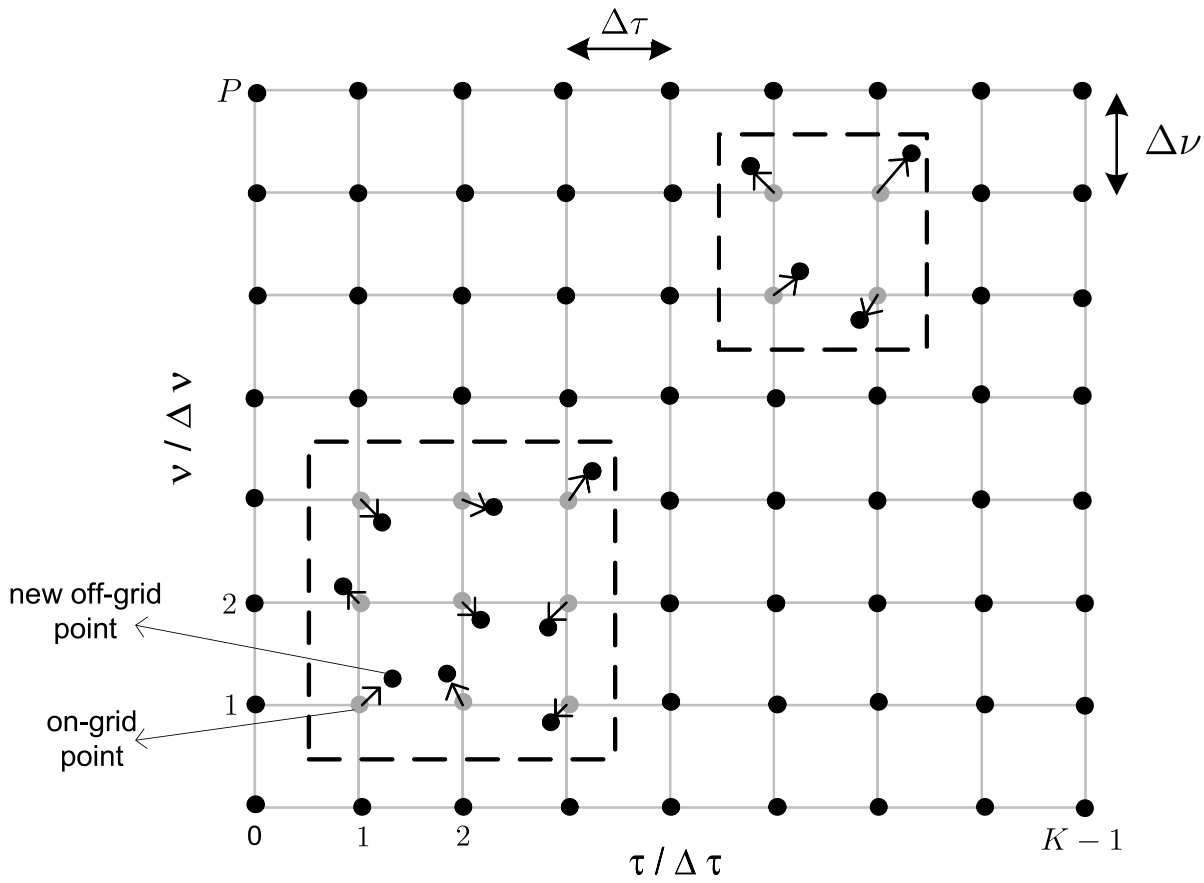

Figure 5.10: Position update of each grid point, that reside in a cluster, to the estimated new off-grid position.

around each discrete grid point and the convergence of particles to a possible solution. In each PSO cycle, following linear system of equation:

$$\hat{\mathbf{y}}_c(t;\eta) \approx \hat{\mathbf{\Psi}}_c(\boldsymbol{\varphi}(\mathcal{G}_c,\eta))\ \mathfrak{h}_c(\eta) \quad , \tag{5.57}$$

is solved using the OMP in a greedy fashion and very efficiently by minimizing

$$\left\| \hat{\mathbf{y}}_c(t;\eta) - \hat{\mathbf{\Psi}}_c(\boldsymbol{\varphi}(\mathcal{G}_c,\eta))\mathfrak{h}_c(\eta) \right\|_2^2 \quad , \tag{5.58}$$

in order to compare the performance of each particle. Equation (5.55) is evaluated using the location values of each particle and the location that gives the best fitness chosen as the **globalBest**. In Fig. 5.10, it is shown that, in the end of PSO cycles, initial on-grid points are updated based on the minimization results and new off-grid points are estimated to better support existing off-grid multipath components. Having estimated the parameters of each multipath component in the c^{th} cluster, effects of these multipath components are eliminated as in (5.54) from the receiver output for a better estimation in remaining clusters. Iterations, η, continue until convergence is established or a preset number of iterations is reached.

5.5 Simulation Results

In this section, we will provide numerical results to clarify the performance gains obtained by exploiting the clustered structure and handling the off-grid problem. In all simulations, length-53 Alltop sequences are used as a probing signal and OMP is used as a sparse recovery technique. 500 Monte Carlo simulations are conducted for each scenario. Number of multipath components, in another words sparsity level $\mathcal{S}$ is changed in between $2-12$. It is assumed that there exist two multipath clusters exists on the delay-Doppler domain. Location of multipath components in two separate clusters on delay-Doppler domain are shown in Fig. 5.11. In each Monte Carlo realization, cluster locations are preserved but multipath component locations are randomly changed.

Firstly, let's observe the effect of off-grid problem in terms of recovery percentage for different sparsity $\mathcal{S} = 2, ..., 12$ and perturbation levels $\kappa = 0, 0.2, 0.3, 0.4, 0.5$. On-grid delay Doppler location of each multipath components is perturbed as follows:

$$\tau_i = \tau_i + \boldsymbol{\mathcal{U}}(-\kappa, \kappa)/\Delta\tau \tag{5.59}$$

$$\nu_i = \nu_i + \boldsymbol{\mathcal{U}}(-\kappa, \kappa)/\Delta\nu \quad . \tag{5.60}$$

Results obtained by OMP are shown in the Fig. 5.12. Note that, for $\mathcal{S} \leq 4$ we have a recovery rate of %100 when all multipath components are on-grid as suggested in Theorem 3. However, when we perturb the delay-Doppler location of

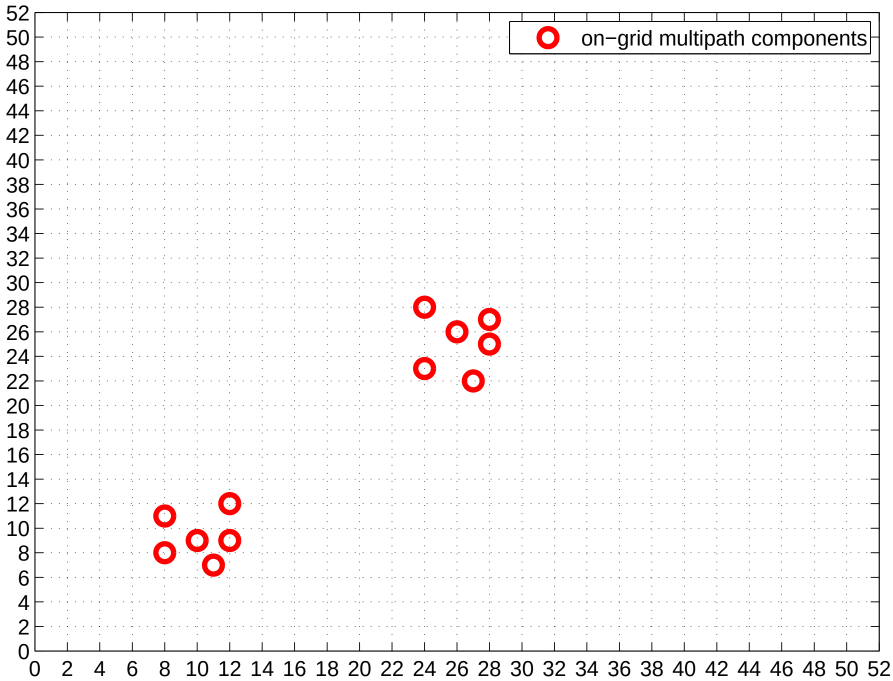

Figure 5.11: Location of on-grid multipath components in two separate clusters on delay-Doppler domain.

each multipath randomly within a limit κ, performance degrades severely. Since we cover all probable delay-Doppler parameter pairs, most realistic scenario is when $\kappa = 0.5$. Even for sparsity level smaller than 4, $\mathcal{S} \leq 4$, we have an approximately %30 decrease in recovery percentage.

In the following experiments, we will provide results obtained by using proposed technique for various different settings. In the first experiment, we will look for how much we can improve recovery ability with minimum resources. In other words, using minimum number of particles, PSO cycles and EM iterations. Choose number of particles as 2, number of PSO cycles as $10, 30, 50$, and number of EM iterations $\eta = 1$ and $\kappa = 0.5$. All simulations are conducted on an HP Desktop with Intel Core-2 2.13 GHz processor. Parameter estimation time of standart OMP technique is recorded as 0.012 *sec* and PSO-OMP with

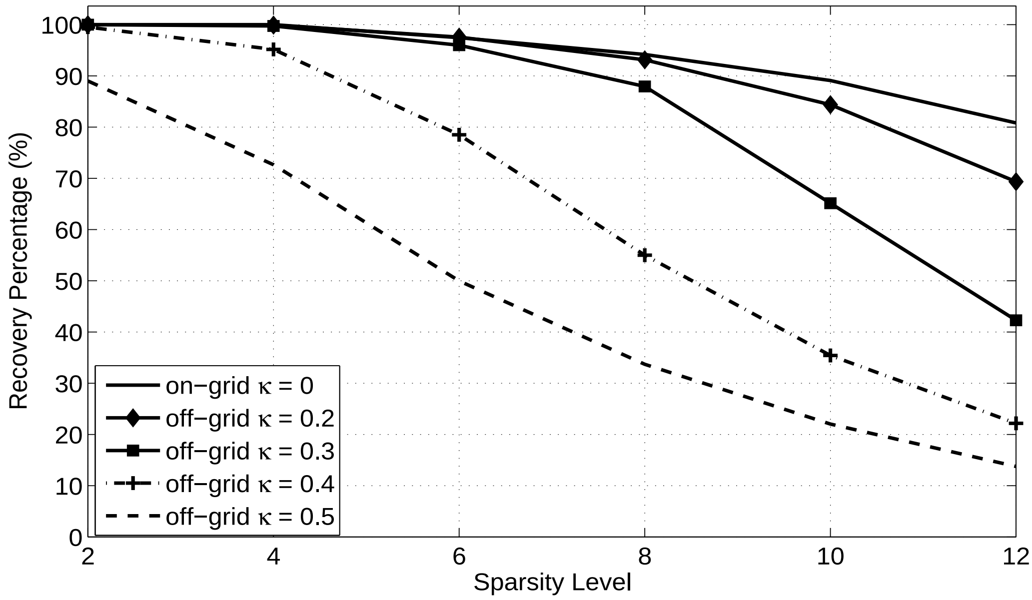

Figure 5.12: Recovery percentage the OMP technique for various sparsity and perturbation levels.

$\#particles = 2$, $\eta = 1$, $PSO\ cycles = 10$ is recorded as 0.3 sec for this specified scenario. In Figs. 5.13 performance of PSO-OMP with $\#particles = 2$ and $\eta = 1$ is compared with standart OMP and results are presented in terms of recovery percentage(%), rMSE and rMSE of detected multipath components. Perturbation limit κ is set to 0.5. 10, 30 and 50 PSO iterations are conducted. Even for 10 PSO iterations, PSO-OMP outperform OMP and solves the off-grid problem. For example, it seen that, for sparsity level 10, PSO-OMP with 10 PSO iterations increase the recovery %20. Moreover it is obvious that performance is increased with higher number of PSO iterations due to the increased chance of converging the global solution. In the second set of results that are presented in Figs. 5.14, we provide the performance improvements in recovery percentage, rMSE and rMSE of detected multipaths when we have 2 EM iterations instead of 1 EM iteration. As expected, since we better isolate the effect of multipath clusters to each other with addition of second EM iteration, we obtained better results. For sparsity level 6, recovery percentage is increased approximately %15, with addition of 1 EM iteration.

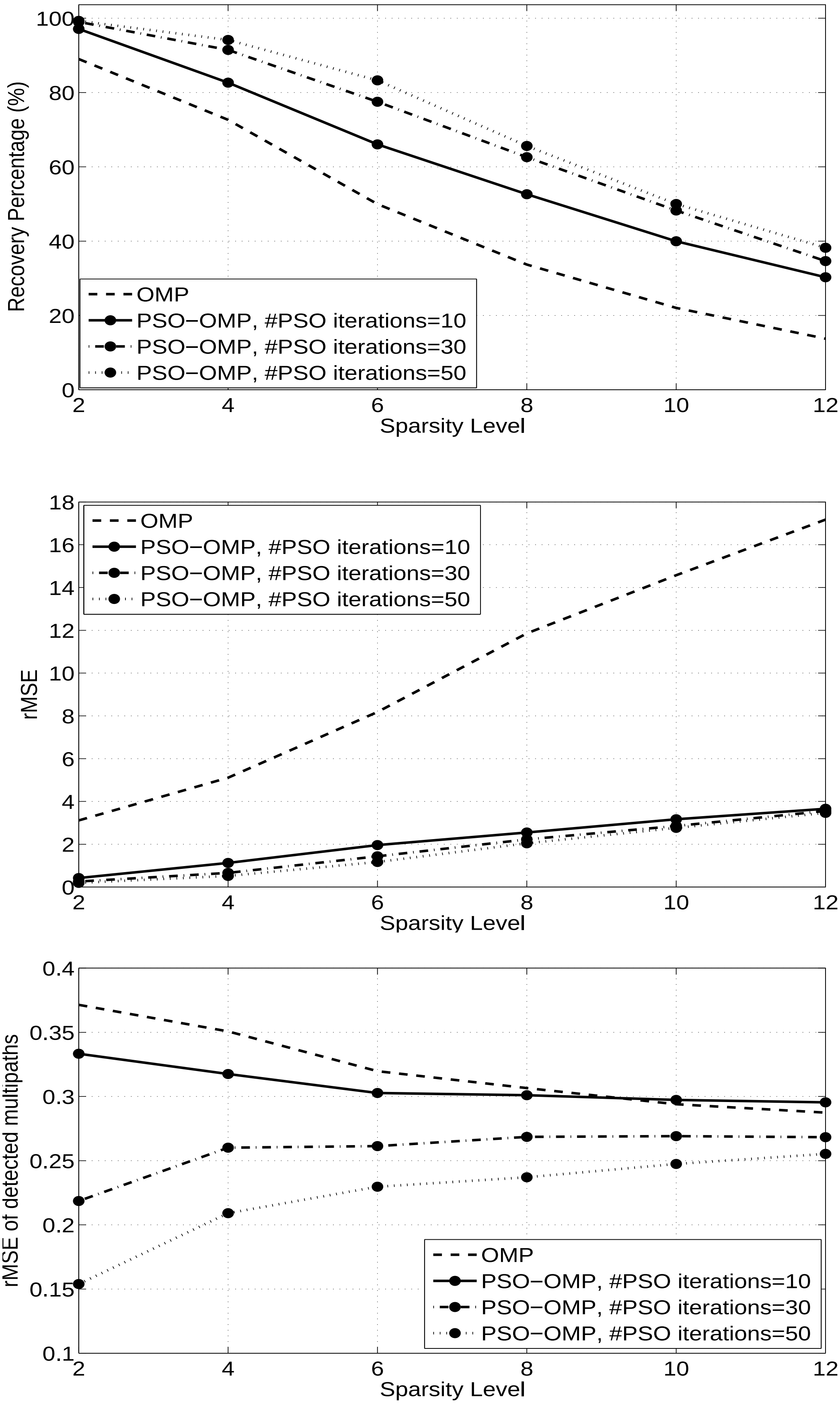

Figure 5.13: Recovery percentage, rMSE and rMSE of detected multipath components of OMP and PSO-OMP(number of EM iterations is 1 and number of particles is 2,) for various sparsity levels and number of PSO iterations, respectively. Perturbation limit, $\kappa = 0.5$.

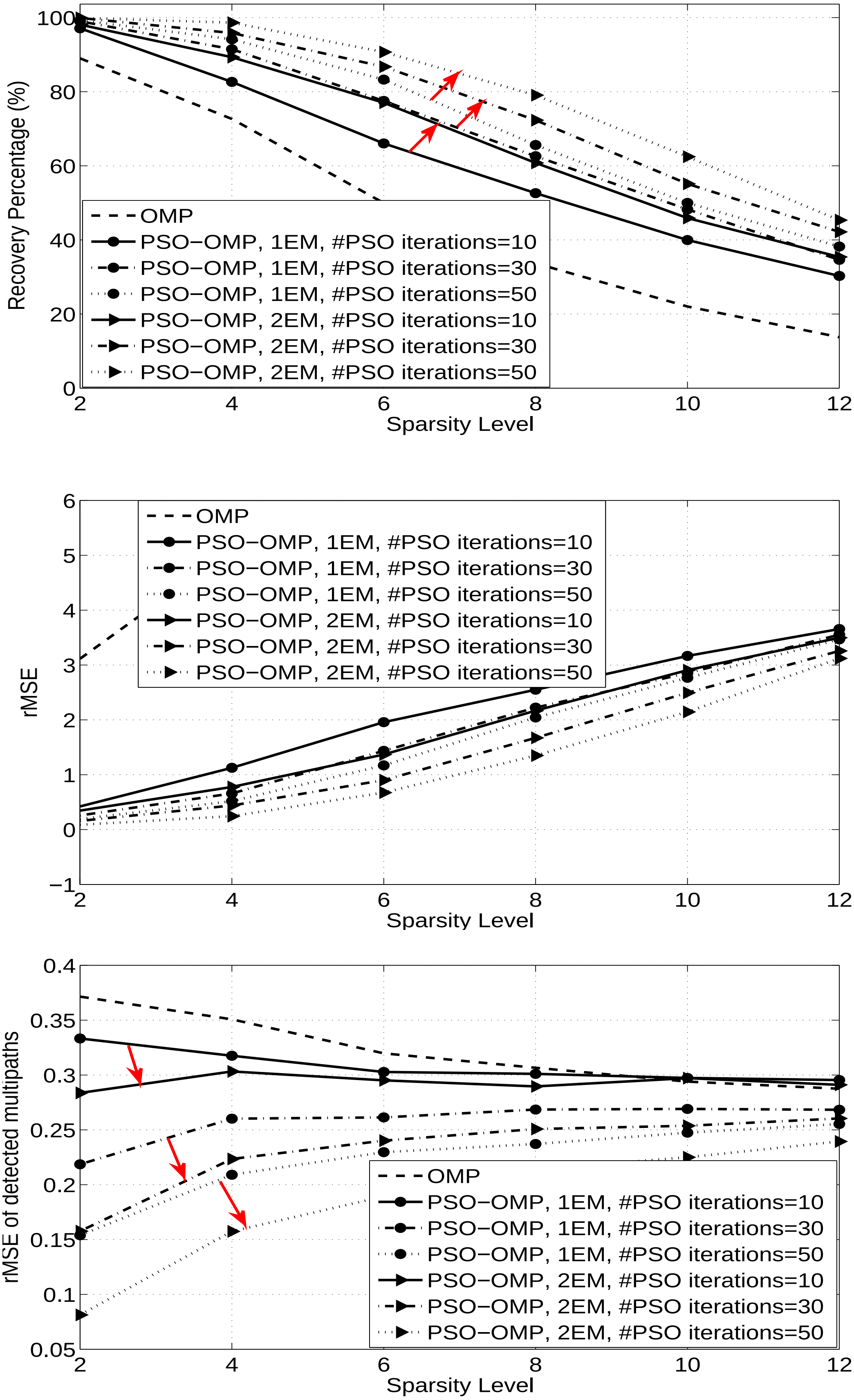

Figure 5.14: Recovery percentage, rMSE and rMSE of detected multipath components of OMP, PSO-OMP(number of EM iterations is 1 and number of particles is 2,) and PSO-OMP(number of EM iterations is 2 and number of particles is 2,) for various sparsity levels and number of PSO iterations, respectively. $\kappa = 0.5$.

In the third set of results we tested the performance of the algorithm by using more resources. Namely, number of particles is increased to 4 and number of PSO iterations are increased to 80. It is seen in Figs. 5.15 that performace is increased. For sparsity level 6, recovery percentage is increased approximately %10.

We also analyzed the error progress curves of EM and PSO iterations. In Fig. 5.16, the rMSE between measured and estimated receiver outputs obtained with PSO-OMP, are shown for 20 EM iterations values and for different sparsity levels. Number of PSO iterations and number of particles are chosen as 30, 2, respectively. The rMSE is monotonically decreases and saturates around after 20 iterations. Sharp decreases occur in between $1^{th} - 4^{th}$ iterations. However, as proofed in previously conducted experiments, even for 1 EM iteration, off-grid problem is successfully handled. In Fig. 5.17, normalized error versus number of PSO iterations curve obtained with PSO-OMP is shown. Number of EM iterations and number of particles are chosen as 2, and 2, respectively. Similar to the curve in Fig. 5.16, the rMSE is monotonically decreases and saturates around after 100 iterations. Meaning that, particles converged to a point and movement of particles does not change the estimation error anymore. Note from the results shown in Fig. 5.13 that only 10 PSO iterations are enough to get good results. Finally, similar to the results shown in Fig. 5.12, for various perturbation limit values performance of the PSO-OMP is tested. Number of EM iterations, number of particles and number of PSO iterations are chosen as 1, 2, 10, respectively. As expected, when we lower the perturbation limit we get better results. This is due to the fact that, since particles firstly search for the global optimum in the very vicinity of the on-grid point, they found the correct off-grid point rapidly and inrush onto the point.

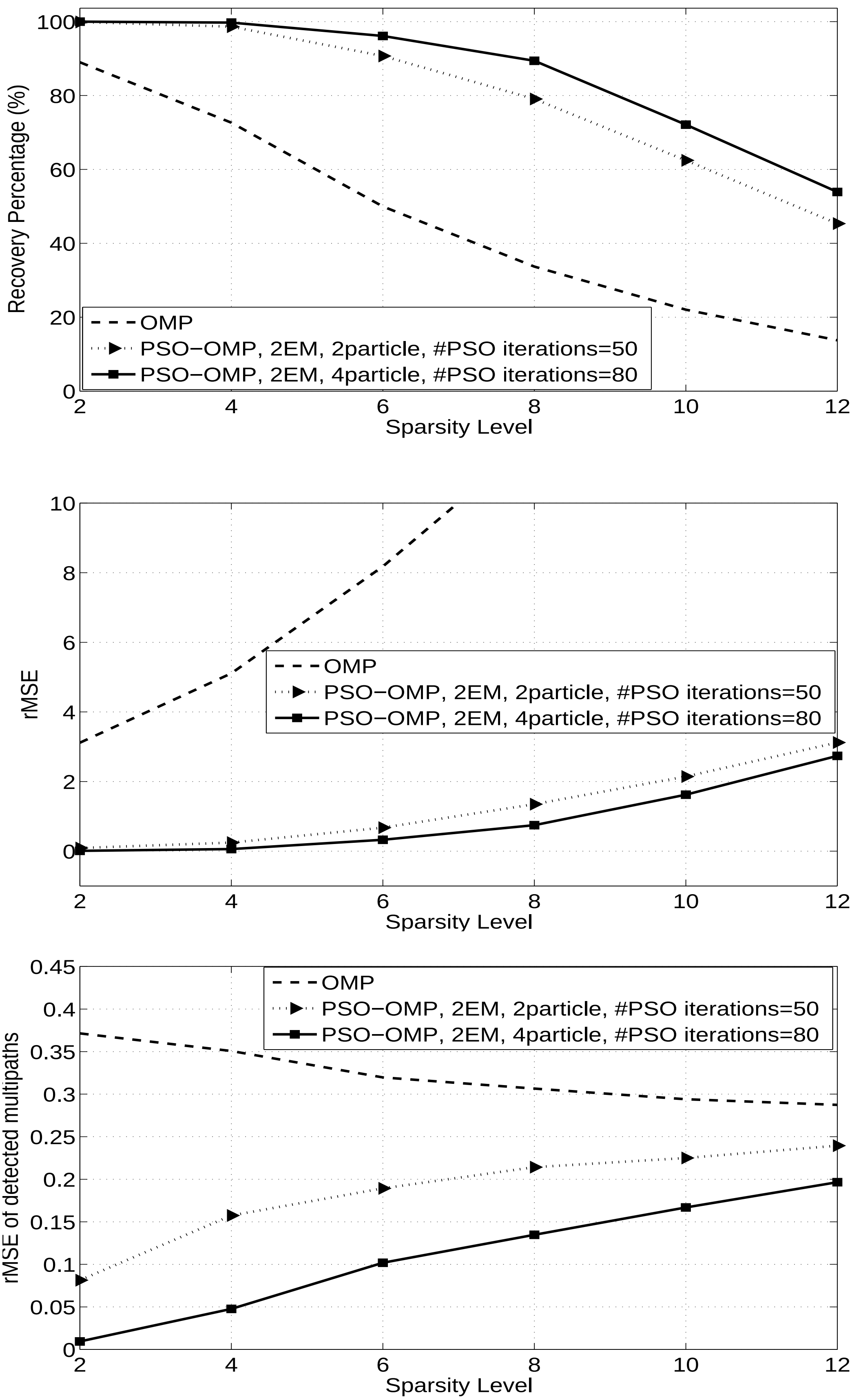

Figure 5.15: Recovery percentage, rMSE and rMSE of detected multipath components of OMP, PSO-OMP(number of EM iterations is 2 and number of particles is 2,) and PSO-OMP(number of EM iterations is 2 and number of particles is 4,) for various sparsity levels and number of PSO iterations, respectively. $\kappa = 0.5$.

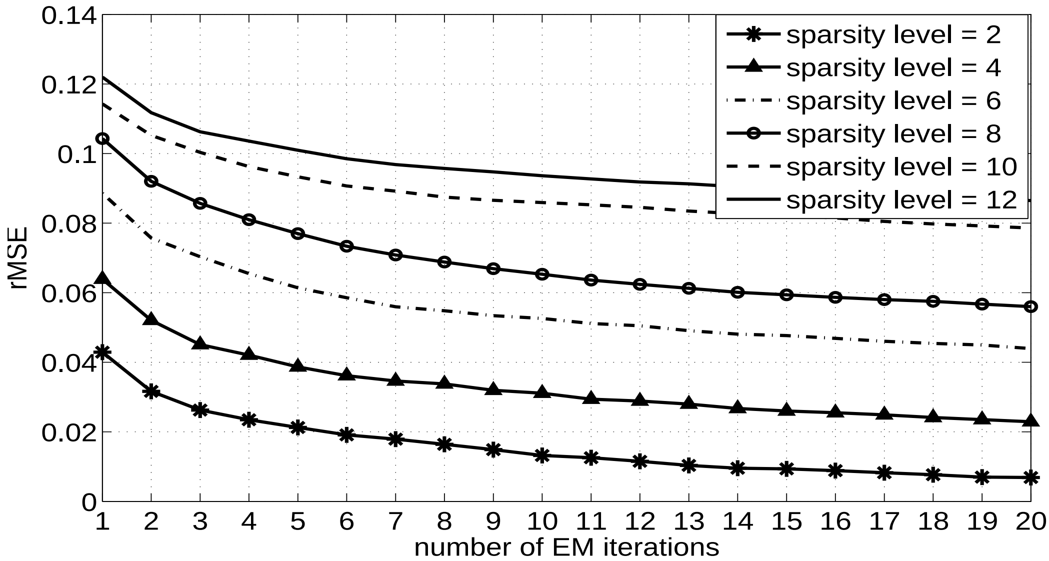

Figure 5.16: rMSE values for various EM iteration values and for various sparsity levels obtained with PSO-OMP. Number of particles is 2 and number of PSO iterations is 30.

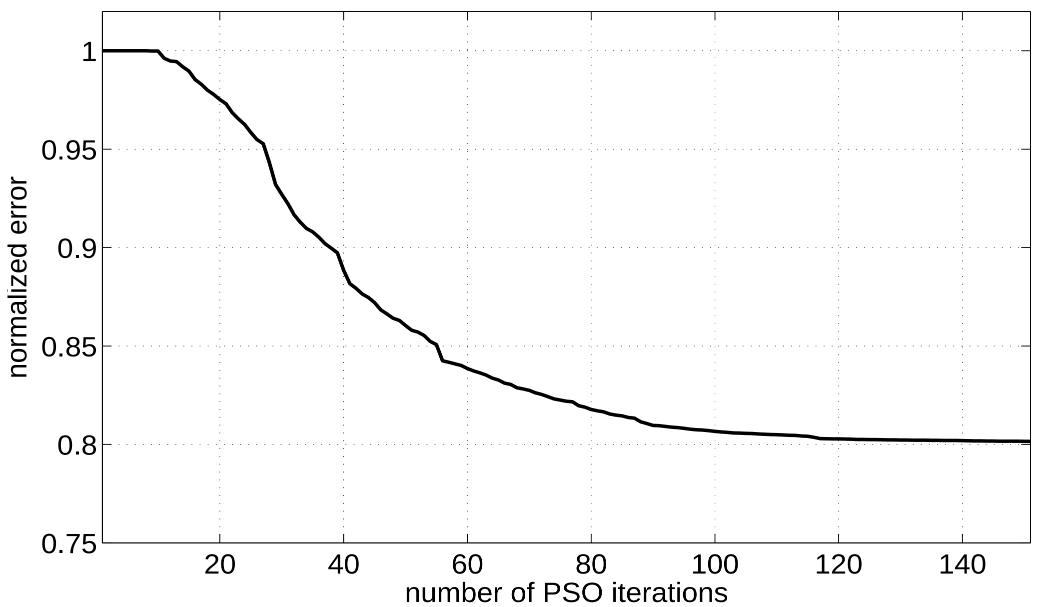

Figure 5.17: Normalized error during PSO iterations obtained with PSO-OMP. Number of particles is 2 and number of EM iterations is 2.

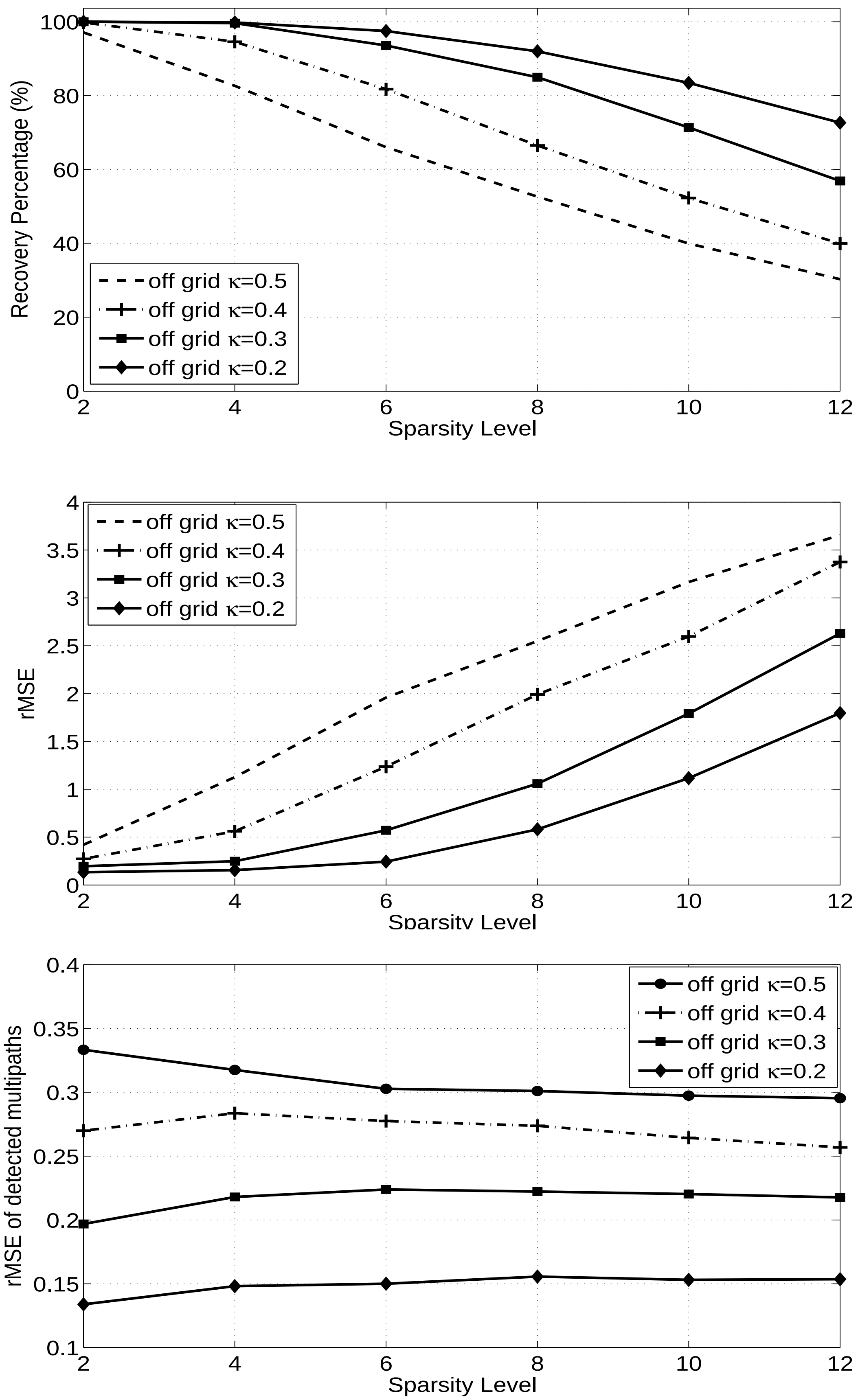

Figure 5.18: Recovery percentage, rMSE and rMSE of detected multipath components of PSO-OMP(number of EM iterations is 1 and number of particles is 2, number of PSO iterations is 10) for various sparsity levels and κ values. $\kappa = 0.5$.

5.6 Conclusions

Based on sparse approximation tools and compressed sensing theory, a new approach for identification of sparse multipath channels is presented. A general assumption used in all of the sparse multipath channel estimation techniques is that the all multipath components fall on the grid points, which is practically impossible as the target parameters are unknown. Performance of standard compressed sensing formulations based on discretization of the multipath channel parameter space degrade significantly when the actual channel parameters deviate from the assumed discrete set of values. To solve this so called "off-grid", we proposed a novel algorithm that can also be used in applications other than the multipath channel identification. The proposed algorithm, firstly makes use of the cross ambiguity function calculation and transform the receiver output to the delay-Doppler domain for efficient exploitation of the delay-Doppler diversity of the multipath signals. Then by detecting the candidate multipath clusters, the original channel identification problem is reduced to channel identification problems over the identified clusters in the delay-Doppler domain. After that, on-grid points that reside in each cluster are perturbed by using PSO and multipath components are recovered by using OMP in a greedy fashion. Superior performance of the proposed algorithm verified on various test scenarios.

Chapter 6

Conclusions and Future Work

In this thesis, new array signal processing techniques are developed for modeling multipath communication channels based on CAF calculation, swarm intelligence and CS theory. First proposed technique called as CAF-DF calculates CAF on each antenna output to detect the presence of multipath signals and iteratively estimates DOAs, time-delays and Doppler shifts of each impinging onto an antenna array. The key success behind the CAF-DF technique is its ability to separate multipath components on delay-Doppler domain and to suppress the sidelobe interference effects between each multipath component. Superior performance of the CAF-DF technique is verified on real ionospheric data.

Secondly developed technique named as particles swarm optimization cross ambiguity function (PSO-CAF), transforms the receiver array outputs to delay-Doppler domain by integrating CAF calculation. By this way, diverse structure of the multipath environment is revealed for accurate and reliable channel modeling. PSO is used to estimate parameters of each multipath component in each cluster that is detected on the delay-Doppler surface by an amplitude thresholding.

In the third developed technique, key ideas from CS theory, swarm intelligence and CAF computation are combined in the estimation process. Standard

CS based sparse channel modelling techniques assume that the multipath channel parameters reside on a predefined set of discrete values. However, in practice actual channel parameters deviate from the assumed discrete set of values and this so called off-grid problem degrade the performance of the algorithms severely. To overcome this problem, a new technique is presented by using PSO. Performances of the developed techniques are tested successfully on various scenarios.

CS theory and sparse representations have attracted many researchers from wide range of disciplines in last decade and changed the way information is represented. However, there still exists many open practical problems especially in array signal processing and channel estimation waiting to be answered such as the off-grid problem that we have proposed a candidate solution in this thesis. For example, faster, adaptive and robust to noise techniques that can handle off-grid scenarios can be developed and tested for various sparse recovery tools. Secondly, new training signal variants can be generated based on the distribution of multipath clusters on delay-Doppler domain and coherency of sensing dictionary to further improve the performance of current recovery techniques in noisy practical multipath scenarios. Lastly, different popular variants of standard PSO and other swarm intelligence based approaches can be analyzed and compared with each other in off-grid problem.

APPENDIX A

Particle Swarm Optimization (PSO)

Particle swarm optimization (PSO) is an evolutionary stochastic optimization algorithm, developed by Kennedy and Eberhart in 1995 [35]. PSO has been shown to be very effective in optimizing challenging multidimensional, nonlinear and multimodal problems in a variety of fields such as signal processing [38], communication networks [39], biomedical [40], [41], control [42], [43], robotics [44], power systems [45], electromagnetics [46], image and video analysis [47]. It was inspired by the social behavior of animals, specifically the ability of groups of animals to work collectively in finding the desirable positions in a given area. Fish schooling and bird flocking are two very good examples. PSO algorithm operates on a set of solution candidates that are called as swarm of particles. The particles travel through a multidimensional search space, where the position of each particle is adjusted based on a combination of its individual best position and the best position of the whole particle set ever visited. A few key points about PSO should be stated here to clarify the advantages of it over Newton-type techniques: 1) less sensitive to initialization, 2) better chance to find global optimum and 3) provides more accurate estimates. Moreover, compared to other global optimization techniques, such as genetic algorithm (GA) [30], some superior properties of PSO can be pointed out that: 1) faster in convergence; 2) easier to implement, simpler in concept; 3) can be adapted to different application domains and hybridized with other techniques; 4) interaction between particles is defined in such a way that logic behind the ideal social communication in a community is preserved and diversity of the swarm is maintained through the solution search; 5) better memory management. The components of the PSO setup can be itemized as follows:

- A set of parameters and their corresponding search intervals: For the multipath channel identification, the parameters are the delay, Doppler shift, elevation and azimuth angle of arrivals of each path.
- A fitness function is used to compare the performance of each particle in the swarm: For the multipath channel identification log-likelihood function can be used for this purpose.
- An update strategy for reposition of particles in the swarm.

Although there are variants in the literature, the following stages describes the general dynamics of the PSO.

1. *Initialization:* Each particle in the swarm starts searching for the optimal position in the solution space at its own random location with a velocity that is random both in its direction and magnitude. This first location is recorded as their ***personalBest*** for each particle. ***globalBest*** is initialized as the location of the particle that has the best fit.
2. *Coordinate update:* Each particle travels through the multidimensional search space, where the position and velocity of each particle is adjusted according to certain update rules at each time step. Each particle l consists of three vectors: its location in K-dimensional search space

$\mathbf{z}_l = [z_{l1}, z_{l2}, ..., z_{lK}]$, its historicaly best position $\mathbf{p}_l = [p_{l1}, p_{l2}, ..., p_{lK}]$ and its velocity $\boldsymbol{\upsilon}_l = [\upsilon_{l1}, \upsilon_{l2}, ..., \upsilon_{lK}]$. In each time step, using the positions of the particle, a fitness function is evaluated. If this fitness value is greater than the value corresponding to ***personalBest*** for that particle, or ***globalBest*** for the swarm, then these locations are updated with the current location. The velocity and the location of each particle is updated according to the relative positions of ***personalBest*** ($\mathbf{p}_l$) and ***globalBest*** ($\mathbf{p}_g$) by the following equation:

$$\begin{aligned} \upsilon_{lk} &= \vartheta\left(\upsilon_{lk} + c_1\epsilon_1\ (p_{lk} - z_{lk}) + c_2\epsilon_2\ (p_{gk} - z_{lk})\right) \\ z_{lk} &= z_{lk} + \upsilon_{lk} \quad , \end{aligned} \tag{A.1}$$

where c_1 is so called the cognitive factor that adjusts how much the particle is influenced by the historical best position of his own, c_2 is so called the social factor that adjusts how much the particle is influenced by the historical best of the swarm, ϵ_1 and ϵ_2 are two uniformly distributed random numbers. ϑ is the constriction factor, that balances global and local searches and defined as [100]:

$$\vartheta = \frac{2}{\left|2 - \varsigma - \sqrt{\varsigma^2 - 4\varsigma}\right|} \quad , \tag{A.2}$$

where $\varsigma = c_1 + c_2$. Recommended values for these constants are $c_1 = c_2 = 2.05$ and $\vartheta = 0.72984$.

3. *Convergence check:* The optimization process is repeated starting at step 2) until convergence is established or the maximum allowed number of iterations are reached.

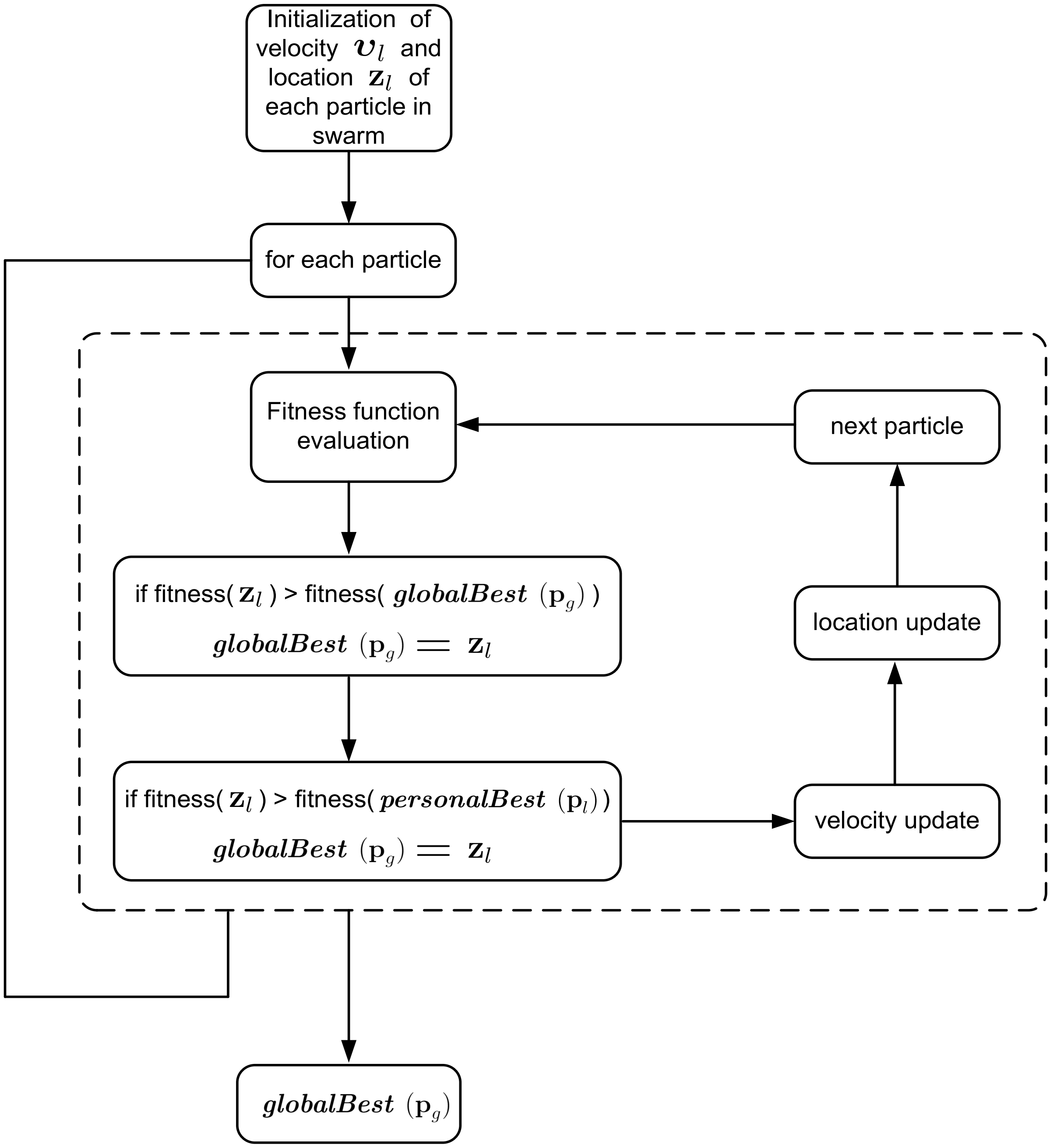

Figure A.1: Flow chart of the particle swarm optimization.

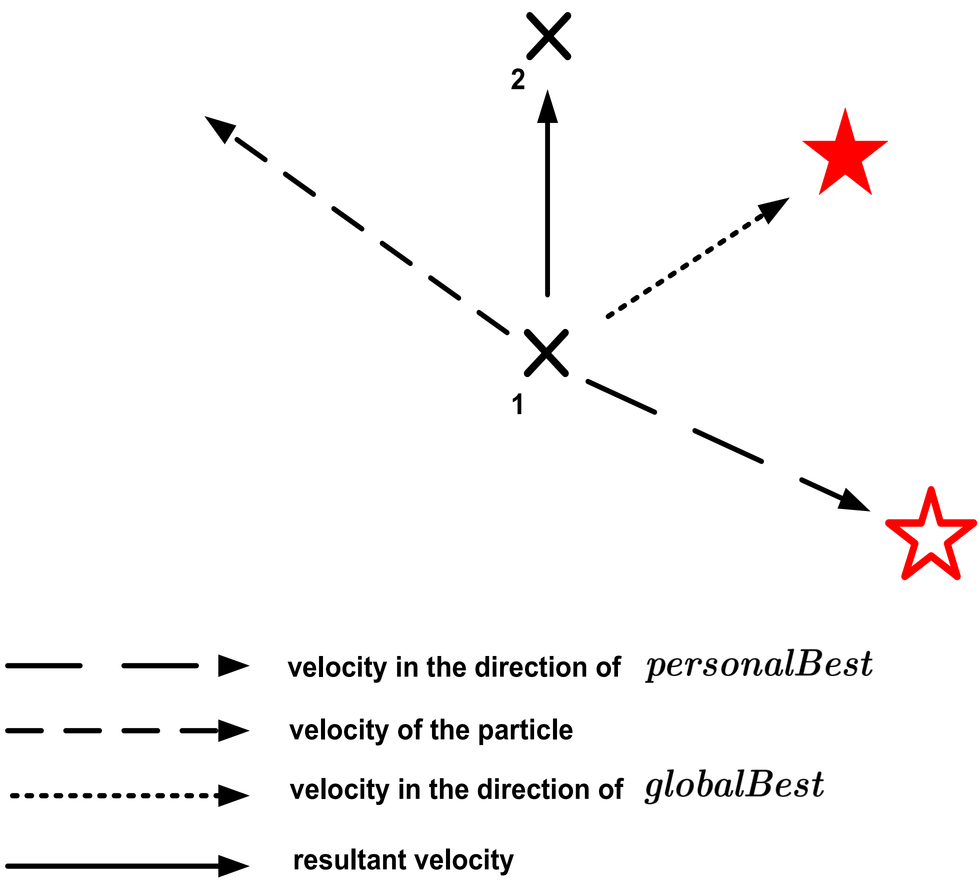

Figure A.2: Location update from location **1** to location **2** of a particle illustrated with $\times$. Particles ($\times$) accelerated toward the location of the best solution **globalBest** ($\star$), and the location of their own personal best **personalBest**, in a 2-D parameter space.

APPENDIX B

Matched Filter and Ambiguity Function

A matched filter can be defined as a type of filter matched to the known or assumed characteristics of a target signal, designed to optimize the detection of that signal in the presence of noise [23]. In the case of white additive noise, the highest SNR at the detector is obtained when the received signal is correlated with the replica of the transmitted signal. In this section, firstly complex envelopes of the narrow bandpass signals, which make the design of the matched filter simple, will be described. After that, basics of the matched filter and how we get to the ambiguity function will be discussed.

Narrowband bandpass signals can be represented in several ways. The simplest one is

$$s(t) = g(t)\cos[\omega_c t + \Phi(t)] \tag{B.1}$$

where $\Phi(t)$ is the instantaneous phase and $g(t)$ is the envelope of $s(t)$. Second form is

$$s(t) = g_c(t)\cos(\omega_c t) - g_s(t)\sin(\omega_c t) \tag{B.2}$$

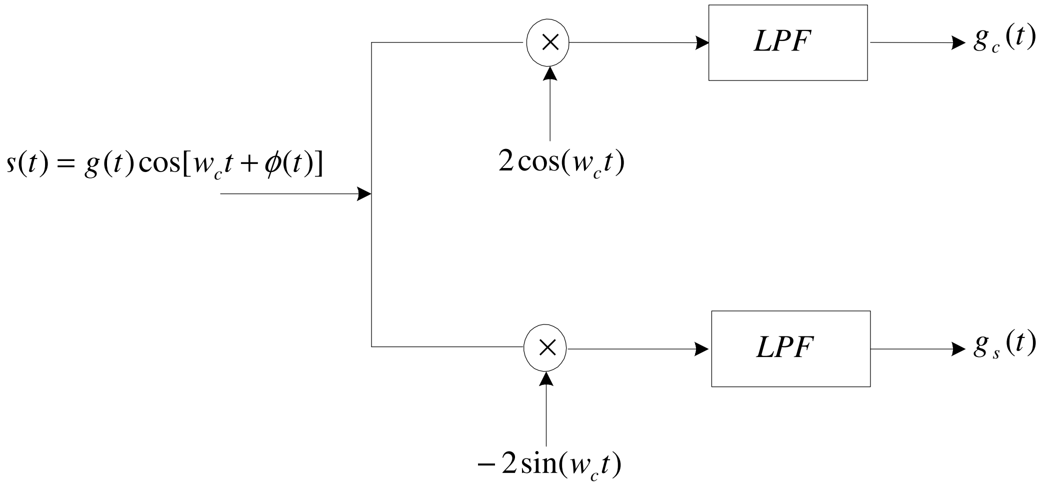

Figure B.1: IQ Detector.

where $g_c(t)$ and $g_s(t)$ are the *in-phase* and *quadrature* baseband components, respectively, and represented as follows

$$g_c(t) = g(t)\cos(\Phi(t)) \tag{B.3}$$

$$g_s(t) = g(t)\sin(\Phi(t)) \quad . \tag{B.4}$$

An I/Q detector, depicted in Fig. B.1 is used to eliminate the in-phase **I** and the quadrature **Q** components using a low-pass filter which discards the high frequency terms. A third form of a narrow bandpass signal is

$$s(t) = Re\{u_e(t)\exp(jw_c t)\} \tag{B.5}$$

where $u_e(t)$ is called the complex envelope of the signal $s(t)$ and is defined as

$$u_e(t) = g_c(t) + jg_s(t) \quad . \tag{B.6}$$

The angular frequency w_c is called as the carrier frequency and it is significantly larger than the bandwidth of the baseband signal. The fourth and the most general form of a narrow bandpass signal is

$$s(t) = \frac{1}{2}u_e(t)\exp(jw_c t) + \frac{1}{2}u_e^*(t)\exp(-jw_c t) \quad . \tag{B.7}$$

Now we can get into the motivation and derivation of the matched filter and the ambiguity function.

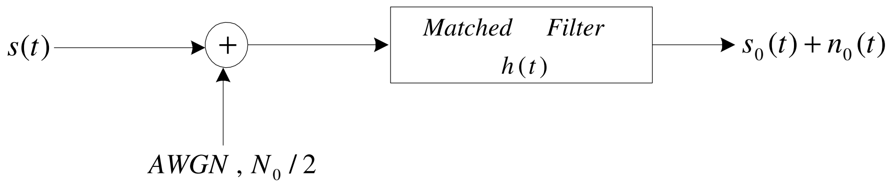

Figure B.2: Matched filter block diagram.

Matched filters can be designed for both baseband and bandpass real signals. In the following derivations, a filter matched to the complex envelope of the signal will be considered. In Fig. B.2, the input signal to the filter is the $s(t)$ in additive white gaussian noise with a two-sided power spectral density of $N_0/2$ [23]. Impulse response of the filter is $h(t)$ and the frequency response is $H(w)$. The objective here is to find a $h(t)$, which yields the maximum output SNR at a specific t_0 when we decide on the presence or absence of $s(t)$ in white noise. The mathematics of this objective is maximizing

$$\left(\frac{S}{N}\right)_{out} = \frac{|s_o(t_0)|^2}{\overline{n_o^2(t)}} \quad . \tag{B.8}$$

Assuming S(w) is the Fourier transform of the s(t), one can write the output of the matched filter at t_0 as

$$s_o(t_0) = \frac{1}{2\pi}\int_{-\infty}^{\infty} H(w)S(w)e^{jwt_0}dw \tag{B.9}$$

The mean-squared value of the noise is

$$\overline{n_o^2(t)} = \frac{N_0}{4\pi}\int_{-\infty}^{\infty} |H(w)|^2 dw \tag{B.10}$$

If we substitute (B.9) and (B.10) into (B.8) output SNR becomes

$$\left(\frac{S}{N}\right)_{out} = \frac{\left|\int_{-\infty}^{\infty} H(w)S(w)\exp(jwt_0)dw\right|^2}{\pi N_0 \int_{-\infty}^{\infty} |H(w)|^2 dw} \quad . \tag{B.11}$$

Using the *Schwarz inequality*, (B.11) can be rewritten as

$$\left(\frac{S}{N}\right)_{out} \leq \frac{1}{\pi N_0}\int_{-\infty}^{\infty} |S(w)|^2 dw = \frac{2E}{N_0} \tag{B.12}$$

where E is the energy of the signal:

$$E = \int_{-\infty}^{\infty} s^2(t)dt = \frac{1}{2\pi}\int_{-\infty}^{\infty} |S(w)|^2 dw \tag{B.13}$$

The equality in the above, *Schwarz* upper bound can be achieved by the following filter response which is the matched filter:

$$H(w) = KS^*(w)e^{-jwt_0} \quad . \tag{B.14}$$

Taking the inverse fourier transform, impulse response of the filter reveals as

$$h(t) = Ks^*(t_0 - t) \quad , \tag{B.15}$$

meaning that delayed mirror image of the conjugate of the signal is impulse response of the matched filter. Using this configuration, at $t = t_0$, one can obtain a maximum output SNR value of $2E/N_0$. This result is interesting in the sense that, maximum SNR at the output of a matched filter is only a function of the signal energy but not its shape.

Let's now investigate a filter matched to a narrowband bandpass signal. If we use the forth form of $s(t)$, given in (B.7), in (B.9) we get the equation below:

$$\begin{aligned} s_o(t) = & \frac{K}{4}\int_{-\infty}^{\infty}\left[u_e(\tau)e^{jw_c\tau} + u_e^*(\tau)e^{-jw_c\tau}\right] \\ & .\left\{u_e^*(\tau - t + t_0)e^{-jw_c(\tau-t+t_0)} + u_e(\tau - t + t_0)e^{jw_c(\tau-t+t_0)}\right\}d\tau \ . \end{aligned} \tag{B.16}$$

After straightforward simplifications, $s_o(t)$ can be obtained as:

$$s_o = Re\left(\left[\frac{1}{2}Ke^{-jw_ct_0}\int_{-\infty}^{\infty}u_e(\tau)u_e^*(\tau - t + t_0)d\tau\right]e^{jw_ct}\right) \quad . \tag{B.17}$$

From this long equation, we can separate out a new complex envelope:

$$u_o(t) = \frac{1}{2}Ke^{-jw_ct_0}\int_{-\infty}^{\infty}u_e(\tau)u_e^*(\tau - t + t_0)d\tau \quad , \tag{B.18}$$

and in the end we obtain the output of the matched filter as

$$s_o(t) = Re\{u_o(t)\exp(jw_ct)\} \quad . \tag{B.19}$$

This equation tells us that the output of a filter matched to a narrowband bandpass signal has a complex envelope $u_o(t)$ obtained by passing the complex envelope $u_e(t)$ of the narrowband bandpass signal through its own matched filter.

Therefore, in applications where narrowband bandpass signals used, it is sufficient to work with the complex envelope $u(t)$ of the signal and its matched filter output $u_o(t)$. Once $u_o(t)$ is obtained, $s_o(t)$ could be found by (B.19).

The above derivation of the matched filter ignored the potential Doppler shift on the received signals. However in wireless communication, when the receiver is moving relative to the transmitter or the received waves bounced off from moving objects, the received signal suffers a Doppler shift. When the Doppler shift is not known, performance of the receiver that makes use of a matched filter matched to the transmitted signal may significantly degrade. Now let's modify the input complex envelope with a Doppler shift as below:

$$u_d(t) = u_e(t) \exp(j2\pi\nu t) \quad . \tag{B.20}$$

In order to find the output complex envelope we replace the first $u_e(t)$ in (B.18) by $u_d(t)$ and choose $t_0 = 0, K = 1$ yields a function carrying both doppler shift and time information:

$$u_o(t, \nu) = \int_{-\infty}^{\infty} u(\tau) \exp(j2\pi\nu\tau) u^*(\tau - t) d\tau \quad . \tag{B.21}$$

Another form of the equation above is the well-known *ambiguity function* and given as

$$\chi_{u_e,u_e}(\tau, \nu) = \int_{-\infty}^{\infty} u_e(t) u_e^*(t - \tau) e^{j2\pi\nu t} dt \quad . \tag{B.22}$$

The ambiguity function (AF), characterizes the output of a matched filter when the input signal is delayed by τ and Doppler shifted by ν. This function was first introduced by Woodward in 1953 and found useful in wide variety of applications. Moreover, symmetrical cross-ambiguity function can be written as:

$$\chi_{x,u_e}(\tau, \nu) = \int_{-\infty}^{\infty} x\left(t + \frac{\tau}{2}\right) u_e^*\left(t - \frac{\tau}{2}\right) e^{-j2\pi\nu t} dt \tag{B.23}$$

Let's now mention some of the important properties of AF. If we assume that the energy E of $u_e(t)$ is normalized to unity, maximum value of the ambiguity

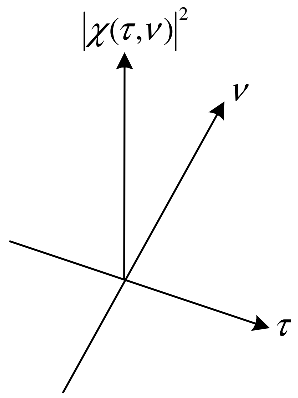

Figure B.3: Ideal ambiguity function; $\left|\chi(\tau,\nu)\right|^2 = \delta(\tau,\nu)$.

function occurs at the origin and equals to one. We can formalize it as

$$\left|\chi(\tau,\nu)\right| \leq \left|\chi(0,0)\right| = 1 \quad . \tag{B.24}$$

Total volume under the normalized ambiguity surface equals unity, independent of the signal waveform:

$$\int_{-\infty}^{\infty}\int_{-\infty}^{\infty}\left|\chi(\tau,\nu)\right|^2 d\tau d\nu = 1 \quad . \tag{B.25}$$

These two properties states that, if one try to squeeze the AF to a narrow peak at the origin, that peak cannot exceed a value of one and the volume squeezed out of that peak must reappear somewhere else [98]. Therefore, the behavior of the ambiguity diagram indicates that there have to be trade-offs made among the resolution, accuracy, and ambiguity. Thirdly, AF is symmetric with respect to the origin;

$$\left|\chi(-\tau,-\nu)\right| = \left|\chi(\tau,\nu)\right| \tag{B.26}$$

which suggests that it is sufficient to study only two adjacent quadrant of the AF.

Although it is not realistic, the “ideal” ambiguity diagram would consists of a single infinitesimal thickness peak at the origin and be zero everywhere else, as shown in Fig. 2.5. This figure tells us that we have no ambiguities in range or doppler frequency. Time delay and/or frequency could be determined simultaneously to as high a degree of accuracy as wanted.

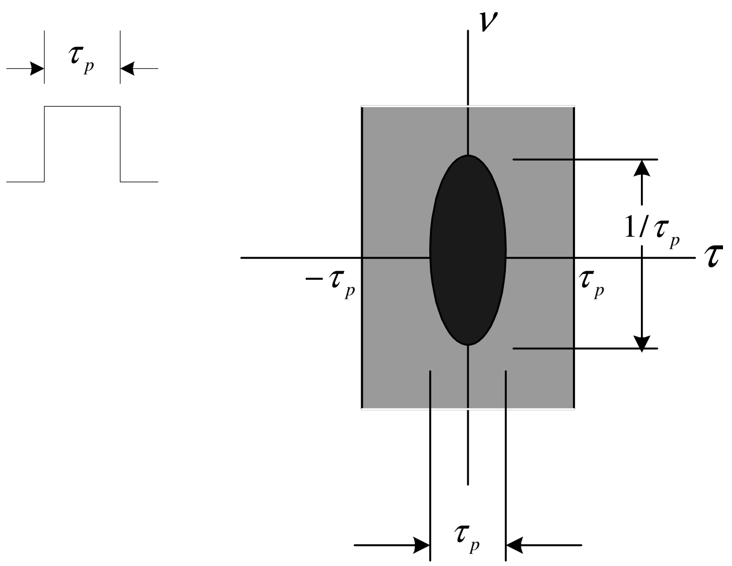

Figure B.4: 2D view of the ambiguity function for a single pulse of width τ_p.

Usually two dimensional plots of ambiguity diagrams are used to gather information. In Fig. B.4, two dimensional representation of the ambiguity diagram for a single unmodulated pulse obtained by gating a sinusoid signal of width τ_p is given. Black shaded regions indicate that $|\chi(\tau,\nu)|^2$ is large and gray regions indicate that $|\chi(\tau,\nu)|^2$ is small. This figure says that if τ_p is large corresponding to a long pulse, we have poor delay and good doppler accuracy. The opposite occurs for a short pulse. The short pulse is doppler tolerant, meaning that the output from a filter matched to a zero doppler shift will not change much when there is a doppler shift. However, the long pulse is not doppler tolerant, and produce reduced output for a doppler-frequency shift. Lastly for this unmodulated pulse, the time bandwidth product (TBP) which is defined as the 3-dB timewidth times the 3-dB bandwidth of the pulse is one. For modulated pulses the TBP may significantly exceed one.

Each different waveform yields a new distribution of ambiguity. There are several types of signals that are commonly used in practice. Two important examples are the periodic continuous wave (CW) radar signal and a coherent train of identical pulses. In Fig. B.5, ambiguity distribution of a uniform pulse train is shown. If there are N pulses of duration τ_p in a pulse train where pulses are separated by T/N, the Doppler measurement accuracy becomes $1/T$ which can be many time more accurate than the accuracy provided by a single pulse. This fact is illustrated in Fig. B.5. To increase the delay accuracy, transmitted pulses can be modulated either by using phase or frequency modulations. For example, if the pulse of duration τ_p is divided into 13 subpulses where the phase of each subpulse is chosen to be $\{11111-1-111-11-11\}$, which is known as the Barker-13 sequence, the delay accuracy can be increased by 13 times. Note that, the Ambiguity distribution of a Barker-13 sequence is plotted in Fig. B.6. The TBP of this sequence is thirteen.

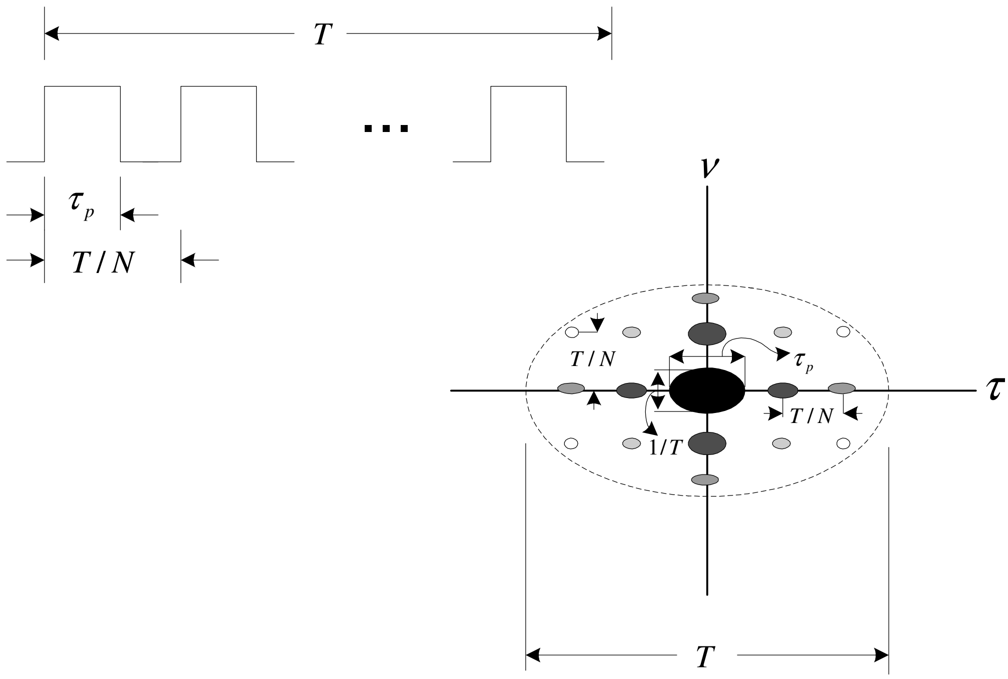

Figure B.5: Ambiguity function distribution of an uniform pulse train.

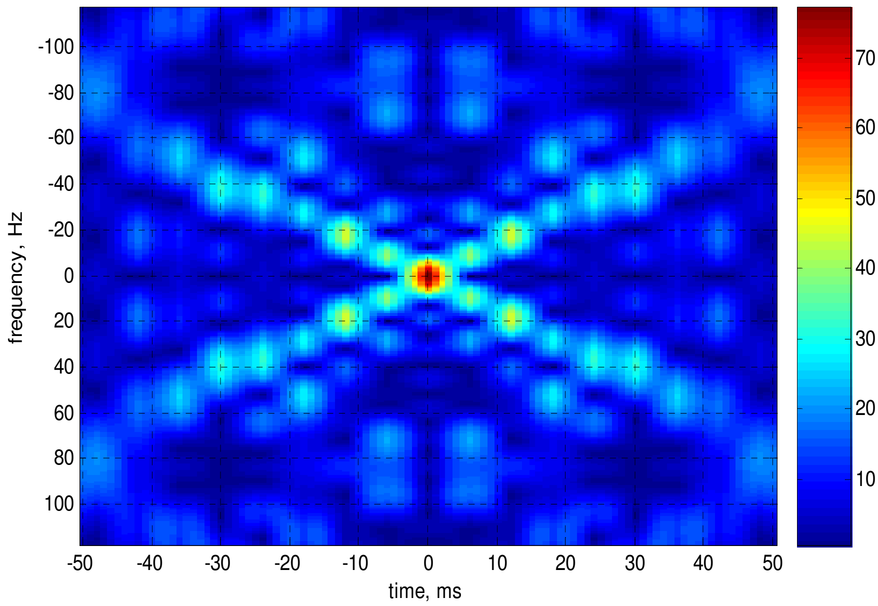

Figure B.6: Ambiguity function distribution of a Barker-13 sequence.

APPENDIX C

Cramer-Rao Lower Bound

In this appendix derivation of the CRB for the joint estimation problem is presented. In our model, residual error vector $\mathbf{e}(t_k)$ defined below has a circularly symmetric i.i.d. Gaussian distribution:

$$\mathbf{e}(t_k) = \mathbf{x}(t_k) - \sum_{i=1}^{d} \mathbf{a}(\theta_i, \phi_i)\zeta_i s(t_k - \tau_i)e^{j2\pi\nu_i t} \quad . \tag{C.1}$$

Assuming the variance of the distribution is σ^2, the log likelihood function can be written as

$$\mathfrak{L} = -NM\log\pi\sigma^2 - \frac{1}{\sigma^2}\sum_{\mathrm{k=1}}^{\mathrm{N}} \|\mathbf{e}(\mathrm{t_k})\|^2 \quad . \tag{C.2}$$

Using straightforward differentiations we obtain the following partial differentials that will be used to derive the entries of the Fisher Information Matrix (FIM):

$$\frac{\partial\mathfrak{L}}{\partial\tau_i} = \frac{2}{\sigma^2}\sum_{k=1}^{N} \Re e\left[\zeta_i^H \mathbf{a}^H(\theta_i, \phi_i)e^{-j2\pi\nu_i t_k}\frac{\partial s^H(t_k - \tau_i)}{\partial t}\mathbf{e}(t_k)\right] \tag{C.3}$$

$$\frac{\partial\mathfrak{L}}{\partial\theta_i} = \frac{2}{\sigma^2}\sum_{k=1}^{N} \Re e\left[\zeta_i^H s^H(t_k - \tau_i)e^{-j2\pi\nu_i t_k}\frac{\partial \mathbf{a}^H(\theta_i, \phi_i)}{\partial\theta_i}\mathbf{e}(t_k)\right] \tag{C.4}$$

$$\frac{\partial \mathfrak{L}}{\partial \phi_i} = \frac{2}{\sigma^2}\sum_{k=1}^{N} \Re e\left[\zeta_i^H s^H(t_k-\tau_i)e^{-j2\pi\nu_i t_k}\frac{\partial \mathbf{a}^H(\theta_i,\phi_i)}{\partial \phi_i}\mathbf{e}(t_k)\right] \tag{C.5}$$

$$\frac{\partial \mathfrak{L}}{\partial \nu_i} = \frac{-4\pi}{\sigma^2}\sum_{k=1}^{N} t_k \Im m\left[\zeta_i^H s^H(t_k-\tau_i)e^{-j2\pi\nu_i t_k}\mathbf{a}^H(\theta_i,\phi_i)\mathbf{e}(t_k)\right] \tag{C.6}$$

If we define $\zeta_i = \eta_i + j\kappa_i$, we obtain

$$\frac{\partial \mathfrak{L}}{\partial \eta_i} = \frac{2}{\sigma^2}\sum_{k=1}^{N} \Re e\left[s^H(t_k-\tau_i)e^{-j2\pi\nu_i t_k}\mathbf{a}^H(\theta_i,\phi_i)\mathbf{e}(t_k)\right] \tag{C.7}$$

$$\frac{\partial \mathfrak{L}}{\partial \kappa_i} = \frac{2}{\sigma^2}\sum_{k=1}^{N} \Im m\left[s^H(t_k-\tau_i)e^{-j2\pi\nu_i t_k}\mathbf{a}^H(\theta_i,\phi_i)\mathbf{e}(t_k)\right] \tag{C.8}$$

The following identities [135], are useful to determine the elements of the FIM.

$$E\big[\boldsymbol{e}_i(t_k)\boldsymbol{e}_c^H(t_j)\big] = \delta_{ic}\delta_{t_k t_j}\sigma^2 \tag{C.9}$$

$$E\big[\boldsymbol{e}_i(t_k)\boldsymbol{e}_z(t_j)\big] = 0 \tag{C.10}$$

$$E\big[\boldsymbol{e}_c^H(t_k)\boldsymbol{e}_l(t_j)\boldsymbol{e}_n(t_i)\big] = 0 \tag{C.11}$$

$$E\big[\boldsymbol{e}(t_k)\boldsymbol{e}^H(t_k)\boldsymbol{e}(t_j)\boldsymbol{e}^H(t_j)\big] = M^2\sigma^4 + \delta_{t_k t_j}M\sigma^4 \quad , \tag{C.12}$$

where $\boldsymbol{e}_i(t_k)$ is the i^{th} component of the $\boldsymbol{e}(t_k)$ and δ represents Kronecker's delta. Moreover, to make equations shorter, following equalities are defined;

$$R_{s's}^{i,l}(k) = \frac{\partial s^H(t_k-\tau_i)}{\partial t}s(t_k-\tau_l) \quad , \tag{C.13}$$

$$\gamma(k) = e^{-j2\pi(\nu_i-\nu_l)t_k} \quad , \tag{C.14}$$

$$\Psi_{\mathbf{a}'_\theta \mathbf{a}}^{i,l} = \frac{\partial \mathbf{a}^H(\theta_i, \phi_i)}{\partial \theta_i} \mathbf{a}(\theta_l, \phi_l) \quad . \tag{C.15}$$

Using these identities elements of the FIM matrix can be obtained as follows:

$$E\left[\frac{\partial \mathfrak{L}}{\partial \tau_i} \frac{\partial \mathfrak{L}}{\partial \tau_l}\right] = \frac{2}{\sigma^2} \Re e \left[\Psi_{\mathbf{aa}}^{i,l} \zeta_i^H \zeta_l \sum_{k=1}^{N} R_{s's'}^{i,l}(k) \gamma(k)\right] \quad . \tag{C.16}$$

Similarly, other FIM elements can be obtained as:

$$E\left[\frac{\partial \mathfrak{L}}{\partial \theta_i} \frac{\partial \mathfrak{L}}{\partial \theta_l}\right] = \frac{2}{\sigma^2} \Re e \left[\zeta_i^H \zeta_l \Psi_{\mathbf{a}'_\theta \mathbf{a}'_\theta}^{i,l} \sum_{k=1}^{N} R_{ss}^{i,l}(k) \gamma(k)\right] \tag{C.17}$$

$$E\left[\frac{\partial \mathfrak{L}}{\partial \phi_i} \frac{\partial \mathfrak{L}}{\partial \phi_l}\right] = \frac{2}{\sigma^2} \Re e \left[\zeta_i^H \zeta_l \Psi_{\mathbf{a}'_\phi \mathbf{a}'_\phi}^{i,l} \sum_{k=1}^{N} R_{ss}^{i,l}(k) \gamma(k)\right] \tag{C.18}$$

$$E\left[\frac{\partial \mathfrak{L}}{\partial \nu_i} \frac{\partial \mathfrak{L}}{\partial \nu_l}\right] = \frac{8\pi^2}{\sigma^2} \Re e \left[\Psi_{\mathbf{aa}}^{i,l} \zeta_i^H \zeta_l \sum_{k=1}^{N} R_{ss}^{i,l}(k) \gamma(k) t_k^2\right] \tag{C.19}$$

$$E\left[\frac{\partial \mathfrak{L}}{\partial \eta_i} \frac{\partial \mathfrak{L}}{\partial \eta_l}\right] = \frac{2}{\sigma^2} \Re e \left[\Psi_{\mathbf{aa}}^{i,l} \sum_{k=1}^{N} R_{ss}^{i,l}(k) \gamma(k)\right] \tag{C.20}$$

$$E\left[\frac{\partial \mathfrak{L}}{\partial \kappa_i} \frac{\partial \mathfrak{L}}{\partial \kappa_l}\right] = \frac{2}{\sigma^2} \Re e \left[\Psi_{\mathbf{aa}}^{i,l} \sum_{k=1}^{N} R_{ss}^{i,l}(k) \gamma(k)\right] \tag{C.21}$$

$$E\left[\frac{\partial \mathfrak{L}}{\partial \tau_i} \frac{\partial \mathfrak{L}}{\partial \theta_l}\right] = \frac{2}{\sigma^2} \Re e \left[\Psi_{\mathbf{aa}'_\theta}^{i,l} \zeta_i^H \zeta_l \sum_{k=1}^{N} R_{s's}^{i,l}(k) \gamma(k)\right] \tag{C.22}$$

$$E\left[\frac{\partial \mathfrak{L}}{\partial \tau_i} \frac{\partial \mathfrak{L}}{\partial \phi_l}\right] = \frac{2}{\sigma^2} \Re e \left[\Psi_{\mathbf{aa}'_\phi}^{i,l} \zeta_i^H \zeta_l \sum_{k=1}^{N} R_{s's}^{i,l}(k) \gamma(k)\right] \tag{C.23}$$

$$E\left[\frac{\partial \mathfrak{L}}{\partial \tau_i} \frac{\partial \mathfrak{L}}{\partial \nu_l}\right] = \frac{4\pi}{\sigma^2} \Im m \left[\Psi_{\mathbf{aa}}^{i,l} \zeta_i \zeta_l^H \sum_{k=1}^{N} R_{s's}^{i,l}(k) \gamma^H(k) t_k\right] \tag{C.24}$$

$$E\left[\frac{\partial \mathfrak{L}}{\partial \tau_i}\frac{\partial \mathfrak{L}}{\partial \eta_l}\right] = \frac{2}{\sigma^2}\Re e\left[\Psi^{i,l}_{\mathbf{aa}}\zeta_i^H\sum_{k=1}^{N}R^{i,l}_{s's}(k)\gamma(k)\right] \tag{C.25}$$

$$E\left[\frac{\partial \mathfrak{L}}{\partial \tau_i}\frac{\partial \mathfrak{L}}{\partial \kappa_l}\right] = \frac{-2}{\sigma^2}\Im m\left[\Psi^{i,l}_{\mathbf{aa}}\zeta_i\sum_{k=1}^{N}R^{i,l}_{s's}(k)\gamma^H(k)\right] \tag{C.26}$$

$$E\left[\frac{\partial \mathfrak{L}}{\partial \theta_i}\frac{\partial \mathfrak{L}}{\partial \phi_l}\right] = \frac{2}{\sigma^2}\Re e\left[\zeta_i^H\zeta_l\Psi^{i,l}_{\mathbf{a}'_\theta\mathbf{a}'_\phi}\sum_{k=1}^{N}R^{i,l}_{ss}(k)\gamma(k)\right] \tag{C.27}$$

$$E\left[\frac{\partial \mathfrak{L}}{\partial \theta_i}\frac{\partial \mathfrak{L}}{\partial \nu_l}\right] = \frac{4\pi}{\sigma^2}\Im m\left[\Psi^{i,l}_{\mathbf{aa}'_\theta}\zeta_i\zeta_l^H\sum_{k=1}^{N}R^{i,l}_{ss}(k)\gamma^H(k)t_k\right] \tag{C.28}$$

$$E\left[\frac{\partial \mathfrak{L}}{\partial \theta_i}\frac{\partial \mathfrak{L}}{\partial \eta_l}\right] = \frac{2}{\sigma^2}\Re e\left[\Psi^{i,l}_{\mathbf{a}'_\theta\mathbf{a}}\zeta_i^H\sum_{k=1}^{N}R^{i,l}_{ss}(k)\gamma(k)\right] \tag{C.29}$$

$$E\left[\frac{\partial \mathfrak{L}}{\partial \theta_i}\frac{\partial \mathfrak{L}}{\partial \kappa_l}\right] = \frac{-2}{\sigma^2}\Im m\left[\Psi^{i,l}_{\mathbf{a}'_\theta\mathbf{a}}\zeta_i\sum_{k=1}^{N}R^{i,l}_{ss}(k)\gamma^H(k)\right] \tag{C.30}$$

$$E\left[\frac{\partial \mathfrak{L}}{\partial \nu_i}\frac{\partial \mathfrak{L}}{\partial \eta_l}\right] = \frac{4\pi}{\sigma^2}\Im m\left[\Psi^{i,l}_{\mathbf{aa}}\zeta_i^H\sum_{k=1}^{N}R^{i,l}_{ss}(k)\gamma(k)t_k\right] \tag{C.31}$$

$$E\left[\frac{\partial \mathfrak{L}}{\partial \nu_i}\frac{\partial \mathfrak{L}}{\partial \kappa_l}\right] = \frac{-4\pi}{\sigma^2}\Re e\left[\Psi^{i,l}_{\mathbf{aa}}\zeta_i^H\sum_{k=1}^{N}R^{i,l}_{ss}(k)\gamma(k)t_k\right] \tag{C.32}$$

$$E\left[\frac{\partial \mathfrak{L}}{\partial \eta_i}\frac{\partial \mathfrak{L}}{\partial \kappa_l}\right] = \frac{-2}{\sigma^2}\Im m\left[\Psi^{i,l}_{\mathbf{aa}}\sum_{k=1}^{N}R^{i,l}_{ss}(k)\gamma^H(k)\right]\ . \tag{C.33}$$

Bibliography

[1] T. S. Rappaport, *Wireless Communications Principles and Practice.* Prentice Hall, 2002.

[2] T. S. Rappaport, S. Y. Seidel, and R. Singh, "900 mhz multipath propagation measurements for u.s. digital cellular radiotelephone," *IEEE Trans. Veh. Technol.*, pp. 132–139, May 1990.

[3] D. A. Hawbaker, "Indoor wideband radio wave propagation measurements and models at 1.3 ghz and 4.0 ghz," Ph.D. dissertation, Virginia Tech., Virginia Tech., Blacksburg, VA, 1991.

[4] H. Krim and M. Viberg, "Two decades of array signal processing research: the parametric approach," *IEEE Signal Process. Mag.*, vol. 13, no. 4, pp. 67–94, Jul. 1996.

[5] J. Capon, "High-resolution frequency-wavenumber spectrum analysis," *Proc. IEEE*, vol. 57, no. 8, pp. 1408–1418, Aug. 1969.

[6] R. O. Schmidt, "A signal subspace approach to multiple emitter location and spectral estimation," Ph.D. dissertation, Stanford Univ., Stanford, CA, 1981.

[7] M. Rubsamen and A. B. Gershman, "Direction-of-arrival estimation for nonuniform sensor arrays: from manifold separation to fourier domain MUSIC methods," *IEEE Trans. Signal Process.*, vol. 57, no. 2, pp. 588–599, Feb. 2009.

[8] P. Chevalier, A. Ferreol, L. Albera, and G. Birot, "Higher order direction finding from arrays with diversely polarized antennas: The PD-2Q-MUSIC algorithms," *IEEE Trans. Signal Process.*, vol. 55, no. 11, pp. 5337–5350, Nov. 2007.

[9] M. Viberg and B. Ottersten, "Sensor array processing based on subspace fitting," *IEEE Trans. Signal Process.*, vol. 39, no. 5, pp. 1110–1121, May. 1991.

[10] M. Viberg, B. Ottersten, and T. Kailath, "Detection and estimation in sensor arrays using weighted subspace fitting," *IEEE Trans. Signal Process.*, vol. 39, no. 11, pp. 2436–2449, Nov. 1991.

[11] R. Roy and T. Kailath, "Esprit-estimation of signal parameters via rotational invariance techniques," *IEEE Trans. Acoust., Speech, Signal Process.*, vol. 37, no. 7, pp. 984–995, Jul. 1989.

[12] M. Haardt and J. A. Nossek, "Unitary esprit: how to obtain increased estimation accuracy with areduced computational burden," *IEEE Trans. Signal Process.*, vol. 43, no. 5, pp. 1232–1242, May. 1995.

[13] L. C. Godara, "Application of antenna arrays to mobile communications, part ii: Beam-forming and direction-of-arrival considerations," *Proc. IEEE*, vol. 85, no. 8, pp. 1195–1245, Aug. 1997.

[14] A. P. Dempster, N. M. Laird, and D. B. Rubin, "Maximum likelihood from incomplete data via the EM algorithm," *J. Roy. Statist. Soc.*, vol. 39, no. 1, pp. 1–38, 1977.

[15] J. A. Fessler and A. O. Hero, "Space-alternating generalized expectation-maximization algorithm," *IEEE Trans. Signal Process.*, vol. 42, no. 10, pp. 2664–2677, Oct. 1994.

[16] P. J. Chung and J. F. Bohme, "Recursive EM and SAGE-inspired algorithms with application to DOA estimation," *IEEE Trans. Signal Process.*, vol. 53, no. 8, pp. 2664–2677, Aug. 2005.

[17] N. Czink, X. Yin, H. Ozcelik, M. Herdin, E. Bonek, and B. H. Fleury, "Cluster characteristics in a MIMO indoor propagation environment," *IEEE Trans. Wireless Commun.*, vol. 6, no. 4, pp. 1465–1475, April 2007.

[18] A. Kocian, I. Land, and B. H. Fleury, "Joint channel estimation, partial successive interference cancellation, and data decoding for DS-CDMA based on the SAGE algorithm," *IEEE Trans. Commun.*, vol. 55, no. 6, pp. 1231–1241, Jun. 2007.

[19] B. H. Fleury, M. Tschudin, R. Heddergott, D. Dahlhaus, and K. I. Pedersen, "Channel parameter estimation in mobile radio environments using the SAGE algorithm," *IEEE J. Sel. Areas Commun.*, vol. 17, no. 3, pp. 434–450, Mar. 1999.

[20] X. Fu, H. Minn, and C. D. Cantrell, "Two novel iterative joint frequency-offset and channel estimation methods for OFDMA uplink," *IEEE Trans. Commun.*, vol. 56, no. 3, pp. 474–484, Mar. 2008.

[21] K. Haneda and J. I. Takada, "An application of SAGE algorithm for UWB propagation channel estimation," in *IEEE Int. Conf. Ultra Wideband Systems and Technologies (UWBST)*, 2003.

[22] M. Guenach, M. Marey, H. Wymeersch, H. Steendam, and M. Moeneclaey, "Turbo estimation and equalization for asynchronous uplink MC-CDMA," *IEEE Trans. Wireless Commun.*, vol. 7, no. 4, pp. 1217–1226, April 2008.

[23] N. Levanon and E. Mozeson, *Radar Signals.* Wiley-IEEE Press, 2004.

[24] M. B. Guldogan and O. Arikan, "A novel array signal processing technique for multipath channel parameter estimation," in *IEEE Signal Process. and Commun. Applications (SIU)*, 2007.

[25] M. B. Guldogan, O. Arikan, and F. Arikan, "A new technique for direction of arrival estimation for ionospheric multipath channels," *J. Adv. Space Res.*, vol. 44, no. 6, pp. 653–662, Sept. 2009.

[26] M. B. Guldogan and O. Arikan, "Cross-ambiguity function domain direction finding technique for multipath channel parameter estimation," *Signal Processing*, submitted to Signal Processing.

[27] ——, "Comparison of the CAF-DF and SAGE algorithms in multipath channel parameter estimation," in *IEEE Wksp. Sensor Array and Multichannel Signal Processing (SAM)*, 2008.

[28] M. B. Guldogan, O. Arikan, and F. Arikan, "A new technique for direction-of-arrival estimation for ionospheric multipath channels," in *IRI/COST 296 WORKSHOP on Ionosphere-Modelling, Forcing and Telecommunications*, 2007.

[29] M. B. Guldogan and O. Arikan, "Performance analysis of cross ambiguity function - direction finding technique in multipath environments," in *IEEE Signal Process. and Commun. Applications (SIU)*, 2008.

[30] D. E. Goldberg, *Genetic Algorithms in Search, Optimization and Machine Learning.* Addison-Wesley Longman Publishing, 1989.

[31] M. Dorigo and T. Stutzle, *Ant Colony Optimization.* MIT Press, 2004.

[32] K. V. Price, R. Storn, and J. A. Lampinen, *Differential Evolution: a practical approach to global optimization.* Springer, 2005.

[33] A. Loengarov and V. Tereshko, "A minimal model of honey bee foraging," in *IEEE Int. Symp. Swarm Intelligence (SIS)*, 2006.

[34] Y. Liu and K. Passino, “Biomimicry of social foraging bacteria for distributed optimization: Models, principles, and emergent behaviors,” *J. Optim. Theory Appl.*, vol. 115, no. 3, pp. 603–628, Dec. 2002.

[35] J. Kennedy and R. Eberhart, “Particle swarm optimization,” in *IEEE Int. Conf. Neural Networks*, 1995.

[36] F. Arikan, O. Koroglu, S. Fidan, O. Arikan, and M. B. Guldogan, “Multipath separation-direction of arrival (MS-DOA) with genetic search algorithm for hf channels,” *J. Adv. Space Res.*, vol. 44, no. 6, pp. 641–652, Sept. 2009.

[37] S. N. Sivanandan and S. N. Deepa, *Introduction to Genetic Algorithms.* Springer, 2008.

[38] G. K. Venayagamoorthy and W. Zha, “Comparison of nonuniform optimal quantizer designs for speech coding with adaptive critics and particle swarm,” *IEEE Trans. Ind. Appl.*, vol. 43, no. 1, pp. 238–244, Jan. 2007.

[39] Y. Yuan, Z. He, and M. Chen, “Virtual MIMO-based cross-layer design for wireless sensor networks,” *IEEE Trans. Veh. Technol.*, vol. 55, no. 3, pp. 856–864, May. 2006.

[40] S. Selvan, C. Xavier, N. Karssemeijer, J. Sequeira, R. Cherian, and B. Dhala, “Parameter estimation in stochastic mammogram model by heuristic optimization techniques,” *IEEE Trans. Inf. Technol. Biomed.*, vol. 10, no. 4, pp. 685–695, Oct. 2006.

[41] K. Veeramachaneni, L. Osadciw, and P. Varshney, “An adaptive multimodal biometric management algorithm,” *IEEE Trans. Syst., Man, Cybern. C*, vol. 35, no. 3, pp. 344–356, Aug. 2005.

[42] Z. L. Gaing, “A particle swarm optimization approach for optimum design of pid controller in avr system,” *IEEE Trans. Energy Convers.*, vol. 19, no. 2, pp. 384–391, June 2004.

[43] J. Heo, K. Lee, and R. Garduno-Ramirez, "Multiobjective control of power plants using particle swarm optimization techniques," *IEEE Trans. Energy Convers.*, vol. 21, no. 2, pp. 552–561, June 2006.

[44] A. Chatterjee, K. Pulasinghe, K. Watanabe, and K. Izumi, "A particle-swarm-optimized fuzzy-neural network for voice controlled robot systems," *IEEE Trans. Ind. Electron.*, vol. 52, no. 6, pp. 1478–1489, Dec 2005.

[45] Y. Ma, C. Jiang, Z. Hou, and C. Wang, "The formulation of the optimal strategies for the electricity producers based on the particle swarm optimization algorithm," *IEEE Trans. Power Syst.*, vol. 21, no. 4, pp. 1663–1671, Nov. 2006.

[46] F. Grimaccia, M. Mussetta, and R. E. Zich, "Genetical swarm optimization: self-adaptive hybrid evolutionary algorithm for electromagnetics," *IEEE Trans. Antennas Propag.*, vol. 55, no. 3, pp. 781–785, March 2007.

[47] M. Wachowiak, R. Smolikova, Y. Zheng, J. Zurada, and A. Elmaghraby, "An approach to multimodal biomedical image registration utilizing particle swarm optimization," *IEEE Trans. Evol. Comput.*, vol. 8, no. 3, pp. 289–301, June 2004.

[48] M. B. Guldogan and O. Arikan, "A new multipath channel parameter estimation technique using swarm intelligence," in *IEEE Signal Process. and Commun. Applications (SIU)*, 2009.

[49] ——, "Particle swarm optimization based channel identification in cross-ambiguity domain," in *IEEE Int. Conf. Acoust. Speech Sign. Processing (ICASSP)*, 2010.

[50] ——, "Multipath channel identification by using global optimization in ambiguity function domain," *IEEE Trans. Signal Process.*, submitted.

[51] J. K. Javers, "An analysis of pilot symbol assisted modulation for rayleigh fading channels," *IEEE Trans. Veh. Technol.*, vol. 40, no. 4, pp. 686–693, Nov. 1991.

[52] M. K. Simon and M. S. Alouini, *Digital Communication Over Fading Channels.* John Wiley, 2005.

[53] S. Cotter and B. Rao, "Sparse channel estimation via matching pursuit with applications to equalization," *IEEE Trans. Commun.*, vol. 50, no. 3, pp. 374–377, Mar. 2002.

[54] A. Sayeed and B. Aazhang, "Joint multipath-doppler diversity in mobile wireless communications," *IEEE Trans. Commun.*, pp. 123–132, Jan. 1999.

[55] W. Bajwa, J. Haupt, A. Sayeed, and R. Nowak, "Compressed channel sensing: A new approach to estimating sparse multipath channels," *IEEE Trans. Signal Process.*, to appear in the Proc. of IEEE (special issue on Sparse Signal Processing).

[56] G. E. Pfander, H. Rauhut, and J. Tanner, "Identification of matrices having a sparse representation," *IEEE Trans. Signal Process.*, vol. 56, no. 11, pp. 257–275, Nov. 2008.

[57] M. Herman and T. Strohmer, "High-resolution radar via compressed sensing," *IEEE Trans. Signal Process.*, vol. 57, no. 6, pp. 2275–2285, Jun. 2009.

[58] A. C. Gurbuz, J. H. McClellan, and V. Cevher, "A compressive beamforming method," in *IEEE Int. Conf. Acoust. Speech Sign. Processing (ICASSP)*, 2008.

[59] V. Cevher, A. C. Gurbuz, and J. H. McClellan, "Compressive wireless arrays for bearing estimation,," in *IEEE Int. Conf. Acoust. Speech Sign. Processing (ICASSP)*, 2008.

[60] C. Y. Chen and P. P. Vaidyanathan, "Compressed sensing in mimo radar," *CALTECH ACM Tech. Report*, 2009.

[61] Y. Yu, A. Petropulu, and H. V. Poor, "Compressive sensing for mimo radar," in *IEEE Int. Conf. Acoust. Speech Sign. Processing (ICASSP)*, 2009.

[62] D. Malioutov, M. Cetin, and A. S. Willsky, "A sparse signal reconstruction perspective for source localization with sensor arrays," *IEEE Trans. Signal Process.*, vol. 53, no. 8, pp. 3010–3023, Aug. 2005.

[63] Y. Yu, A. P. Petropulu, and H. V. Poor, "Mimo radar using compressive sampling," *IEEE Trans. Signal Process.*, submitted. Available online: arXiv:0911.4752.

[64] M. B. Guldogan, M. Pilanci, and O. Arikan, "Compressed sensing on ambiguity function domain for high resolution detection," in *IEEE Signal Process. and Commun. Applications (SIU)*, 2010.

[65] M. B. Guldogan and O. Arikan, "Multipath channel identification by novel compressed sensing techniques," *IEEE Trans. Signal Process.*, will be submitted.

[66] Y. C. Pati, R. Rezaiifar, and P. S. Krishnaprasad, "Orthogonal matching pursuit: Recursive function approximation with applications to wavelet decomposition," in *Proc. 27th Asilomar Conf. Signals, Systems, and Computers*, 1993.

[67] X. Wang and H. V. Poor, *Wireless Communication Systems - Advanced Techniques for Signal Reception.* Prentice Hall, 2002.

[68] R. Prasad, *Towards a Global 3G Systems: Advanced Mobile Communications in Europe.* Artec House, 2001.

[69] B. Bing, R. V. Nee, and V. Hayes, "Wireless local area and home networks," *IEEE Commun. Mag.*, vol. 39, no. 11, pp. 63–157, Nov. 2001.

[70] W. Webb, *Introduction to Wireless Local Loop: Broadband and Narrowband Systems*. Artec House, 2000.

[71] A. F. Molisch, *Wireless Communications*. IEEE Press, 2005.

[72] F. Adachi, M. Feeney, A. Williamson, and J. Parsons, "Crosscorrelation between the envelope of 900 mhz signals received at a mobile radio base station," *Proc. IEE*, vol. 133, no. 6, pp. 506–512, Oct. 1986.

[73] W. R. Braun and U. Dersch, "A physical mobile radio channel model," *IEEE Trans. Veh. Technol.*, vol. 40, no. 2, pp. 472–482, May 1991.

[74] A. Paulraj and C. B. Papadias, "Space-time processing for wireless communication," *IEEE Signal Process. Mag.*, vol. 14, pp. 49–83, Nov. 1997.

[75] J. Chuang, "The effects of time delay spread on portable communications channels with digital modulation," *IEEE J. Sel. Areas Commun.*, vol. 5, no. 5, pp. 879–889, Jun. 1987.

[76] B. D. Woerner, J. H. Reed, and T. S. Rappaport, "Simulations issues for future wireless modems," *IEEE Signal Process. Mag.*, pp. 19–35, July 1994.

[77] R. Janaswamy, *Radiowave propagation and smart antennas for wireless communications*. Kluwer Academic Publishers, 2001.

[78] S. U. Pillai, *Array Signal Processing*. Springer-Verlag, 1989.

[79] A. Goldsmith, *Wireless Communications*. Cambridge University Press, 2005.

[80] P. Bello, "Characterization of randomly time-variant linear channels," *IEEE Trans. Commun.*, pp. 360–393, Dec. 1963.

[81] A. Saleh and R. Valenzuela, “A statistical model for indoor multipath propagation,” *IEEE J. Sel. Areas Commun.*, pp. 128–137, Feb. 1987.

[82] A. Molisch, “Ultrawideband propagation channels - theory, measurement and modeling,” *IEEE Trans. Veh. Technol.*, pp. 1528–1545, Sep. 2005.

[83] W. F. Schreiber, “Advanced television systems for terrestrial broadcasting: Some problems and some proposed solutions,” *Proc. IEEE*, vol. 83, pp. 958–981, Jun. 1995.

[84] I. J. Fevrier, S. B. Gelfand, and M. P. Fitz, “Reduced complexity decision feedback equalization for multipath channels with large delay spreads,” *IEEE Trans. Commun.*, vol. 47, pp. 927–937, Jun. 1999.

[85] M. Kocic, “Sparse equalization for real-time digital underwater acoustic communications,” in *Proc. OCEAN*, 1995.

[86] W. Li and J. Preisig, “Estimation of rapidly time-varying sparse channels,” *IEEE J. Ocean. Eng.*, pp. 927–939, Oct. 2007.

[87] S. Ariyavisitakul, N. R. Sollenberger, and L. J. Greenstein, “Tap selectable decision-feedback equalization,” *IEEE Trans. Commun.*, vol. 45, pp. 1497–1500, Dec. 1997.

[88] W. Bajwa, A. Sayeed, and R. Nowak, “Sparse multipath channels: Modeling and estimation,” in *IEEE Wksp. Digital Signal Processing*, 2008.

[89] ——, “Learning sparse doubly-selective channels,” *Universiy of Wisconsin-Madison Technical Report ECE*, Jun. 2008.

[90] A. M. Sayeed and V. Veeravalli, “The essential degrees of freedom in space-time fading channels,” in *IEEE Int. Conf. Personal, Indoor and Mobile Radio Communications (PIMRC)*, 2002.

[91] M. Feder and E. Weinstein, "Parameter estimation of superimposed signals using the EM algorithm," *IEEE Trans. Acoust., Speech, Signal Process.*, vol. 36, pp. 477–489, Apr. 1988.

[92] F. Arikan, N. Yilmaz, O. Arikan, and M. K. B. H. Miled, "Mode separation-direction of arrival angle estimation," *Radio Science*, vol. 38, no. 1, pp. 7.1–7.14, 2003.

[93] D. Siddle, A. Stocker, and E. Warrington, "Time of flight and direction of arrival of hf radio signals received over a path along the midlatitude trough: Observations," *Radio Science*, vol. 39, Aug. 2004.

[94] E. Warrington, C. Jackson, and B. Lundborg, "Directional diversity of hf signals received over high latitude paths, and the possibility of improved data throughput by means of spatial filtering," *IEE Proc. Microw. Antennas Propag.*, vol. 147, pp. 487–494, Aug. 2000.

[95] M. K. Ozdemir and H. Arslan, "Channel estimation for wireless OFDM systems," *IEEE Commun. Surveys Tuts.*, vol. 9, no. 2, pp. 18–48, Second Quarter 2007.

[96] P. M. Woodward, *Probability and Information Theory with Application to Radar.* London: Pergamon, 1953.

[97] A. Jakobsson, A. Swindlehurst, and P. Stoica, "Subspace-based estimation of time delays and doppler shifts," *IEEE Trans. Signal Process.*, vol. 46, no. 9, pp. 2472–2483, Sept. 1998.

[98] M. I. Skolnik, *Introduction to Radar Systems.* McGraw-Hill, 2001.

[99] M. Li and Y. Lu, "Maximum likelihood DOA estimation in unknown colored noise fields," *IEEE Trans. Aerosp. Electron. Syst.*, vol. 44, no. 3, pp. 1079–1090, Jul. 2008.

[100] D. Bratton and J. Kennedy, "Defining a standard for particle swarm optimization," in *IEEE Int. Symp. Swarm Intelligence (SIS)*, 2007.

[101] C. E. Shannon, "Communication in the presence of noise," *Proc. IEEE*, vol. 86, no. 2, pp. 447–457, 1998.

[102] M. Unser, "Sampling-50 years after shannon," *Proc. IEEE*, vol. 88, no. 4, pp. 569–587, Apr. 2000.

[103] D. M. Donoho, "Compressed sensing," *IEEE Trans. Inf. Theory*, vol. 52, no. 4, pp. 1289–1306, 2006.

[104] Y. Tsaig and D. Donoho, "Extensions of compressed sensing," *Signal Processing*, vol. 86, no. 3, pp. 549–571, Mar. 2006.

[105] E. J. Candes, J. Romberg, and T. Tao, "Robust uncertainty principles: Exact signal reconstruction from highly incomplete frequency information," *IEEE Trans. Inf. Theory*, vol. 52, no. 2, pp. 489–509, Feb. 2006.

[106] E. J. Candes and T. Tao, "Near-optimal signal recovery from random projections: Universal encoding strategies," *IEEE Trans. Inf. Theory*, vol. 52, no. 12, pp. 5406–5425, Dec. 2006.

[107] R. Rubinstein, A. M. Bruckstein, and M. Elad, "Dictionaries for sparse representation modeling," *IEEE Trans. Signal Process.*, To appear, 2010.

[108] S. S. Chen, D. L. Donoho, and M. A. Saunders, "Atomic decomposition by basis pursuit," *SIAM Rev.*, vol. 43, no. 1, pp. 129–159, 2001.

[109] J. A. Tropp, J. N. Laska, M. F. Duarte, J. K. Romberg, and R. G. Baraniuk, "Beyond nyquist: Efficient sampling of sparse bandlimited signals," *IEEE Trans. Inf. Theory*, submitted. Available online: arXiv:0902.0026v2.

[110] M. Mishali and Y. C. Eldar, "Blind multiband signal reconstruction: Compressed sensing for analog signals," *IEEE Trans. Signal Process.*, vol. 57, no. 3, pp. 993–1009, Mar. 2009.

[111] S. Gleichman and Y. C. Eldar, "Blind compressed sensing," *IEEE Trans. Inf. Theory*, submitted. Available online: arXiv:1002.258.

[112] M. Lustig, D. L. Donoho, J. M. Santos, and J. M. Pauly, "Compressed sensing mri," *IEEE Signal Process. Mag.*, vol. 25, no. 2, pp. 72–82, Mar. 2008.

[113] D. Donoho and X. Huo, "Uncertainty principles and ideal atomic decomposition," *IEEE Trans. Inf. Theory*, vol. 47, no. 7, pp. 2845–2862, 2001.

[114] J. A. Tropp, "Just relax: Convex programming methods for identifying sparse signals in noise," *IEEE Trans. Inf. Theory*, vol. 52, no. 3, pp. 1030–1051, 2006.

[115] D. L. Donoho, M. Elad, and V. N. Temlyakov, "Stable recovery of sparse overcomplete representations in the presence of noise," *IEEE Trans. Inf. Theory*, vol. 52, no. 1, pp. 6–18, 2006.

[116] E. J. Candes and T. Tao, "The dantzig selector: Statistical estimation when p is much larger than n," *Ann. Statist.*, vol. 35, no. 6, pp. 2313–2351, 2007.

[117] L. R. Welch, "Lower bounds on the maximum cross-correlation of signals," *IEEE Trans. Inf. Theory*, vol. 20, no. 3, pp. 397–399, 1974.

[118] E. J. Candes, "The restricted isometry property and its implications for compressed sensing," *Comptes Rendus Mathematique*, vol. 346, no. 9, pp. 589–592, May. 2008.

[119] Z. B. Haim, Y. C. Eldar, and M. Elad, "Coherence-based performance guarantees for estimating a sparse vector under random noise," *IEEE Trans. Signal Process.*, submitted. Available online: arXiv:0903.4579v2.

[120] J. A. Tropp and S. J. Wright, "Computational methods for sparse solutions of linear inverse problems," *CALTECH ACM Tech. Report*, vol. 1, pp. 1–8, Mar. 2009.

[121] S. Mallat and Z. Zhang, "Matching pursuits with time-frequency dictionaries," *IEEE Trans. Signal Process.*, vol. 41, no. 12, pp. 3397–3415, 1993.

[122] R. Chartrand, "Exact reconstruction of sparse signals via nonconvex minimization," *IEEE Signal Process. Lett.*, vol. 14, no. 10, pp. 707–710, Oct. 2007.

[123] A. J. Miller, *Subset selection in regression.* London: Chapman and Hall, 2002.

[124] D. Wipf and B. Rao, "Sparse bayesian learning for basis selection," *IEEE Trans. Signal Process.*, vol. 52, no. 8, pp. 2153–2164, Aug. 2004.

[125] R. Tibshirani, "Regression shrinkage and selection via the lasso," *J. Roy. Statist. Soc.*, vol. 58, pp. 267–288, 1996.

[126] D. Needell and J. A. Tropp, "Cosamp: Iterative signal recovery from incomplete and inaccurate samples," *Applied and Computational Harmonic Analysis*, vol. 26, no. 3, pp. 301–321, May 2009.

[127] D. Needell and R. Vershynin, "Uniform uncertainty principle and signal recovery via regularized orthogonal matching pursuit," *Foundations of Computational Mathematics*, vol. 9, no. 3, pp. 317–334, June 2009.

[128] D. L. Donoho, Y. Tsaig, I. Drori, and J. L. Starck, "Sparse solution of underdetermined linear equations by stagewise orthogonal matching pursuit (stomp)," submitted, 2007.

[129] Z. B. Haim and Y. C. Eldar, "The cramer rao bound for estimating a sparse vector," *IEEE Trans. Signal Process.*, Will appear. Available online.

[130] S. Kay, *Fundamentals of Statistical Signal Processing: Estimation Theory.* Prentice Hall, 1993.

[131] J. A. Tropp, "Greed is good: Algorithmic results for sparse approximation," *IEEE Trans. Inf. Theory*, vol. 50, no. 10, pp. 2231–2242, Oct. 2004.

[132] W. O. Alltop, "Complex sequences with low periodic correlations," *IEEE Trans. Inf. Theory*, vol. 26, no. 3, pp. 350–354, May 1980.

[133] T. Strohmer and R. H. Jr., "Grassmannian frames with applications to coding and communications," *Applied and Computational Harmonic Analysis*, vol. 14, no. 3, pp. 257–275, 2003.

[134] H. C. R. M. Planat and S. Perrine, "A survey of finite algebraic geometrical structures underlying mutually unbiased quantum measurements," *Found. Phys.*, vol. 36, no. 11, pp. 1662–1680, Nov. 2006.

[135] P. Stoica and A. Nehorai, "MUSIC, maximum likelihood, and Cramer-Rao bound," *IEEE Trans. Acoust., Speech, Signal Process.*, vol. 37, no. 5, pp. 720–741, May. 1989.